The University Of Sheffield.

Fabrication and characterisation of microcavity based III-nitride optoelectronics on a microscale

Guillem Martínez de Arriba

A thesis submitted in partial fulfilment of the requirements for the degree of Doctor of Philosophy

The University of Sheffield

Department of Electronic and Electrical Engineering

December 2022

Abstract

In this work, the design implementation, fabrication and characterisation on III-nitride microemitters with microcavity effects grown on c-plane sapphire are presented. Highly doped GaN layers have been effectively porosified by means of electrochemical etching (EC). Different porous morphology is established by varying the doping level of the GaN layer and the EC bias voltage, enabling a wide refractive index tunability of the porous layer. Through this thesis the potential of nearly-lattice matched nanoporous GaN as a cladding layer and as a Distributed Bragg reflector (DBR) has been fundamentally studied. There are three major parts that constitute the outcome of the work. The first part is on the development and characterisation of a novel microcavity based microemitter array, which partially mitigates one of the consequences of the Quantum Confined Stark Effect (QCSE). The so-called 'blue shifting' of the emission wavelength that is considered to be one of the long-standing problems of III-nitrides has been reduced from 50 nm to 3 nm. The second part highlights a novel approach towards micro-Vertical Surface Emitting Lasers, which is achieved by developing a direct epitaxial method based on selective epitaxial growth. Nearly lattice-matched porous DBRs have been achieved with reflectivities over 99%. Strong cavity effects have been demonstrated via electrical and optical pumping. Although stimulated emission is not fully confirmed, the full width at half maximum of the peak emission has been reduced by a factor of 5. Finally, the last part is an introduction on the potential enhancement effect of porous GaN as a cladding layer in III-nitride green edge emitting lasers, instead of conventional AlGaN. There is an enhancement in the optical confinement by a factor of 2.5, as verified using a Finite Difference Eigenmode solver. Porous cladding layers have been effectively formed, achieving porosities of 50%. Effective current injection through the porous was demonstrated. However, the inherent challenges from the cleaving of sapphire substrates limited the facet formation. Thus, stimulated emission was not confirmed yet.

Acknowledgements

I would like to express my gratitude to the people who helped me during my journey of pursuing a PhD. First, I would like to thank Prof. Tao Wang, who gave me the opportunity to purse a PhD degree in the area of III-nitrides. His advice and opinions not only guided me through my research but also shaped my mentality.

I am also very grateful to Dr. Jie Bai, Dr. Yuefei Cai, Dr. Nicolas Poyiatzis, Dr. Ye Tian and Dr. Suneal Gathora. Specially I would like to say thanks to Dr. Xiangyu He who helped me to improve my device fabrication skills and boosted my theoretical knowledge. Finally, I would like to thank to Dr. Elizabeth Prieto for all the useful suggestions about my research and discussions about VCSELs.

This project would not be possible without the people who grew the samples and spend uncountable amount of time taking care of the MOVPE reactors, they are the real motor of this group. Therefore, I want to show my most sincere gratitude to: Xinchi Chen, Rongzi Ni, Ce Xu and Dr. Peng Feng. Furthermore, I would like to thank to Dr. Chenqi Zhu, who introduced me into the growth field during the last few months of my PhD and was always very patient in helping and explaining MOCVD growth.

Finally, I would like to express my sincere appreciation to my parents, my brother and the rest of my family, for their love, support and encouragement all the time. Special thanks to my girlfriend for her support and company during these tough years (ài ài ài).

Publications

G. Martinez de Arriba, P. Feng, C. Xu, C. Zhu, J. Bai and T. Wang, "Simple Approach to Mitigate the Emission Wavelength Instability of III-Nitride μLED Arrays". *ACS Photonics* **9**, 2073–2078 (2022).

P. Fletcher[*], **G. Martínez de Arriba[*],** Y. Tian, N. Poyiatzis, C. Zhu, P. Feng, J. Bai and T. Wang, Optical characterisation of InGaN-based microdisk arrays with nanoporous GaN/GaN DBRs. *J. Phys. D: Appl. Phys.* **55**, 464001 (2022).
[*] Co-first author

C. Zhu, C. Xu, P. Feng, **G. Martinez de Arriba,** J. Bai and T. Wang, A comparison study of InGaN/GaN multiple quantum wells grown on (111) silicon and (0001) sapphire substrates under identical conditions. *J. Phys. D: Appl. Phys.* **55**, 444003 (2022).

P. Feng, C. Xu, J.Bai, C. Zhu, I. Farrer, **G. Martinez de Arriba,** and T. Wang, A Simple Approach to Achieving Ultrasmall III-Nitride Microlight-Emitting Diodes with Red Emission. *ACS Appl. Electron. Mater.* **4**, 2787–2792 (2022).

Y. Tian, P. Feng, C. Zhu, X. Chen, C. Xu, V. Esendag, **G. Martinez de Arriba** and T. Wang, Nearly Lattice-Matched GaN Distributed Bragg Reflectors with Enhanced Performance. *Materials* **15**, 3536 (2022).

G. Martinez de Arriba, P. Feng, C. Xu, C. Zhu, J. Bai and T. Wang, Micro-LEDs with a mode control emission wavelength. Semiconductor & Integrated Optoelectronics conference (SIOE), 12th-14th April 2022, Cardiff.

Contents

List of Figures

List of Tables

Chapter 1: Introduction

In this chapter the background of my PhD project via the thesis and the motivation and potential applications for III-nitride based optoelectronics devices are introduced. This thesis focuses on the design, fabrication and characterisation of microcavity based devices, aiming to obtain a new kind of optoelectronics on a microscale.

1.1 Motivation

Light emitting diodes (LEDs) cover a wide range of applications, from the visible range to infrared for telecommunications. A laser diode (LD) performs better than a LED in terms of beam directionality, modulation speed, and output power density. However, the structure and the fabrication of a laser diode is more complex than those of a LED, as an optical cavity for achieving photon feedback is necessary for a LD.

LEDs have a long lifetime (~100000 hours) and a low electrical consumption, which is about 30 times less than incandescent bulbs. It was therefore expected that LEDs could potentially help to reduce the global energy consumption, where lighting accounts for 20% of overall electricity [1]. In fact, recent studies show that LED bulb market is expected to reach a value of 14.8 billion USD by 2027 [2]. Moreover, LEDs can be used not only for solid state lighting but also LED TV, backlighting, traffic lighting and automotive applications [3,4].

III-nitrides LEDs are risen as the ideal candidate to replace conventional lighting sources due to the direct bandgap material of GaN. However, the performance of III-nitride LEDs is still required to be further improved by developing new approaches to further increase their efficiency. Internal quantum efficiency (IQE) and extraction efficiency are two major parameters in determining device performance. IQE relies on the quality of the active region (where photons are produced) grown by Metal Organic Chemical Vapour Deposition (MOCVD). External quantum efficiency (EQE) is limited due to the high index contrast between GaN and air which generates a small solid angle (24°) [5-8]. In this case, most of the generated light is reflected into the device unless extra processes are utilised.

The placement of a quantum well (QW) into a microcavity can enhance its optical extraction [9-15]. Furthermore, other benefits such as narrowing in emission wavelength and reduction in emission divergence can be achieved. These are particularly attractive for AR/VR applications, where emitters on a microscale are the key elements for manufacturing microdisplays [16,17].

1.2 History of the development of III-nitride light emitting diodes

In 1907 the first electroluminescent device was discovered by H.J. Round, who found it while testing a SiC layer with a metal electrode [18]. The luminescence phenomenon was reported in 1928, where O.V. Lossev proved the generation of light due to an electric current or electric field, instead of the black-body light emissions from conventional incandescence [19]. Holonyak and Bevacqua reported the first commercial red LED based on GaAsP in 1962[20]. Furthermore, by tuning the composition of a GaAsP alloy, the emission wavelength can shift from red to green [21]. Afterwards, BELL Labs introduced green LEDs by using N-doped GaP [22].

At that moment, the emission wavelength could only be achieved between the red and green spectral range. In 1960s the research community focused their effort aiming to extend the wavelength to blue and UV by using wideband gap SiC and III-nitride materials. SiC based blue LEDs were available in 1990 with an emission wavelength at 470 nm but a low optical efficiency of 0.03% [23]. Therefore, SiC could not be attractive for many applications mainly due to the low efficiency as a result of its indirect-bandgap structure.

Crystalline GaN films grown on sapphire by using Hybrid Vapour Phase Epitaxy (HVPE) were reported by Maruska et al in 1969 [24].

In 1972, Pankove et al. reported the first blue GaN diode based in a metal-insulator-semiconductor (MIS) [25]. However, low crystal quality and a great challenge in achieving p-dope GaN made the material unattractive to researchers [26]. In 1986, Amano and Akasaki invented a novel growth approach, leading to a major improvement in the crystal quality. Their approach was to initially introduce a thin AlN buffer layer at a low temperature, typically 450°C, before the deposition of a thick GaN at a high temperature of above 1000°C [27]. The so-called two step approach has become a standard method to grow GaN on sapphire substrates using Metal Organic Chemical Vapour Deposition (MOCVD). In 1989, Amano and Akasaki reported a solution to obtain p-type GaN which is based on the activation of Mg-dopant through low-energy electron beam irradiation (LEEBI) [28]. The first p-n GaN based junction was reported in 1992 [22]. Finally, in 1993 Nakamura who was then a Nichia employee demonstrated the activation of Mg dopants simply by a thermal annealing method, in a nitrogen ambient [29]. One year later, Nakamura presented the first blue, green and yellow LED based on InGaN/AlGaN quantum wells [30]. Major achievements in III-nitride semiconductors have been made during the last two decades. In 2014 Professors Isamu Akasaki, Hiroshi Amano and Shuji Nakamura received the

Nobel Prize for their contribution to III-nitride epitaxial growth. Figure 1 illustrates the bandgaps of III-nitrides across the whole compositional range covering the whole visible spectrum, part of the ultraviolet and part of infrared, offering major advantages for a wide range of applications, such as solid-state lighting, high resolution displays, visible light communication (VLC), solar energy etc [31-35].

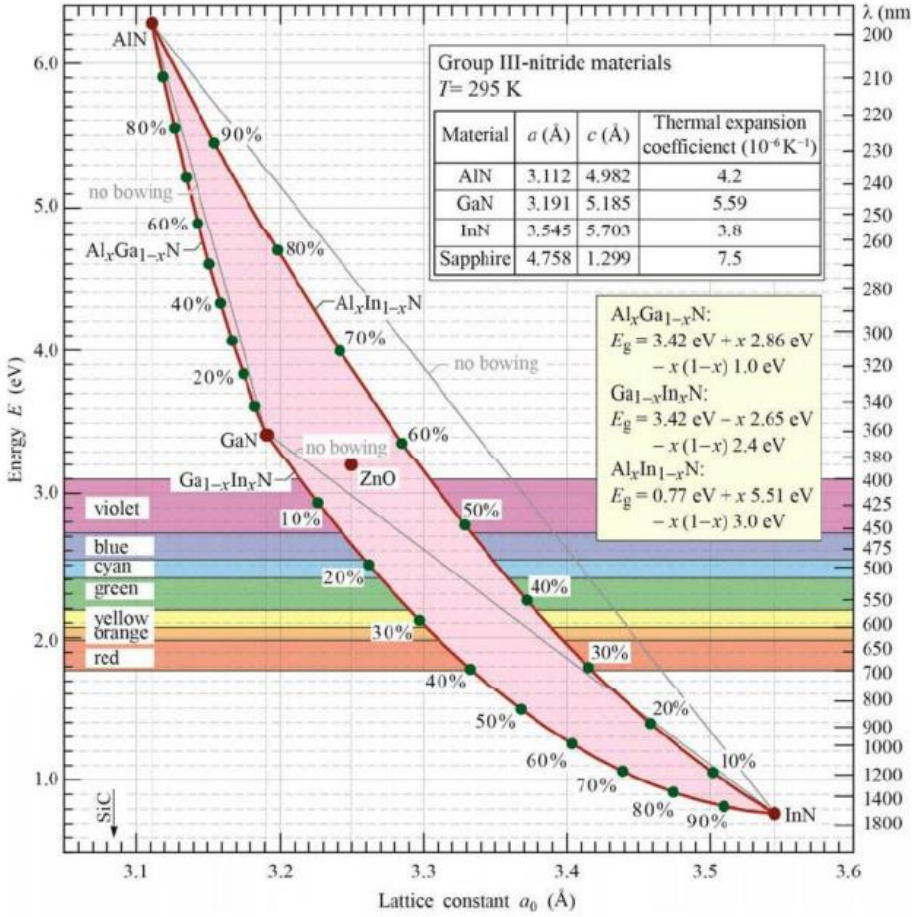

Figure 1: Bandgap energy versus lattice constant of III-nitride materials at RT. (Reproduced with permission from E. F. Schubert [23]).

1.3 Challenges

The last two decades have seen major advancements in developing III-nitride semiconductor devices. However, so far, the major success has been achieved in GaN grown on c-plane (001) substrates. This polar orientation possesses several challenges that limit the performance of III-nitride optoelectronic devices.

1.3.1 Issues with substrates

Free-standing GaN can be typically obtained by Hybrid Vapour Phase Epitaxy (HVPE) followed by a lift-off process. The typical procedure involves an initial growth of up to 300 µm GaN on sapphire and then a substrate-removal process typically by using a laser lift off (LLO) technique [36-39]. It has been observed

that LLO often produce bowing effects, leading to cracking and even the damage of the active emitting area of an LED wafer [40]. The lack of affordable GaN substrates also restricts the material growth to lattice mismatched heteroepitaxy, where sapphire (Al2O3), silicon carbide (6H-SiC) and silicon (Si,111) can be used as substrates. However, a huge lattice-mismatch is typically generated when GaN is grown on their top. Furthermore, there also exists a large difference of thermal expansion coefficient.

This huge difference often leads to strain induced defects, while these defects act as non-radiative recombination centres which reduce the quantum efficiency of III-nitride optoelectronics. Sapphire offers a lattice mismatch of 16%, while the lattice-mismatch between SiC and GaN is just 3% [41]. It is worth noting that SiC substrates are highly expensive. Si substrates are the cheapest among the three major substrates, but the lattice mismatch between Si and GaN is 17%, which leads to severe cracking issues [42].

All the samples used in this thesis have been grown on Sapphire substrates.

1.3.2 Quantum confined Stark effect (QCSE)

GaN exhibits a hexagonal wurtzite crystal structure. The c-axis suffers a strong polarisation due to the non-centrosymmetric nature of the wurtzite structure [43]. An internal electric field is generated at interface surfaces due to polarisation charges. The optical and the electrical properties of c-plane GaN are significantly influenced by this internal field [23]. There exist two different types of polarisations in III-nitrides and their heterostructures: spontaneous polarisation and piezoelectric polarisation: spontaneous polarisation due to the asymmetry of the atomic bonding of the wurtzite structure, and piezoelectric polarisation which is caused by tensile or compressive stress applied to the material. Tensile strain is produced when a material with smaller lattice constant is grown above of a substrate with a larger lattice constant. Figure 2 illustrates the pseudomorphic compressive strain produced due to the growth of lattice mismatched epitaxial layer with a thickness below the critical thickness.

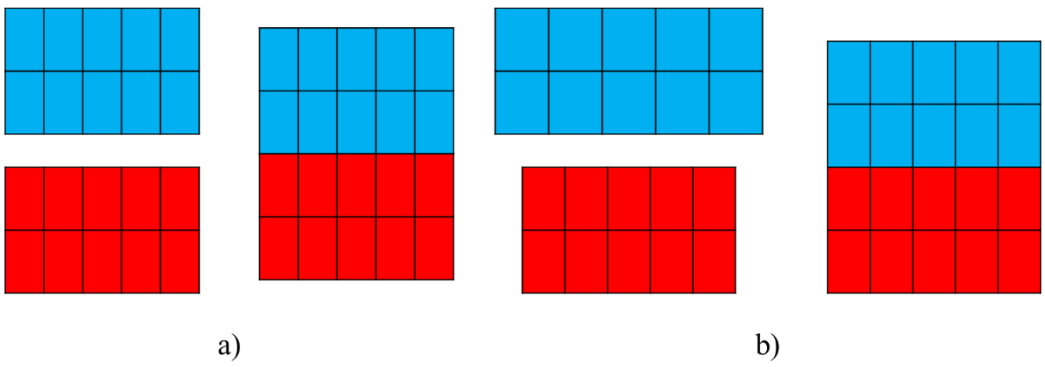

Figure 2: a) Lattice matched epitaxy b) Lattice mismatched epitaxy leading to compressive strain.

The active region of III-nitride emitter in the visible spectral region is normally based on InGaN MQWs, where the emission wavelength can cover the whole visible spectrum (390nm-720nm) by tuning its indium composition across [44]. The lattice mismatch between InGaN and GaN lead to a strong polarisation effect which bends the energy bands. Furthermore, the generated electric field pulls apart the electron and hole wavefunction, as electrons are attracted to the anode and holes to the cathode, as shown in Figure 3. Consequently, the efficiency of radiative recombination is reduced and a red-shift of the emission wavelength is produced [45]. This phenomenon is known as Quantum Confined Stark Effect (QCSE). The QCSE becomes increasingly strong with increasing the emission wavelength of an emitter, which requires higher indium content [46]. This generates stronger piezoelectric fields, thus enhancing the QCSE and then reducing the efficiency. The band structure can be flattened by increasing the carrier density in the active region due to screening effects resulting in a blue shift in emission wavelength.

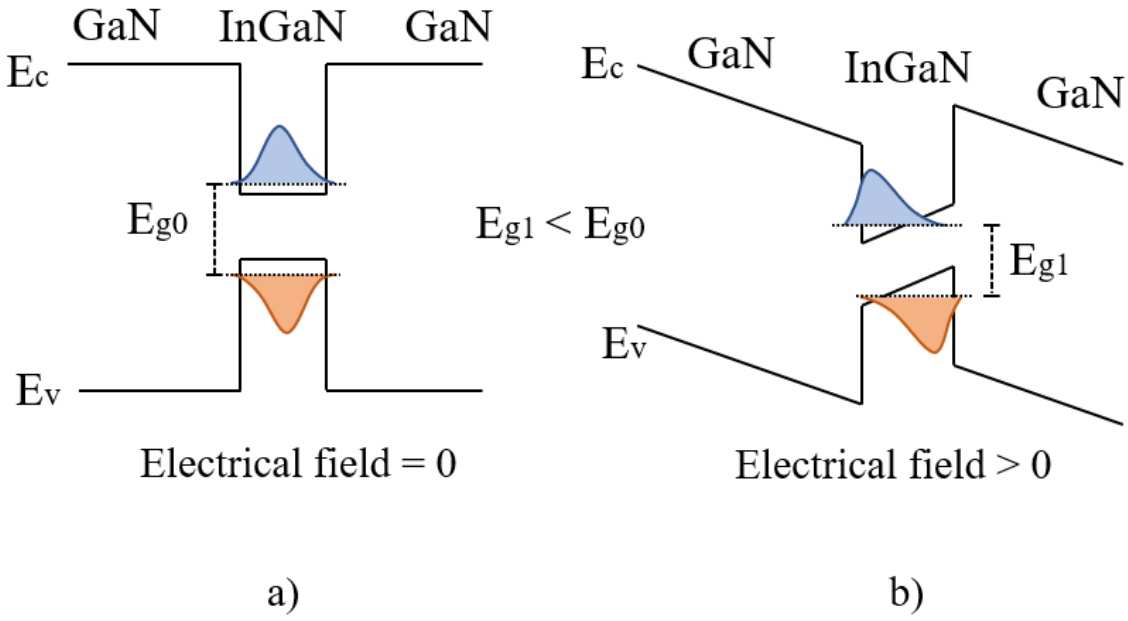

Figure 3: a) MQWs without any external electric field. b) MQWs band-bending due to external electric field.

1.3.3 Issue on green gap

One of the great challenges of III-nitride optoelectronics is to obtain long wavelength efficient emitters, specifically in the green-yellow region, where the required indium content in InGaN MQWs for emitting longer wavelengths leads to a reduction in overall efficiency, as a result of enhanced QCSE. Conventionally, nitrogen was added to GaP to achieve yellow emission [47]. However, GaP band

structure is indirect, which causes low-efficiency. Figure 4 illustrates the external quantum efficiency as a function of wavelength in the whole visible spectral region demonstrating the so called green-gap.

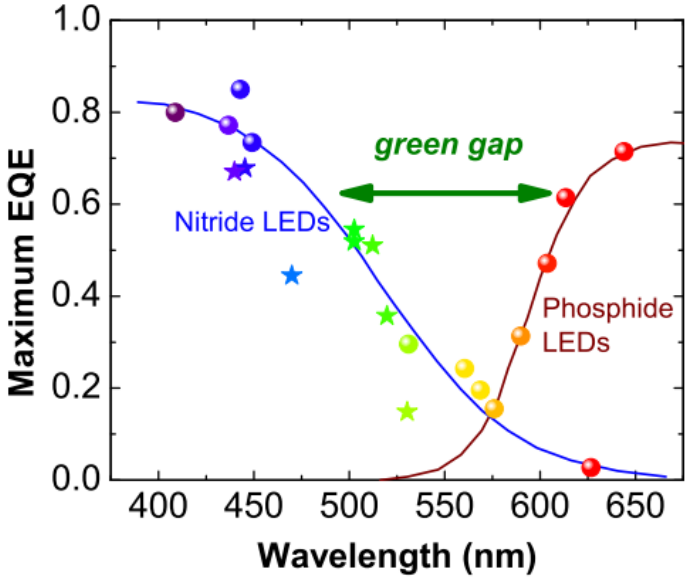

Figure 4: External Quantum Efficency (EQE) of different comercial nitride and phosphide LEDs [47].

1.3.4 Efficiency droop

External Quantum Efficiency (EQE) describes the ratio of the number of emitted photons to the number of injected electrons. Ideally, LEDs emitted power is directly determined by injected current. However, in a real scenario, the efficiency decreases gradually with increasing injection current. This phenomenon is known as 'efficiency droop'[49-51]. The droop phenomenon is currently the subject of research worldwide, its origin still unclear, although several models have been proposed, such as non-radiative recombination processes due to Auger recombination, defects, leakage current or Shockley-Read-Hall recombination (SRH) [49]. Figure 5 illustrates the EQE droop for InGaN based LEDs, showing an initial increase of EQE at low current and then a decrease of EQE with further injection current.

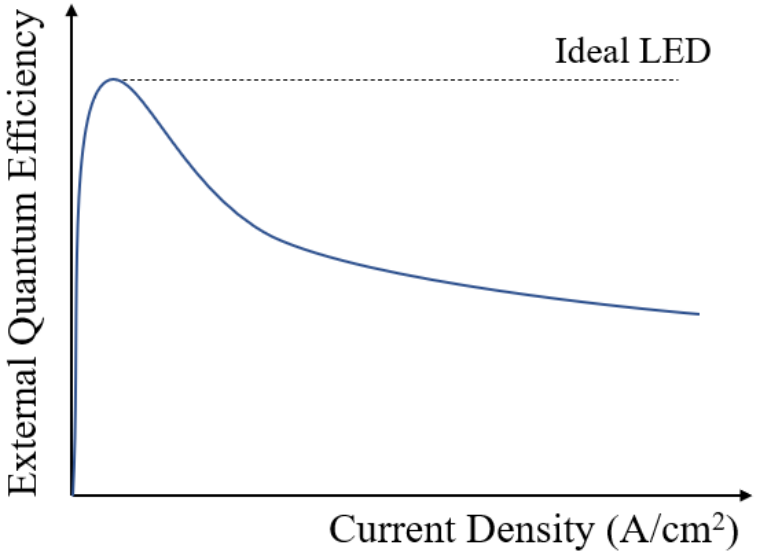

Figure 5: Efficency droop of InGaN LED under high current density.

Auger recombination is a non-radiative process that involves three carriers. It takes place after electron-hole recombination. Instead of producing a photon, the electron or the hole are further excited to a higher energy state. The excited carrier losses its energy by emitting phonons (lattice vibrations) which eventually converts into thermal energy [51]. Another non-radiative effect is due to SRH, where unwanted impurities or defects can act as trap energy levels. Current leakage is a carrier transport process where carriers escape from the active region without forming a photon.

1.5 Thesis Outline

This thesis aims to design a monolithically integrated structure which combines a microcavity and an LED or a laser on a micrometre scale, aiming to demonstrate superior device performance which does not exist. Such a novel device can lead to partially mitigating QCSE and a reduction in naturally broadened emission linewidth. The thesis is split into seven chapters:

Chapter 1 presents the motivation of the thesis. Furthermore, the current challenges related to III-nitride based devices are described.

Chapter 2 describes the fundamental physics of semiconductors for LEDs and Lasers. A VCSEL architecture is presented, where the potential of nanoporous GaN to replace conventional DBRs is demonstrated.

Chapter 3 introduces the experimental methods used in this thesis. A detailed description of the fabrication and characterisation techniques is given.

Chapter 4 demonstrates the existence of whispering gallery modes in a microdisk structure by FDTD simulations. The limitations of current pedestal-based devices

are discussed. Finally, an alternative electrically injected approach based on porous cladding layers is presented.

Chapter 5 presents a novel approach to mitigating the QCSE by demonstrating a high density of green microemitter arrays. The peak emission shifting is reduced from 50nm to 3nm when compared to a standard device.

Chapter 6 opens the path to the first generation of micro-lasers based on our selective overgrowth microemitters. Although, lasing has not been achieved, interesting microcavity effects have been observed under optical and electrical pumping.

Chapter 7 highlights the benefits of utilising nanoporous GaN which can significantly enhance the confinement factor of III-nitride edge emitting lasers.

Chapter 8 presents a summary, conclusion and future work for microcavity micro-scale based devices.

The framework of this thesis combines device simulation, fabrication and characterisation. Block diagram 1 represents the standard logical procedure carried out through each chapter.

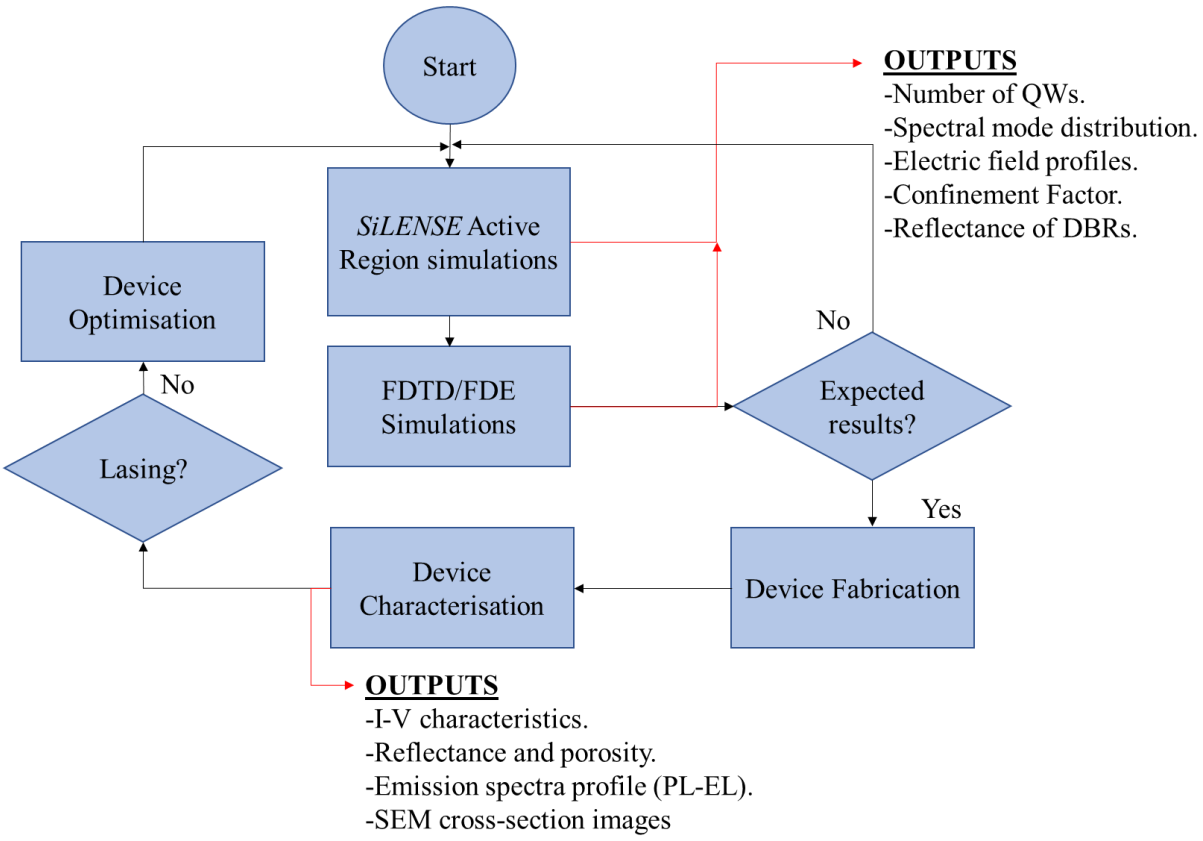

Block diagram 1: Logical cycle undertaken during this thesis.

1.6 References

[1] A. De Almeida, et al., Solid state lighting review - Potential and challenges in Europe. *Renewable and Sustainable Energy Reviews*, 34:30-48, 2014.

[2] LED Bulb Market: Global Industry Trends, Share, Size, Growth, Opportunity and Forecast 2022-2027

https://www.researchandmarkets.com/reports/5656607/led-bulb-market-global-industry-trends-share (Accesed: 1/03/2023)

[3] T. Taki and M. Strassburg, Review—Visible LEDs: More than Efficient Light. *ECS Journal of Solid State Science and Technology*, 9: 015017, 2020.

[4] J. Bhardwaj, R. Peddada and B. Spinger, Advanced LED technology for automotive applications, *Light-Emitting Diodes: Materials, Devices, and Applications for Solid State Lighting XX*, 9768: 976811, 2016.

[5] W. B. Joyce, et al. Geometrical properties of random particles and the extraction of photons from electroluminescent diodes. *Journal of Applied Physics*, 45: 2229–2253, 1974.

[6] J. J. Wierer, et al. InGaN/GaN quantum-well heterostructure light-emitting diodes employing photonic crystal structures. *Applied Physics Letters*, 84:3885–3887, 2004.

[7] M. Krames, et al. Status and future of high-power Light-Emitting Diodes for solid-state lighting. *Journal Display Technology*, 3:160–175, 2007.

[8] T.Fuji et al., Increase in the extraction efficiency of GaN-based light-emitting diodes via surface roughening. *Applied Physics Letters*, 84: 855 ,2004.

[9] J. Back, et al., High efficiency blue InGaN microcavity light-emitting diode with a 205 nm ultra-short cavity. *Applied Physics Letters*, 118:031102, 2021.

[10] H. De Neve, et al., Planar substrate-emitting-microcavity light-emitting diodes with 20% external QE. *Applied Physics Letters*, 70:799, 1997.

[11] C. Dill, et al., Effect of detuning on the angular emission pattern of high-efficiency microcavity light-emitting diodes. *Applied Physics Letters*, 73:3812, 1998.

[12] Y. C. Shen, et al., Optical cavity effects in InGaN/GaN quantum-well-heterostructure flip-chip light-emitting diodes. *Applied Physics Letters*, 82:2221, 2003.

[13] P. M. Pattison, et al., Gallium nitride based microcavity light emitting diodes with 2λ effective cavity thickness. *Applied Physics Letters*, 90:031111, 2007.

[14] D.Ochoa, et al., Microcavity light emitting diodes as efficient planar light emitters for telecommunication applications, *Comptes Rendus Physique*, 3:1:3-14, 2002.

[15] Y-S. Choi, et al., Microcavity InGaN light emitting diodes with a single Fabry-Pérot mode, *Phisica Status Solidi (c)*, 5:6:2306-2308, 2007.

[16] L. Baruah, MicroLED Microdisplays: An Invention Fueled by Augmented Reality. *Front line technology: Information displays*, 38:4:13-18, 2022.

[17] V. W. Lee, N. Twu, I. Kymissis, Micro-LED technologies and applications. *Information Display*, 32 :6:16– 23, 2016.

[18] H. J. Round. A Note on Carborundum. Elektron. *World*, 149:308–309, 1907.

[19] O. V. Lossev. CII. Luminous carborundum detector and detection effect and oscillations with crystals. *The London, Edinburgh, and Dublin Philosophical Magazine and Journal of Science*, 6(39):1024–1044, 1928.

[20] R. N. Hall, G. E. Fenner, J. D. Kingsley, T. J. Soltys, and R. O. Carlson. Coherent light emission from GaAs junctions. *Physical Review Letters*, 9(9):366, 1962.

[21] N. Holonyak and S. F. Bevacqua. Coherent (visible) light emission from Ga(As1−xPx) junctions. *Applied Physics Letters*, 1(4):82–83, 1962.

[22] R. A. Logan, H. G. White, and W. Wiegmann. Efficient green electroluminescence in nitrogen-doped GaP p-n junctions. *Applied Physics Letters*, 13(4):139–141, 1968.

[23] E. F. Schubert. *Light-Emitting Diodes*. Cambridge University Press, 2006.

[24] R. B. Jain and H. P. Maruska. How it really happened: The history of p-type doping of gallium nitride. *Physica Status Solidi (a)*, 204(6):1970–1976, 2007.

[25] J. I. Pankove, E. A. Miller, and J. E. Berkeyheiser. GaN blue light-emitting diodes. *Journal of Luminescence*, 5(1):84–86, 1972.

[26] S. Nakamura and M. R. Krames. History of gallium–nitride-based light-emitting diodes for illumination. *Proceedings of the IEEE*, 101(10):2211–2220, 2013.

[27] H. Amano, N. Sawaki, I. Akasaki, and Y. Toyoda. Metalorganic vapor phase epitaxial growth of a high quality GaN film using an AlN buffer layer. *Applied Physics Letters*, 48(5):353–355, 1986.

[28] H. Amano, M. Kito, K. Hiramatsu, and I. Akasaki. P-type conduction in Mg-doped GaN treated with low-energy electron beam irradiation (LEEBI). *Japanese Journal of Applied Physics*, 28(12A):L2112, 1989.

[29] S. Nakamura, N. Iwasa, and M. Senoh. Method of manufacturing p-type compound semiconductor, April 26 1994. US Patent 5,306,662.

[30] S. Nakamura, M. Senoh, N. Iwasa and S. I. Nagahama. High-brightness InGaN blue, green and yellow light-Emitting diodes with quantum well structures. *Japanese Journal of Applied Physics* . 34: L797, 1995.

[31] C. Zhou, et al., Review—The Current and Emerging Applications of the III-Nitrides. *ECS Journal of Solid State Science and Technology*, 6:12:Q149, 2017.

[32] R. P. Green, et al., Modulation bandwidth studies of recombination processes in blue and green InGaN quantum well micro-light-emitting diodes. *Applied Physics Letters*, 102:9:091103, 2013.

[33] J-H. Park, et al., A III-nitride nanowire solar cell fabricated using a hybrid coaxial and uniaxial InGaN/GaN multi quantum well nanostructure. *RSC advances*, 8(37): 20585–20592, 2018.

[34] J. Day, et al., III-Nitride full-scale high-resolution microdisplays. *Applied Physics Letters*, 9:031116, 2011.

[35] H. X. Jiang and J.Y. Lin, III-Nitride Quantum Devices—Microphotonics, Critical reviews in Solid State and Materials Sciences, 28(2):131-183, 2003.

[36] S. S. Park et al., Free-standing GaN substrates by Hybrid Vapor Phase Epitaxy. *Japanese Journal of Applied Physics*, 39: L1141, 2000.

[37] M. K. Kelly et al., Optical process for liftoff of group III-nitride films. *Physica Status Solidi (a)*, vol. 159, p. R3 ,1997.

[38] K.Motoki et al., Preparation of large free standing GaN substrates by Hybride capour phase epitaxy using GaAs as a starting substrate. *Japanese Journal of Applied Physics* , 40: L140, 2001.

[39] Y. Oshima et al., Preparation of free-standing GaN wafers by hybrid vapor phase epitaxy with void-assisted separation. *Japanese Journal of Applied Physics*, 42:L1, 2003.

[40] M.H. Donhan et al., Influence of laser lift-off on optical and structural properties of InGaN/GaN vertical blue light emitting diodes. *AIP Advances 2*, 022122, 2012.

[41] W.A.Melton, J.I.Pankove., GaN growth on sapphire. *Journal of Crystal Growth*, Volume 178, Issues 1-2 p. 169-173, 1997.

[42] A. Dadgar et al., Epitaxy of GaN on silicon-impact of symmetry and surface reconstruction. *New Journal of Physics*, 9:389 , 2007.

[43] S. Nakamura and S. F. Chichibu, Introduction to Nitride Semiconductor Blue Lasers and Light Emitting Diodes, 1st ed. (New York and London: Taylor & Francis, 2000).

[44] T. Mukai. et al., Characteristics of InGaN-Based UV/ Blue/ Green/ Amber/ Red Light-Emitting Diodes. *Japanese Journal of Applied Physics* , 38:3976 ,1999.

[45] P.Waltereit, et al., Nitride Semiconductors Free of Electrostatic Fields for Efficient White Light-Emitting Diodes. *Nature*, 406: 865–868, 2000.

[46] T. Takeuchi, et al., Determination of Piezoelectric Fields in Strained GaInN Quantum Wells Using the Quantum-Confined Stark Effect. *Applied Physics Letters*, 73:1691–1693, 1998.

[47] W. O. Groves, A. H. Herzog & M. G. Craford, The effect of nitrogen doping on GaAs1-xPx electroluminescent diodes. *Applied Physics Letters*, 19, 184–186, 1971.

[48] M. der Maur, et al., Unraveling the " Green Gap" problem: The role of random alloy fluctuations in InGaN/GaN light emitting diodes. arXiv preprint, 2015.

[49] J. Piprek, Efficiency droop in nitride-based light-emitting diodes. *Physica status solidi (a)*, 207:2217–2225, 2010.

[50] D. Zhu and C. J. Humphreys, Solid-state lighting based on light emitting diode technology. *Optics in Our Time* ,87–118, Springer International Publishing, 2016.

[51] J. Cho, E. F. Schubert, J. K. Kim, Efficiency Droop in Light-emitting Diodes: Challenges and Countermeasures. *Laser Photonics Reviews*,7 (3): 408–421, 2013.

Chapter 2: Background

2.1 Semiconductor device fundamentals

Solid materials can be classified according to their electrical properties which are determined by the bandgap energy (Eg), also named 'forbidden region' that is between the valance band (Ec) and conduction band (Ev). Solid state materials are categorised in three groups: insulators, conductors and semiconductors.

Conductive materials have a complete overlap between the conduction band and the valence band, so carriers (electrons-holes) are free to move without needing extra excitation energy even at room temperature. In semiconductors electrons can be excited from the conduction band to the valence band under a condition where the applied energy is equal or higher than the bandgap [1].

Based on the bandgap, a semiconductor can be divided into two different structures types with a direct or an indirect band structure. Figure 6 schematically illustrates the band structures of a direct band gap semiconductor and an indirect bandgap semiconductor.

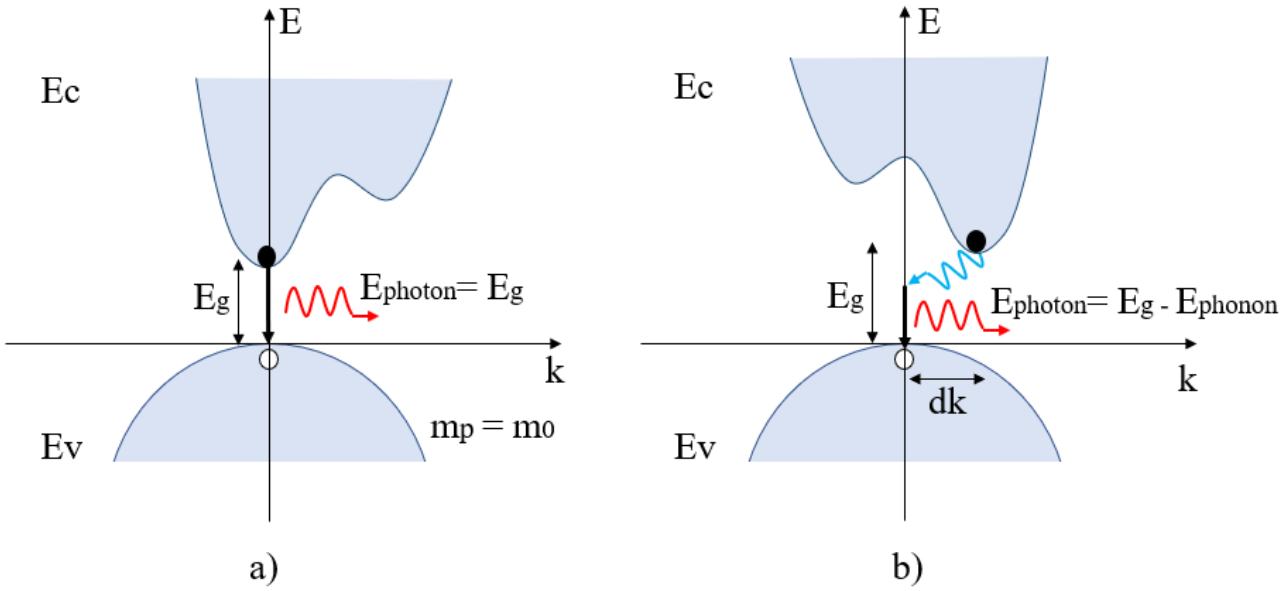

Figure 6: Representation of the band structure of a) direct and b) Indirect bandgap material

The recombination from an electron in the conduction band and a hole in the valence band leads to the emission of a photon. For a direct band-gap semiconductor, the valance band maximum and the conduction band minimum exhibit the same crystal momentum. However, for an indirect-bandgap semiconductors the valance band maximum and the conduction band minimum are located at different values of crystal momentum, thus requiring an extra particle to compensate the momentum difference to meet the momentum

conservation, typically via phonons (i.e. lattice vibration). This gives a much lower probability of electron-hole recombination than that for a direct-bandgap semiconductor. Therefore, a direct bandgap semiconductor is normally used for fabricating high-efficiency optoelectronic devices [2]. The relationship between bandgap and the emission wavelength of photons is expressed as:

$$Eg = Ec - Ev \approx \frac{hc}{\lambda} \quad (1)$$

Where Eg is the bandgap, Ec is the energy of the minimum energy level of the conduction band, Ev is the maximum energy level of the valence band, λ is the emitted wavelength from the semiconductor, h is the Planck constant and c is the speed of light in a vacuum [3].

2.1.1Crystal structure of III-nitrides

III-nitride semiconductors have three basic binary alloys, which are AlN, GaN and InN, respectively. III-nitride semiconductors exhibit three possible kinds of crystal structures depending on their atomic configuration: rock-salt, zinc-blende and wurtzite [4]. Rock-salt can only be formed under high pressure (52.2GPa for GaN). Under normal ambient conditions, hexagonal wurtzite is the most thermodynamically stable between all of them, and thus GaN wurtzite is widely used. Wurtzite structure has hexagonal symmetry formed by ABABAB HCP lattices along (0001) direction. Two parameters are commonly used to describe a wurtzite hexagonal structure: the in-plane lattice constant (a) and the out-plane lattice constant (b), where the former represents the spacing between adjacent atoms within the same basal plane and the latter one represents the distance between two adjacent basal planes. Figure 7, schematically illustrates a GaN wurtzite structure, where the each N_2 atom is naturally bonded to four Ga atoms (dashed lines). The two HCP sublattices of Ga and N have an offset that is equal to 5/8 of the height of the cell.

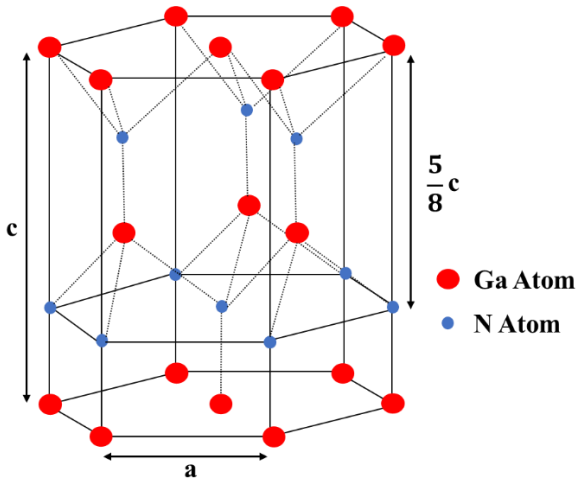

Figure 7:Schematic representation of a GaN wurtzite unit cell.

Table 1 shows the lattice constants of III-nitrides with a wurtzite structure including their in-plane and out-plane lattice constants.

Table 1 : Lattice Constant of GaN, AlN and InN [5].

Material	Lattice Constant a (Å)	Lattice Constant c (Å)
GaN	3.189	5.185
AlN	3.112	4.982
InN	3.533	5.693

Ternary alloys such as $In_xGa_{x-1}N$ maintain the wurtzite structure due to the isomorphous nature of III-nitride. The composition content of individual materials can tune the bandgap of the alloys.

The work done in this thesis is based on devices in a wurtzite structure.

Electrical Properties

The wide bandgap materials (WBG) offer high breakdown voltages and intrinsically high thermal conductivity which make them the ideal candidates for high frequency and high temperature applications, where heat dissipation is critical [6]. Table 2 shows the electrical and thermal properties of WBG at room temperature. The main drawback of GaN compared to other mature semiconductors is its low electron mobility, which is also affected by impurities and crystal defects. Therefore, it is crucial to optimise the growth conditions to achieve high crystal quality.

Table 2: Electrical and thermal properties of GaN and other semiconductors at 300K [7-16].

Material	Bandgap (eV)	Electron mobility (cm^2/Vs)	Breakdown Field (MV/cm)	Thermal Conductivity ($Wcm^{-1}K^{-1}$)
GaN	3.4	1245	3.3	2.3
Si	1.12	1400	0.3	0.55
SiC (4H-SiC)	3.26	380	3	3.6
GaAs	1.4	9400	0.4	0.55
InP	1.34	5400	0.5	0.68

Polarisation

As mentioned above, this thesis is based on wafers grown on c-plane sapphire substrates. Due to the non-centrosymmetric nature of a wurtzite structure, there is a strong polarisation along the c-axis [17]. The active region formed by InGaN/GaN MQWs suffers from lattice-mismatch induced strain, resulting in a piezoelectric polarisation. The strain can be either compressive or tensile. Depending on the strain type, piezoelectric polarisation can be opposed or contribute to the spontaneous polarisation. Compressive strain, such as InGaN/Gan heterostructure has P_{pz} in the opposite direction to P_{sp}, as InGaN suffers compressive strain on a GaN surface, while AlGaN grown on GaN suffers tensile strain, leading P_{pz} and P_{sp} to be aligned in the same direction. Figure 8, schematically illustrates the resultant piezoelectric polarisation effect.

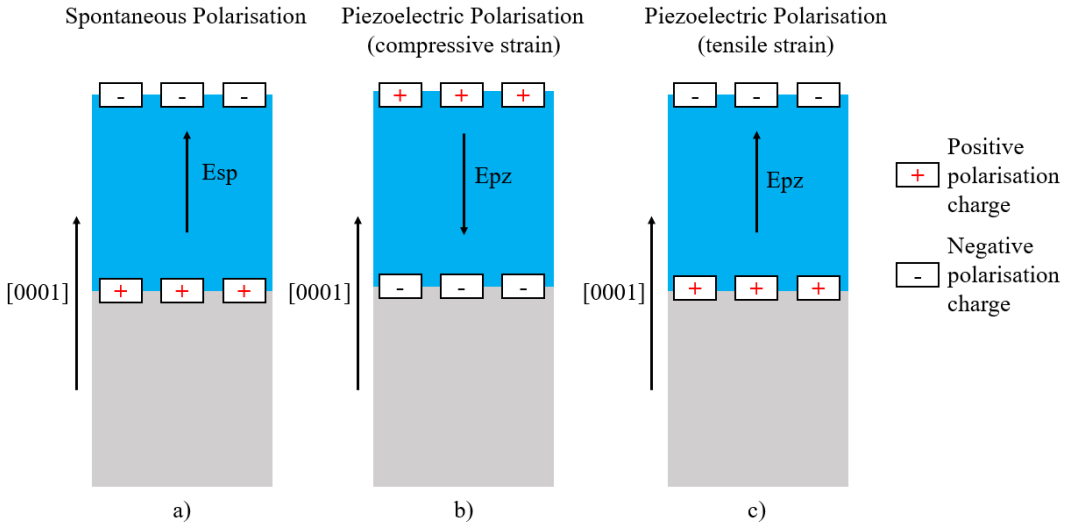

Figure 8: Schematic of surface charges and direction of the electric field. a) The spontaneous polarisation effect (e.g GaN on Sapphire). b) The piezoelectric polarisation effect under compressive strain (InN on GaN). c) The piezoelectric polarisation effect under tensile strain (e.g. AlN on GaN). Adapted with permission from [18].

The intrinsic electric field generated by the polarisation will detrimentally affect the optical performance of a quantum well structures grown on c-plane substrates, leading to an increase in radiative recombination lifetime and thus a reduction in quantum efficiency.

Generally speaking, a reduction in the thickness of InGaN MQW facilitates to minimise polarisation effects, leading to a decrease in the separation of electron and hole wavefunctions[19]. Polarisation effect can also be minimised or removed by growing a III-nitride LED structure on non-polar or semipolar planes [20-22]. Furthermore, piezoelectric polarisation can be reduced by introducing strain relaxation layers underneath of the InGaN active region [23].

2.1.2 Carrier concentration, doping and recombination

The conductivity of a semiconductor is determined by the density of free carriers (electrons and holes) and their mobilities, which can be described by:

$$\sigma = ne\mu n + ne\mu p \tag{2}$$

Where n is the charge density, e is the elemental charge of an electron and μn and μp are the mobility of the electron and hole respectively [24]. The mobility is a material dependant parameter which describes how electrons and holes can move through a semiconductor under an electric field.

For an intrinsic semiconductor, the carrier density is described by:

$$ni = \sqrt{NEcNEv}\, e^{\left(-\frac{Eg}{2KBT}\right)} \tag{3}$$

Where NEc and NEv are the density of states in the conduction and valance band respectively [24]. The conductivity of a material could be increased if impurities are added, generating an excess of free carriers. This technique is known as doping. Two types of dopants can be added: p-type (acceptor-holes) or n-type (donors-electrons). As an example, for an III-nitride semiconductor, Magnesium (Mg) is typically used for p-type doping, as Mg atoms replace Ga atoms generating additional vacancies, while Si atoms can replace Ga atoms generating free electrons and thus leading to n-type GaN. The impurities form an extra energy level in the bandgap forming shallow level states, which can be close to either the conduction band or the valence band. For n-type doping, the formed energy level lies close the conduction band, while p-type impurities form shallow level states that are close to the valance band.

Under equilibrium conditions at a given temperature (no external excitation), the product of electron and hole carrier concentrations is a constant value. Equation 4 describes the law of mass action:

$$nopo = ni^2 \quad (4)$$

There exist five major mechanisms which are responsible for electron-hole recombination in III-nitrides, shown in Figure 9. The recombination process that generates photons is known as radiative recombination, while the recombination process which leads to energy released in a form of thermal energy is called non-radiative recombination.

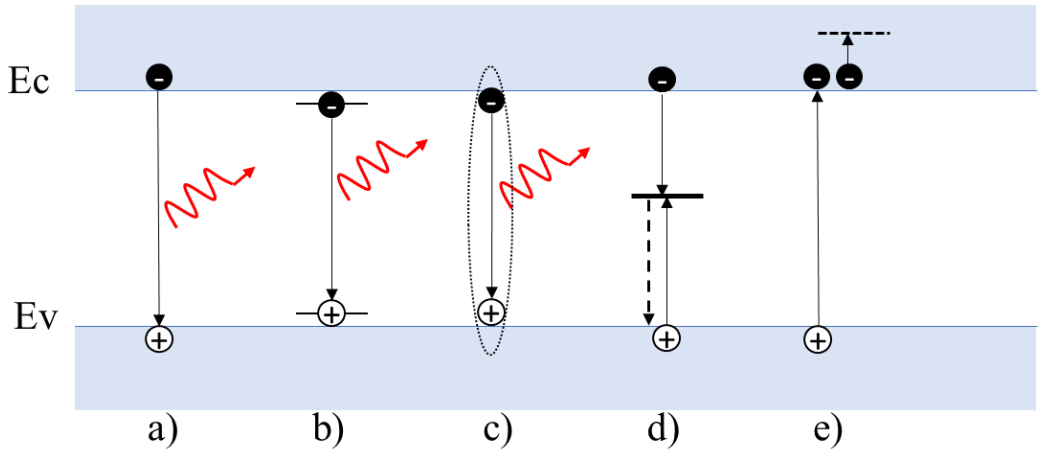

Figure 9: Recombination mechanism in semiconductors: a) Spontaneous band-edge recombination. b) Donor-acceptor recombination. c) Exciton pair recombination. d) Shockley-Reed-Hall recombination (SRH). e) Auger recombination.

Radiative Recombination

Band edge emission

Described as the radiative recombination process where an electron in the conduction band losses its energy and recombines with a hole in the valence band. The energy loss results in an emitted photon with the energy of the bandgap.

Donor-acceptor recombination

Doped semiconductor exhibits shallow states near the conduction or the valance band, depending on the kind of impurities that have been added. The recombination phenomenon will produce a photon with less energy than the band-gap energy.

Excitonic Recombination

Excitonic recombination is the processes that forms excitons, created by a coulombic attraction of carriers with opposite charge (electrons and holes). Excitons are characterised as neutrally charged quasiparticles, which can be divided into two categories. Wannier-Mott excitons weakly bonded in the crystal due to its large radius. Frenkel excitons commonly present in insulators tightly

bounded to the atoms due to a smaller radius, making them difficulty in movement within the crystal [25].

Bohr model can be used to calculate the exciton binding energy:

$$En = -\frac{\mu}{mo}\frac{1}{\varepsilon r^2}\frac{RH}{n^2} \quad (5)$$

Where RH is the Rydberg constant for a hydrogen atom (13.61eV). For GaN the excitonic energy is 25meV, which is similar to the thermal energy at room temperature, therefore excitons can be formed at room temperture [26]. Excitonic recombination produces a photon with slightly smaller energy than the bandgap of the material (Eg - En).

Non-radiative recombination

Shockley-Read-Hall (SRH)

Electron-hole recombination produced in trap levels created by a dopant or a defect, which leads to an exchanging of energy in the form of lattice vibration (phonon). SRH is predominantly a single-particle process, therefore is dominating under low excitation.

Auger recombination

Auger recombination involves three carriers, takes place under a high electrical or optical excitation density. The released energy produced by the electron-hole recombination will excite another atom into a higher energy state, instead of releasing a photon. The 'hot' carrier will then relax down to the band edge by releasing multiple phonon emission. Normally, Auger recombination takes place as the carrier density is increased, therefore is one of the causes of the efficiency droop [27].

The total recombination rate needs to consider both radiative and non-radiative process, given by;

$$Rtotal = R_{rad} + R_{SHR} + R_{Auger} \quad (6)$$

2.1.3 P-n junctions, heterojunctions and light emitting diodes

Epitaxial growth technology is used for combining p-type and n-type materials, giving the name of PN-junction. There are two types of PN-junctions, which are homojunctions and heterojunctions. The homojunction consist of a single crystalline material structure, which has the same bandgap across the whole junction. Heterojunctions consists of two kinds of semiconductors with different bandgaps. Figure 10a) schematically illustrates the geometry of a PN-junction

under unbiased applied bias. Electrons in the n-type and holes in the p-type diffuse towards the opposite direction due to the carrier density gradient. After that, positive and negative charges are left in the n-type and p-type regions, respectively, forming an electrostatic potential (eV_B) to stop carriers further diffusing. This region between the n-type and p-type layers exhibits a very low density of free carriers, termed as depletion region (W_D). The forward biasing conditions leads to a reduction in potential barrier height and then allow carriers to diffuse through the material, the depletion width is reduced. Figure 10b) shows the state of a forwards biased PN-junction, indicating that an external potential reduces the potential barrier across the depletion region to allow carriers to be injected to the depletion region, producing a current flow. The external voltage applied leads to a higher concentration of carriers than in the thermal equilibrium situation. In that case, quasi-fermi levels (EF_n-EF_h) are used to describe the electron and hole populations under non-equilibrium [28].

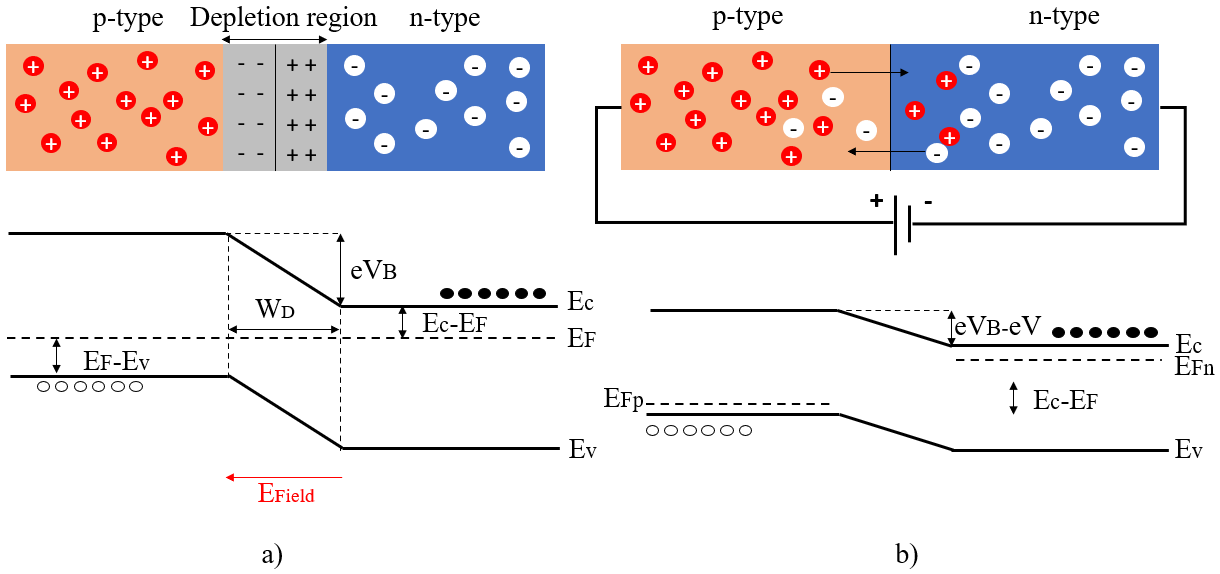

Figure 10: Energy band diagram of an unbiased (a) and a forward biased (b) PN-junction.

A heterojunction consists of two different semiconductors, one with a small bandgap and the other with a larger bandgap. The structure that forms two heterojunctions is so called ‘double heterostructure’, namely, a layer with a small bandgap sandwiched by two large bandgap layers [24]. Figure 11 schematically displays the difference in band diagram between a homojunction and a heterojunction in terms of carrier distribution. A heterostructure gives an enhanced confinement in carriers, leading to an increase in radiative recombination rate and thus an improvement in LED efficiency. Typically, high-performance LEDs active region relies on PN heterojunctions to enhance the radiative recombination rate.

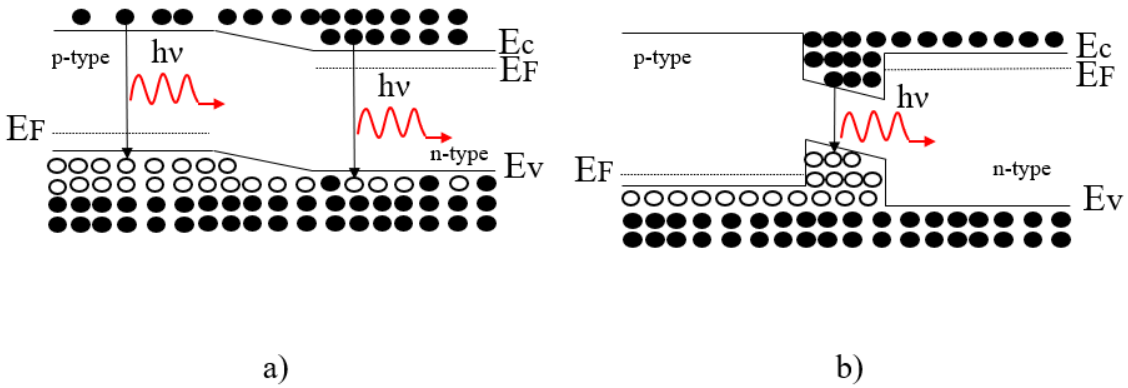

Figure 11: a) PN homojunction under forward bias. b) PN heterojunction under forward bias.

The heterostructure can spatially confine carriers in the active region of a LED, but some carriers may escape due to different reasons, such as different doping levels or different carrier mobilities between the n-type and p-type layers, low barrier height or high thermal energy. Therefore, an extra potential barrier is often necessary. An electron blocking layer (EBL) is often used for III-nitride emitters. In detail, an AlGaN electron blocking layer is used to create an extra barrier in both conduction and balance band, preventing electron leakage from the active region.

Active regions are commonly based on Multi Quantum Wells (MQWs) which generate carrier confinement in one direction, where the dimension of a quantum well is typically in the order of the Broglie wavelength (a few nm) to produce quantum effects (simply speaking, a number of extra, discrete energy levels in both the conduction band and the valence band which are so-called quantisation energy are generated, depending on the dimension of the quantum well) as shown in Figure 12. Therefore, when an electron and a hole recombine in a quantum well, the released energy includes the extra quantization energy in both the conduction band and the valence band. Figure 13 illustrates the typical GaN based LED and its band structure.

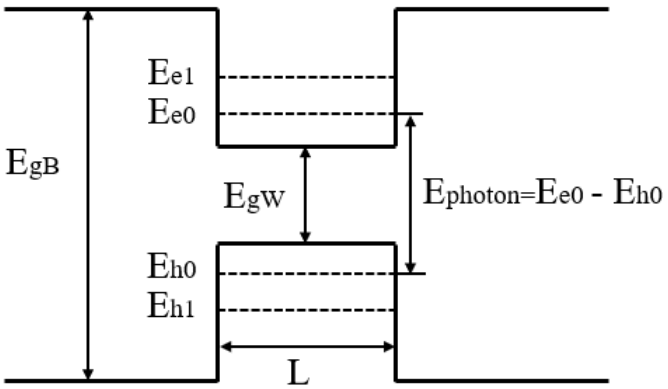

Figure 12: Band diagram of a Quantum Well.

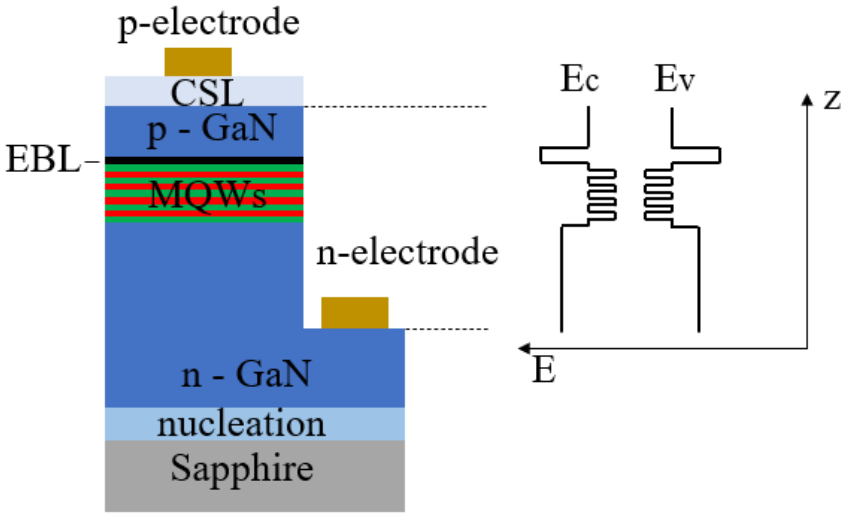

Figure 13: Schematic of a standard GaN LED on Sapphire and its band diagram energy.

2.1.4 Principles of laser diodes

The interaction of a semiconductor and photons can be quantitively described by using probability coefficients for absorption, spontaneous emission and stimulated emission rates, respectively [30]. A laser diode emits light via a stimulated emission process, under where one photon stimulates another photon such that all the photons generated exhibit the same wavelength, polarisation and direction. Figure 14 illustrates the three mechanics of stimulated emission.

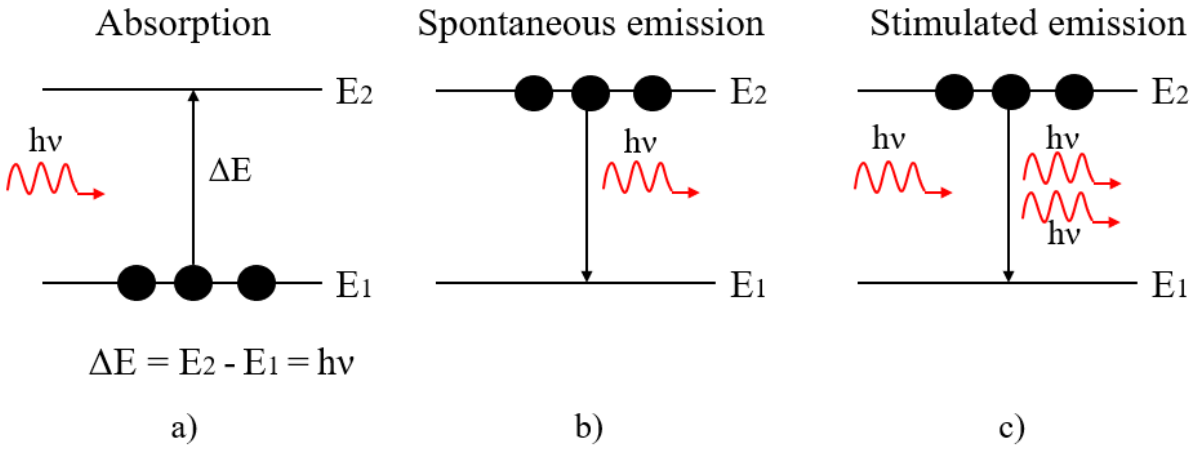

Figure 14: Scheme of a) Absorption b) Spontaneous emission and c) Stimulated emission.

Lasing can take place under a certain conditions, which is so-called population inversion, meaning that the population of electrons in the conduction band is greater than the valence band. Population inversion can be obtained by using heavily optical or electrical pumping. In order to achieving lasing, optical feedback is necessary. Figure 15 schematically illustrates a simple optical cavity, which consists of two parallel mirror facets and a emitter, where optical feedback is introduced through using the pair of mirrors. Due to the mirror facets, constructive interference occurs at resonant frequencies, leading to an

enhancement of light inside the cavity. The density of photons bouncing in the cavity increases, leading into threshold.

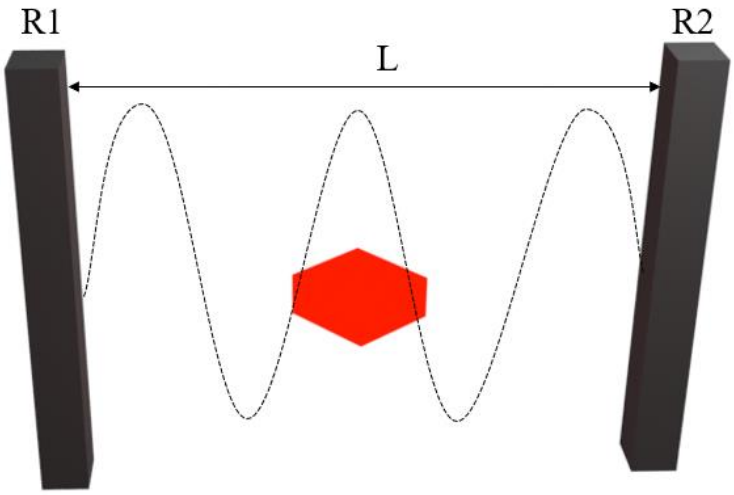

Figure 15: Diagram of a FP type cavity.

A threshold condition is achieved when the optical gain (G_{modal} i.e. gain of the light bouncing in the cavity) exceeds the optical loss. The material gain which can satisfy this condition is known as threshold gain. For a F-P laser the threshold condition can be expressed as:

$$G_{modal} = \Gamma g_{th} = \alpha_i + \alpha_m \tag{7}$$

Where Γ is the confinement factor, g_{th} is the threshold gain and α_i and α_m correspond to the intrinsic loss due to absorption, scattering and mirror loss, respectively [31]. The confinement factor is a dimensionless parameter that describes the overlap between the gain region and the optical mode field. The threshold gain is a property which is dependant of the carrier density. A reduction in threshold gain means that an inferior carrier density (and pump power) is required to obtain lasing. Therefore, it is necessary to minimise g_{th} for achieving a high-performance laser diode when designing a laser structure. The cavity losses are mainly dominated by the mirror loss, which can be expressed by:

$$\alpha_m = \frac{1}{L} \ln\left(\frac{1}{\sqrt{R1R2}}\right) \tag{8}$$

Where L is the cavity length and R_1 and R_2 correspond to the reflectivities of the two mirror facets [31]. As mentioned above, intrinsic losses are typically produced as a result of absorption and scattering.

The capacity of a cavity to confine light is determined by its quality factor (Q), which describes the relationship between energy stored and energy dissipated in the cavity. The Q factor is estimated by:

$$Q = \frac{\lambda}{\Delta\lambda} \tag{9}$$

Where λ is the resonant wavelength and $\Delta\lambda$ is the FWHM of the resonance [31].

Normally, the characterisation of a semiconductor laser involves the quantification of its Amplified Spontaneous Emission (ASE). The photoluminesce (PL) or electroluminescence (EL) spectra are acquired as a function of the excitation density, for high enough excitation density, the spontaneous emission is amplified, allowing the appearance of an ASE band in the spectra (if the material shows optical gain). The most used method to visualise ASE is by means of log-log plot of the integrated intensity and excitation density. The non-linear behaviour of the intensity and the narrowing in the spectral linewidth (FWHM) are the fingerprint of lasing devices [30,31]. Furthermore, once the device starts to lase, visual changes in the far-field pattern are observed.

2.2 III-nitride Vertical Cavity Surface Emitting Lasers (VCSELs)

2.2.1 Background

Laser diodes can be in either a surface emitting or edge-emitting architectures: namely, edge emitting lasers (EELs) and surface-emitting laser. EELs emit light from a facet which is perpendicular to the substrate, while Vertical Cavity Surface Emitting lasers (VCSELs) emit light along the surface of the epiwafer. Figure 16 illustrates these two kinds of device architectures. The first III-nitride laser diode (blue laser diode) is based on Edge Emitting Lasers (EEL) and was reported in 1996 by S. Nakamura [32]. Since then, such a blue laser diode have been widely used for a high density-optical storage application [33].

VCSELs exhibit different advantages in comparison to EELs due to their superior characteristics such as lower threshold current, single longitudinal mode operation, symmetric and low divergence angle and two-dimensional array capability [34]. Furthermore, the small cavity volume results in higher modulation bandwidth compared with standard EELs. All these characteristics make VCSELs attractive for many applications such as high-density storage systems, laser printing or micro projectors [35-37]. However, due to the vertical orientation, the gain region is smaller than EELs, therefore high mirror reflectance (>99%) is crucial.

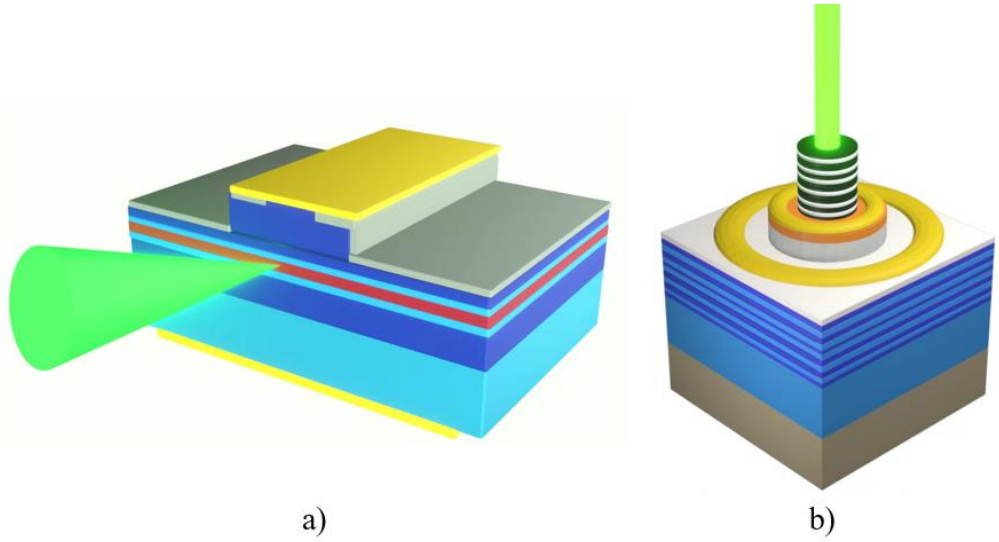

Figure 16: Schematic of an EEL (a) and a VCSEL (b) showing the emission direction and profile.

To form a VCSEL a cavity with an active region is placed between two reflectors. The design of a VCSEL is critical, as a bad design can lead into losses and reduce the chances of lasing. One of the key-challenges for the fabrication of III-nitride VCSELs is due to the difficulty in obtaining an epitaxial Distributed Bragg Reflectors (DBRs) with high reflectivity, where a typical DBR structure is due to many pairs of Al(Ga)N and GaN alternating layers. However, the lattice-mismatch between AlN and GaN and the small refractive index contrast between AlN and GaN pose great challenges in obtaining high reflectivity DBRs.

The first reported optically pumped GaN based VCSEL at room temperature was in 1996 [38], their structure consisted of 10µm GaN active region and 30 period $Al_{0.1}Ga_{0.6}N/Al_{0.12}Ga_{0.88}N$ top and bottom mirror. The threshold pumping was as high as 2.0 MW/cm^2 due to the low reflectivity of the mirrors (84%-93%). Arakawa et al. reported in 1998 the first hybrid VCSEL with lasing action at 77K, the bottom DBR consisted of an epitaxially growth of 35-pairs $Al_{0.34}Ga_{0.66}N/GaN$ with reflectivity of 97%, and a 6-pair TiO_2/SiO_2 dielectric top DBR with reflectivity of 98% [39]. In 1999 the room temperature blue wavelength VCSEL was reported by Someya et al [40].

The electrically pumped VCSEL presents even more challenges due to all the prejudicial effects of III-nitride devices. In 2008 the first continuous wave (CW) hybrid VCSEL at 77K was demonstrated by Tieng-chag Lu et al [41]. Their device was formed by 29 pairs AlN/GaN bottom DBR and 8 pairs Ta_2O_5/SiO_2 dielectric top DBR. A few months later, Higuchi et al. published the first CW VCSEL at room temperature, where both top and bottom DBR structures are based on dielectric SiO_2/Nb_2O_5 DBRs [42]. They removed the sapphire substrate

by using a laser lift-off technique and then wire bonding processes to transfer the VCSEL into Si substrate. The threshold current was 7 mA with an 8 μm aperture.

Low threshold current operation requiere the spatial overlap between the optical mode and the carriers in all the three dimensions. Over the past years, the common approach is to define a current aperture, in order to confine the carriers and the optical mode in the centre of the device. For the axial direction this is achieved aligning the quantum wells (QWs) with the anti-node of the standing optical waves, also referred as 'enhancement factor', which has a maximum value of two when a perfect overlap is achieved.

2.2.2 Anti-guiding effects

The last two decades have seen the evolution of VCSEL fabrication processes. Normally in most of the device layouts, electric current is injected through contacts on the top and the bottom side of the substrate. It is critical to achieve a good lateral current confinement in a predefined area so that injected carriers can be recombined effectively at the active region. The early development of VCSELs is mainly based on GaAs-AlAs and their alloys, as they have virtually identical lattice constants and exhibit a relatively large refractive index contrast, where an epitaxial distributed Bragg reflector (DBR) based on AlAs and GaAs provide a reflectivity of up to 99.9%. Furthermore, AlAs layers can be easily oxidized to produce current apertures, which also act as a waveguide to confine the optical lateral mode [43].

Unlike AlGaAs, III-nitride oxidised carrier aperture present a challenge itself. Several approaches have been proposed for current confinement in GaN-VCSELs such as plasma damage of p-GaN [44], ion implantation [45], and the generation of airgaps by photoelectrochemical etching [46]. The most common and simple approach relies on depositing an insulating layer (usually SiO_2) on a bare epitaxial wafer and form a circular aperture using dry-etching techniques, followed by the deposition of a current spreading layer, which normally is ITO to allow carriers to be injected efficiently. The diameter of the active region of the VCSEL also determines the lasing threshold, which can be reduced to a few microns to achieve the lowest threshold. However, it can also exceed 100 μm if a high-power output is desired. The confinement aperture formation involves tedious processing and can detrimentally affect the device characteristics due to sidewall damage caused by dry etching techniques, which becomes increasingly severe when the diameter is below 10 μm. Furthermore, another issue existing for current aperture is due to the parasitic anti-guiding effect in the lateral direction which is a source of losses leading to an increase in threshold currents and a lower output power. Figure 17b)

illustrates the anti-guiding effect described in [46]. The k vectors of a standing wave in a FP resonator can be described by:

$$ka = \frac{m\pi}{L}, Kc = \frac{m\pi}{L+\Delta}, with\ ka > kc \tag{10}$$

Where m is the mode number and Δ is the dielectric layer thickness, as $\Delta \ll L$, m can be assumed to be the same in both regions. The propagation modes can be generated using a common effective mode propagating constant (βeff), where the oblique angle of the k-vector in the cladding region is smaller than that the aperture region. In this case, the optical energy can be leaked out of the cavity region in the lateral direction during the FP oscillation, which is so called the anti-guiding effect [46]. This can be seen in Fig 17a), where the refractive index has a low value at the centre region, coinciding with the high positions of the standing wave, this will lead into a structure with higher refractive index at the outer edge of the aperture than the centre. Figure 17b) illustrates how the anti-guiding effect has higher impact in high-order linear polarised (LP) modes because of their lower βeff.

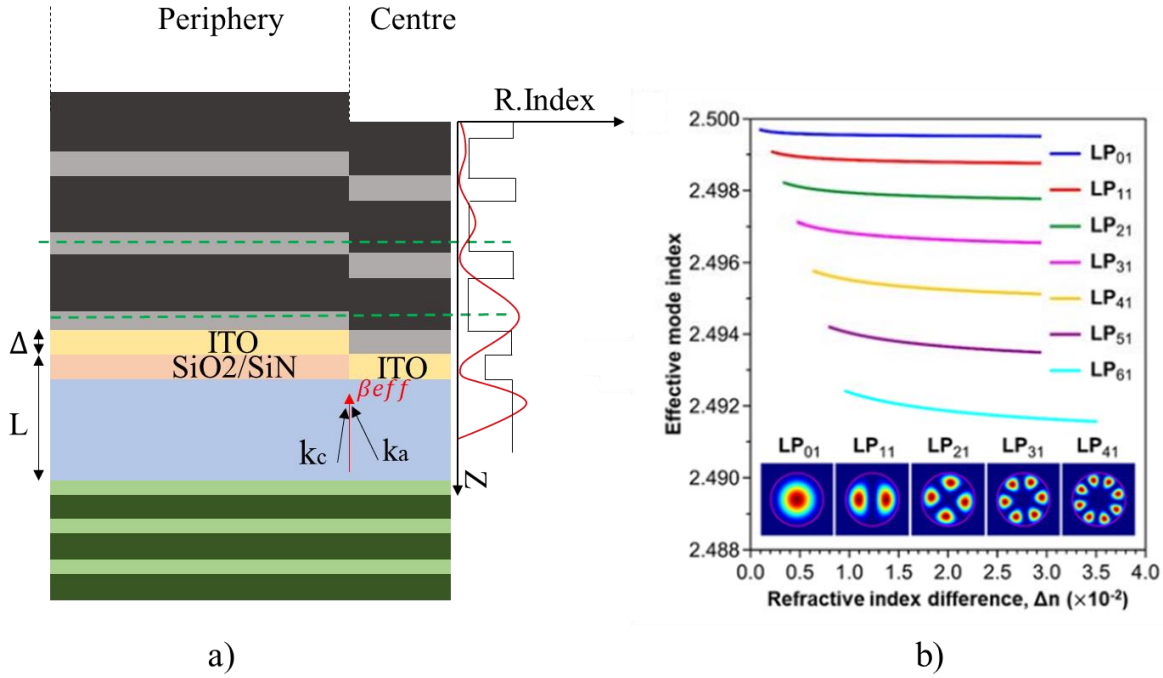

Figure 17: a) Schematic representation of anti-guiding effect due to dielectric aperture. Green dashed lines illustrate the areas where the refractive index is lower in the centre compared to the periphery. b) Calculated mode effective indices of a 6μm diameter VCSEL. Reproduced with permission from [46].

2.2.3 Distributed Bragg Reflectors (DBRs)

The key element of a VCSEL is due to bottom and top reflectors between which an active region is located. A DBR is a type of 1D photonic crystal, which consists of a stack of multiple alternating layers with different refractive indices. The stack

is formed by several pairs of alternating layers with high (nH) and low (nL) refractive indices. The number of pairs and the thickness of the alternating layers determine the reflectance and the centre wavelength, respectively. The spectral bandwidth of a DBR is greatly affected by the refractive index difference between its layers. Figure 18 illustrates the Fresnel reflection of light incident to a Bragg reflector.

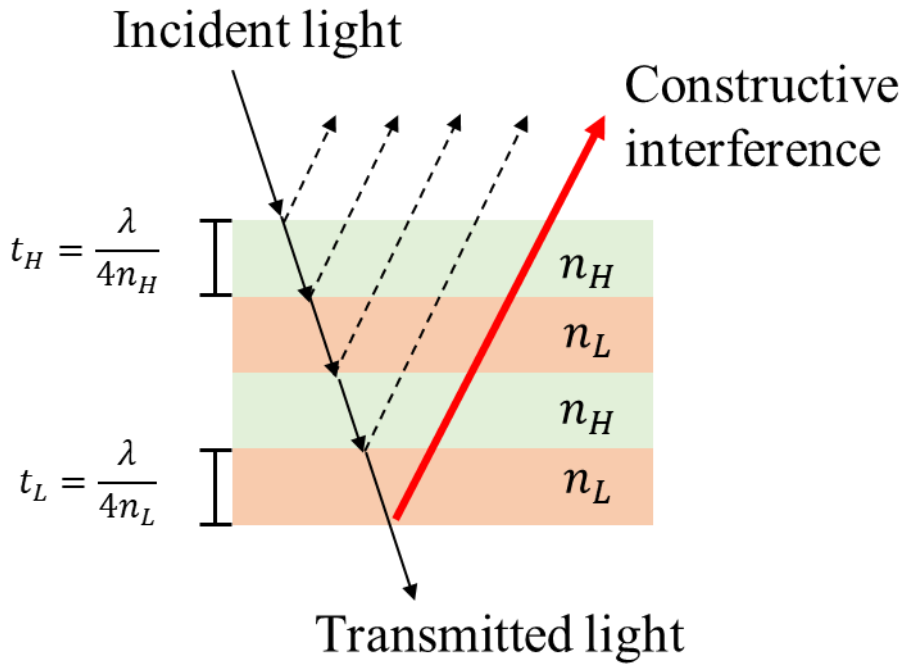

Figure 18: Schematic of the Fresnel reflection on a λ/4 DBR.

Typically, the optical thickness for each layer in each pair is equal to a quarter lambda and can be estimated by Equation 11, where λ is the centre wavelength and n is the refractive index. This specific thickness enables phase matched reflection at each interference so that the reflected constructive standing wave can be formed [47].

$$t_{12} = \frac{\lambda}{4n_{12}} \tag{11}$$

Where the peak reflectance can be estimated from Equation 12, where N is the total number of pairs of the stack, n_s and n_o are the refractive indices of the incident and the terminating medium [47].

$$Rpeak = \left(\frac{1 - \frac{n_s}{n_o}\left(\frac{n_1}{n_2}\right)^{2N}}{1 + \frac{n_s}{n_o}\left(\frac{n_1}{n_2}\right)^{2N}} \right)^2 \tag{12}$$

It can be observed that high reflectance values can be obtained even with low N values, if the contrast between n_1-n_2 is large (Δn). The stopband of a DBR is determined by the refractive index contrast. Equation 13 provides an estimation of the stopband of a DBR. Where $n_{eff}$is the averaged group index described by Equation 14.

$$\Delta\lambda = \frac{2\lambda\Delta n}{\pi\, n_{eff}} \tag{13}$$

$$n_{eff} = n - \lambda\frac{dn}{d\lambda} \tag{14}$$

The mirror losses described in Equation 8 are slightly modified when DBRs are used, as a portion of the optical field can be extended into the DBR with a finite penetration depth. Consequently, the equation is modified to:

$$\alpha_m = \frac{1}{L_{eff}}\ln\left(\frac{1}{\sqrt{R1R2}}\right) \tag{15}$$

$$L_{eff} = L_{penDBR1} + L_{cavity} + L_{penDBR2} \tag{16}$$

$$L_{penDBR} \approx \frac{\lambda}{4\Delta n} \tag{17}$$

Where, L_{eff} is the effective cavity length, $L_{penDBR1}$ and $L_{penDBR2}$ are the penetration depth of top and bottom DBR and Δn is the refractive index difference [47]. Figure 19 illustrates the effect of the refractive index difference (Δn) on the DBR reflectance. As mentioned above, the FWHM of the DBR and the peak reflectance are directly proportional to the refractive index contrast between the DBR materials.

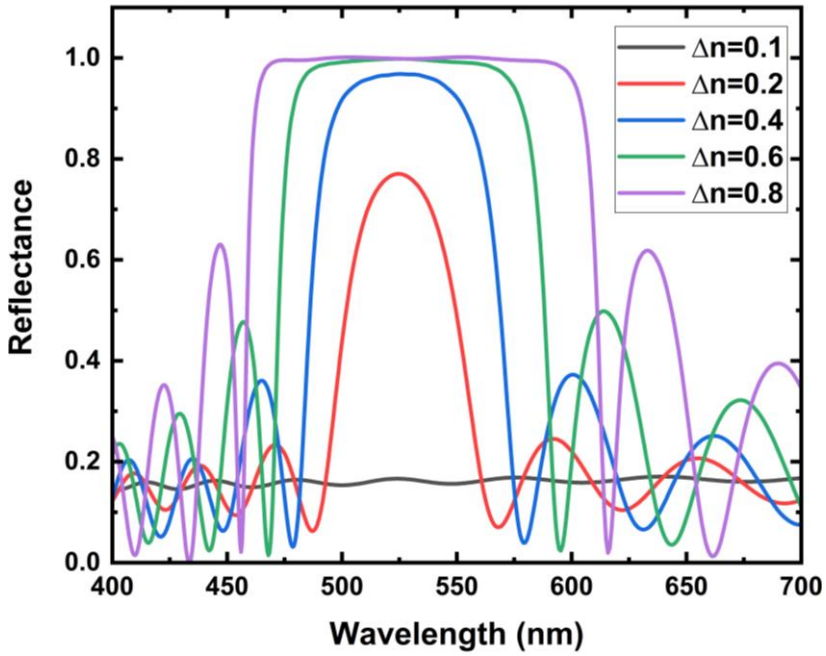

Figure 19: Simulated refractive index contrast Influence on reflectance of a DBR designed at 520nm.

2.2.4 Electrochemical etching of GaN to form nanoporous GaN (NP GaN)

As stated in the previous sections, a DBR structure with high reflectance of >99% is the key component of VCSELs. The lattice matched epitaxially growth of III-nitride DBRs have been demonstrated using $Al_{0.82}In_{0.18}GaN/GaN$ [48]. However, the growth rate of AlInGAN layers is 0.5μm/hr and the refractive index difference between them is only ~0.2. Consequently, more than 40 pairs are required to achieve high reflectance. Other approaches to obtaining epitaxially grown DBR are based on Al(Ga)N and GaN, where the refractive index of Al(Ga)N can be tuned by increasing Al content. However, with increasing Al content, the strain also increases, leading to the generation of extra dislocations and defects. The tensile strain also leads to cracking. Therefore, due to the low refractive index contrast (Δn ~0.3), a large number of AlGaN-GaN pairs (>35) is required in order to achieve a reasonably high reflectance [49-52]. Both approaches require long growth times. Furthermore, the bandwidth of the AlINGaN/GaN and AlGaN/GaN is narrow, which can become a problem during the fabrication of VCSELs as a little tolerance in the layer thickness in each pair would lead to the detuning of the reflectance wavelength, shifting the spectral position from the cavity mode.

In 2009, the first study of porous GaN formation was carried out [53], demonstrating an electro-chemical (EC) etching technique is an efficient approach to the fabrication of a lattice matched DBR. EC can selectively etch heavily doped GaN into nanoporous GaN (NP-GaN) while undoped GaN remain intact. It means that a pair of heavily doped GaN and undoped GaN can be

converted into a pair of NP-GaN and undoped GaN, leading to a large refractive index contrast. It has been confirmed that the bias used for EC etching process and the doping determines the porosity of NP-GaN, tuning the refractive index of NP GaN. The refractive index of NP GaN can be described by Volume Average Theory (VAT):

$$n_{eff} = [(1-\varphi){n_{GaN}}^2 + \varphi {n_{air}}^2]^{\frac{1}{2}} \quad (18)$$

Where φ corresponds to the porosity, and n_{GaN} , n_{air} are the refractive indices of GaN and the air [54]. This approximation is valid when the pore diameter is smaller the wavelength, specifically when the scattering factor is less than 0.2 $\left(\chi = \frac{\pi d}{\lambda} < 0.2\right)$. The refractive index of NP-GaN in DBRs has been reported to be as low as 1.65 [55]. Figure 20 illustrates a comparison between a 40 pairs AlGaN/GaN DBR and a 11pairs NP-GaN/GaN DBR, demonstrating the major advantages of NP-GaN based DBR.

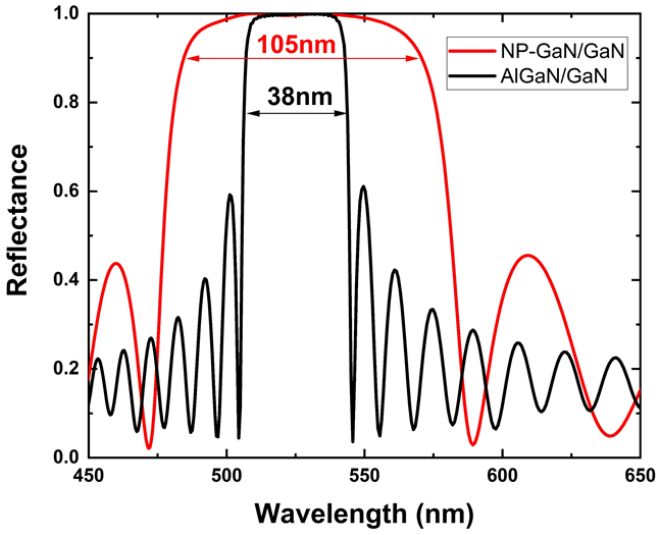

Figure 20: Simulated reflectance of a 40pairs AlGaN/GaN DBR and 11 pairs NP-GaN/GaN design at 520nm, where n-NP=1.9, n-GaN=2.44.

Prof Jung Han's research group provides a systematic study of the pore generation and pore evolution of c-plane GaN grown on sapphire under different EC etching conditions [56]. Figure 21 illustrates the phase diagram for EC etching, exhibiting pore size and pore density as a function of applied etching bias and doping concentration.

Our study has also concluded that for a fixed doping concentration, porous formation occurs at a narrow window in terms of applied bias. It means that below a certain point no etching can occur, while beyond bias heavily doped GaN can be completely etched away (i.e., electro-polishing). Our further study indicated

that the pore size increases linearly with applied voltage, but the porous density is determined by the doping concentration of heavily doped GaN.

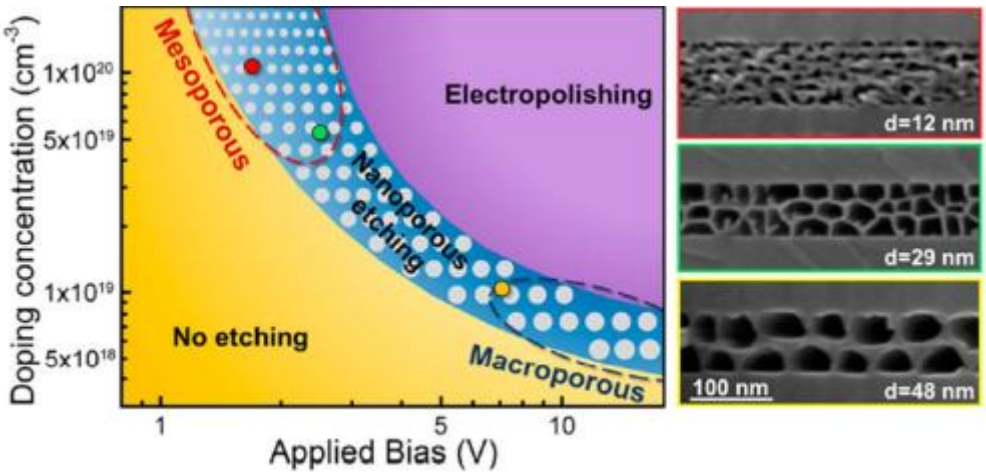

Figure 21: Phase diagram for EC etching. Cross section SEM images under different etching conditions. Reprinted with permision from American Chemical Society [56].

Two main types of EC etching processes have been studied. The first one is due to lateral etching, which can be achieved by initially depositing a dielectric layer on a heavily-doped GaN sample, followed by dry etching (using RIE or ICP) to form open trenches through the dielectric and n-GaN/GaN layers and then EC etching. Once EC etching starts, the acid flows into the sample from the sidewall due to the top protection of the initial deposition of the dielectric film, forming NP-GaN in a lateral direction only [57]. The pore distribution is highly uniform. However, the etching speed is limited to a few μm/min. Defect assisted EC etching has also been reported, meaning that the etchant flows through surface defects (pits) and etched vertically heavily doped n-GaN. In that case, etching is much faster (30 min for a 2inch wafer), depending on defect density [58]. This is certainly not ideal, as the need for dislocation paths would degrade the VCSEL formation by adding non-recombination centres and leakage paths. Furthermore, the threading dislocations can cause the acid to flow vertically, unintentionally porosifying other n++ GaN layers and thus affecting the properties of the finally formed DBR.

The mechanism of porous formation has been widely studied. In general, an EC etching process involves four steps: the generation of holes at the interference semiconductor/electrolyte, the oxidation of the exposed GaN surface, the dissolution of the oxidised layer by the etchant, and the merging of the reaction products into the solution [59]. The oxidation of GaN in EC reaction can be expressed as:

$$2GaN + 6h^{+} \rightarrow 2Ga^{3+} + N_2 \uparrow \qquad (19)$$

Where Ga^{3+} ions are dissolved in the electrolyte. Water oxidation also occurs, generating H_2 bubbling at the cathode.

The EC porosification process is mainly governed by the oxidation of GaN, driven by holes, which are created via Zener tunnelling or avalanche breakdown. The doping-concentration of n-GaN determines which mechanism governs the reaction. A band bending results from a negative applied potential at the electrolyte interface, the valence band at the interface is pulled to a higher energy than the conduction band in the bulk material. For high doping layers, the space charge region (SCR) becomes really narrow, enabling electron tunnelling from the interface valence band to the conduction band, leaving a hole. For low doped layers, the SCR is wider, avalanche breakdown is produced when carriers gain sufficient kinetic energy (obtained by acceleration under a high electric field) to cause electron-hole pairs by colliding with bound electrons [58]. Figure 22 illustrates these two mechanisms.

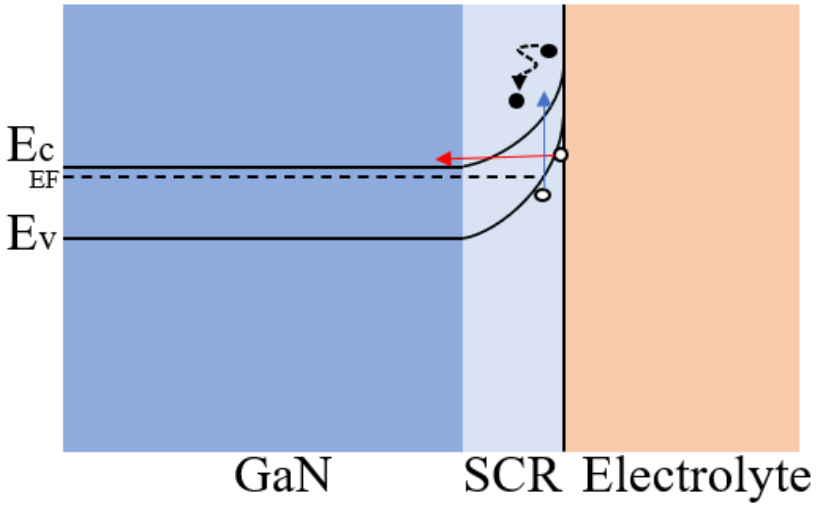

Figure 22: Band diagram of GaN/etchant showing hole generation mechanism. Adapted with permission from [58].

The basic EC setup is described in Figure 23. An indium pad is attached as an anode on the surface of a sample, while a platinum pad is used as a counter electrode. The electrolyte forms an ion transmission path between both electrodes, constant bias voltage is provided by a SMU. Furthermore, a stirrer is employed to maintain the EC process uniformly.

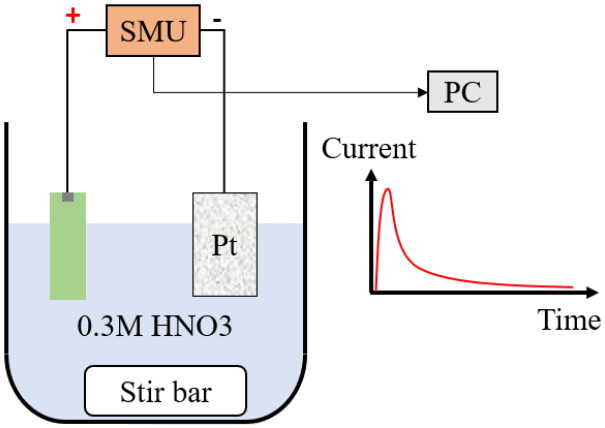

Figure 23: Set-up for GaN electrochemical etching.

2.2.5 Microcavities and Whispering Gallery Modes (WGM) in a microdisk laser

Light is confined in an optical cavity by resonant recirculation. Cavity modes are formed at different wavelengths, which are determined by the cavity size. In semiconductor lasers, coherent photon emission occurs when the emitting dipole is in resonance with the optical cavity mode. It is therefore crucial to understand how to tune the cavity resonances to match them with the emitter.

In 1946 Purcell proposed a theory that suggested that the environment of an emitter can change its spontaneous emission [60]. If an emitter could be placed in a microcavity, spontaneous emission can be significantly enhanced, as it modifies its local density of states (LDOS). The modified LDOS allows emission and absorption rates to be enhanced. Otherwise, a reduction in the recombination rate occurs when dipole and the cavity mode are not in resonance. This is so-called Purcell effect, which can be described by using Purcell factor.

The Purcell factor describes the enhancement of a dipole in a cavity compared to that in a free-space. If the Purcell factor is much greater than one, the exciton can radiate much faster in the cavity than in free space. The lasing threshold can be reduced if the Purcell effect is enhanced, as the spontaneous emission coupling factor (β) which is defined as the fraction of spontaneously emitted photons coupled to the cavity mode, would increase [61]. Equation 20 and 21 describe the Purcell factor inside a cavity and in a free-space [62]. The effective mode volume ($Veff$) is directly related with the cavity dimensions. The reduction of the effective volume of a cavity leads to the increment of the spontaneous emission factor. If the emission rate of an exciton is enhanced by the interaction with the cavity, the light produced by the exciton can be channeled into the cavity mode. Thus, the fraction of spontaneous emission in all the other modes is reduced. One of the fundamental sources of losses in lasers is spontaneous emission going to non-laser modes, therefore if we reduce it, the threshold can be lowered.

$$Fp = \frac{3}{4\pi^2}\left(\frac{\lambda}{nc}\right)^3 \frac{Q}{Veff} \tag{20}$$

$$Fp = \frac{\beta}{1-\beta} \tag{21}$$

The spontaneous and stimulated emission can coexist at the same resonant frequency in a sufficiently small cavity. Purcell factor and the coupling strength are enhanced when the size of the cavity is reduced. Therefore, microcavities present interesting properties as the local density of photon states can be increased by reducing their volume [63].

A resonator with circular geometry can sustain optical modes that bounce on its perimetry due to total internal reflection, where light can circulate around the edge of the resonator by following a critical angle according to Snell's law. The modes generated are termed as 'Whispering gallery modes' and were observed using sound waves at St Paul's Cathedral (UK) where sound can be noticed only in specific points (nodes) of the circumference [64]. The light can interfere constructively through all the reflections.

The spacing between modes, so-called free spectral range (FSR), depends on the cavity radius, which can be described by Equation 22, where λ is the resonance wavelength, R is the radius of the cavity and n is the refractive index of the cavity.

$$FSR = \frac{\lambda^2}{2\pi Rn} \tag{22}$$

Microdisk cavities are three-dimensional. The thickness of a cavity has to be properly designed in order to eliminate any vertical modes that can generate mode competition. Equation 23 describes the critical thickness that avoids the formation of vertical modes.

$$t_c = \frac{\lambda}{2n} \tag{23}$$

A higher β is desired in order to reduce the threshold, as more spontaneous emission is coupled to the lasing mode. Thus, is preferably to have a low number of cavity modes overlapping with the gain region. Therefore, thin microdisks with small diameters are desirable to achieve low threshold lasers.

Microdisk lasers have attracted much attention during the past years due to low lasing threshold, small mode volume and high-quality factor. Owing to excellent characteristics, WGM lasers have several potential applications, such as sensing devices, microdisplays, imaging, and on-chip integration [65,66]. Their structure

relies on a mirror-free structure, where the growth difficulties of III-nitride based DBRs previously mentioned disappear (Section 2.2.1). Due to these major features, microdisk lasers could potentially become an alternative option for VCSELs.

So far, most of the reports on lasing achieved from GaN based microdisk are under optical pumping, where a typic structure employs air as a cladding layer which can be obtained by using an undercut structure (forming a pedestal) fabricated by wet etching techniques [67-70], as shown in Figure 24. Consequently, a large refractive index contrast between GaN and air form an excellent cladding layer to confine the optical field along the axial direction. However, it is a great challenge to achieve an electrical injection microdisk laser due to poor electrical injection through the pedestal.

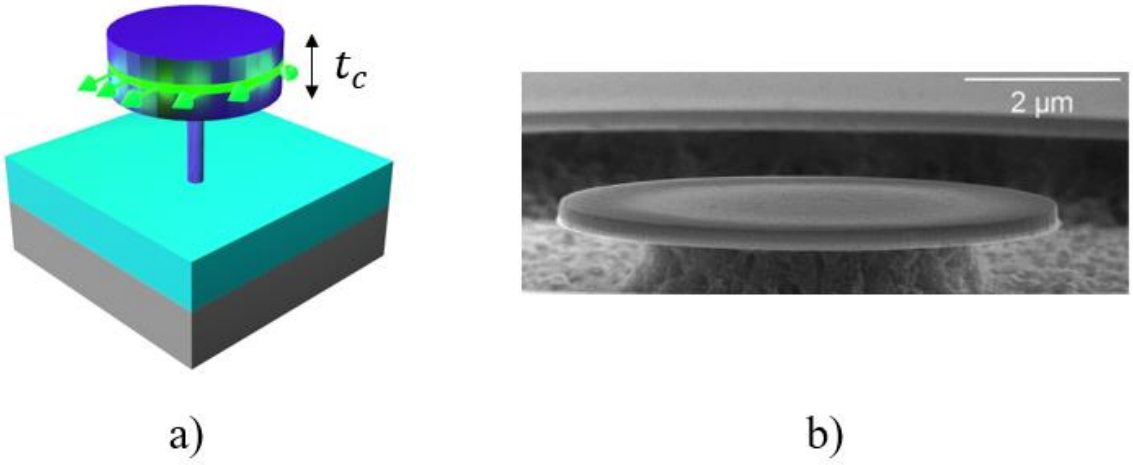

Figure 24: Schematic (a) and SEM image (b) of a undercut GaN microdisk. Reprinted with permission from [68].

2.3 References

[1] M. Fox, Optical Properties of Solids, 2nd ed. (Oxford University Press, Oxford, 2010).

[2] I. Vurgaftman and J. R. Meyer. Band parameters for nitrogen-containing semiconductors. *Journal of Applied Physics*, 94: 3675–3696, 2003.

[3] S. Nakamura and G. Fasol, The Blue Laser Diode: GaN Based Light Emitters and Lasers (Springer, Berlin, 1997).

[4] H. Xia, Q. Xia, and A. L. Ruoff, High-pressure structure of gallium nitride: Wurtzite-to-rocksalt phase transition. *Physical Review B* ,47:12925–12928, 1993.

[5] H. Morkoç, Nitride Semiconductors and Devices; Springer Science & Business Media, Vol. 32, 2013.

[6] E. Y. Chang, Realization of GaN-based technology for high power and high frequency applications. *IEEE International Conference on Semiconductor Electronics (ICSE2014)*, A3-A3, 2014.

[7] D. C. Look, and J. R. Sizelove, Predicted Maximum Mobility in Bulk GaN. *Applied physics letters*, 79 (8):1133–1135, 2001.

[8] D. K.Gaskill, C. D. Brandt and R. J. Nemanich, III-Nitride SiC and diamond materials for electronic devices. Materials research society Pittsburgh PA, Symposium Held April 8-12 1996, San Francisco, California, USA 1996.

[9] E. K. Sichel and J.I. Pankove, Thermal Conductivity of GaN, 25-360 K. *Journal of Physics and Chemistry of Solids*, 38 (3): 330, 1977.

[10] J. S. Blakemore, Semiconducting and Other Major Properties of Gallium Arsenide. *Journal of Applied Physics*, 53 (10):R123–R181, 1982.

[11] A. S. Kyuregyan and S. N. Yurkov, Room-Temperature avalanche breakdown voltages of p-N junctions made of Si, Ge, SiC, GaAs, GaP, and InP. *Soviet Physics Semiconductors*, 23 (10):1126–1131, 1989.

[12] C. Canali, et al., Electron, drift velocity in Silicon. *Physical Review B*, 12 (6), 2265, 1975.

[13] C. J. Glassbrenner and G. A. Slack, Thermal conductivity of silicon and germanium from 3 K to the melting point. *Physical Review*, 134 (4A): A1058, 1964.

[14] S. Nishino, J. A. Powell, H. A. Will, Production of large-area single-crystal wafers of cubic SiC for semiconductor devices. *Applied Physics Letters*, 42 (5), 460–462, 1983.

[15] M. E. Levinshtein, S. L. Rumyantsev and M. S. Shur, Properties of advanced semiconductor materials: GaN, AIN, InN, BN, SiC, SiGe; John Wiley & Sons, 2001.

[16] Razeghi, M., et al., Very high purity InP epilayer grown by metalorganic chemical vapor deposition. *Applied Physics Letters*, 52 (2): 117–119, 1988.

[17] S. Nakamura and S. F. Chichibu, Introduction to Nitride Semiconductor Blue Lasers and Light Emitting Diodes, 1 st ed. (New York and London: Taylor & Francis,2000).

[18] E. Xie. High performance microstructured light emitting diodes: mechanisms and processes. PhD thesis, University of Strathclyde, 2013.

[19] L. Zhang, et al., Photoluminescence studies of polarization effects in InGaN/(In)GaN multiple quantum well structures. *Japanese Journal of applied Physics*, 51:030207, 2012.

[20] P. Waltereit et al., Nitride semiconductors free of electrostatic fields for efficient white light-emitting diodes. *Nature*, 406:865, 2000.

[21] Y. Zhao et al., High-power blue-violet semipolar (20$\bar{2}\bar{1}$) InGaN/GaN light-emitting diodes with low efficiency droop at 200 A/cm2. *Applied Physics Express*, 4:082104, 2011.

[22] M. Funato et al., Blue, green, and amber InGaN/GaN light-emitting diodes on semipolar {11-22} GaN bulk substrates. *Japanese Journal of applied Physics*, 45:L659, 2006.

[23] Y. K. Noh, M. D. Kim and J.E. Oh, Reduction of internal polarization fields in InGaN quantum wells by InGaN/AlGaN ultra-thin superlattice barriers with different indium. *Journal of Applied Physics*, 110:123108, 2011.

[24] E. F. Schubert, Light-Emitting Diodes, 1st ed. (Cambridge University Press, Cambridge, 2003).

[25] G. H. Wannier, The structure of electronic excitation levels in insulating crystals. *Physics Review*, 52:191–197, 1937.

[26] S.-H. Park, J-J. Kim, H-M. Kim, Exciton Binding Energy in Wurtzite InGaN/GaN Quantum Well. *Journal of Korean Physical Society*, 45:2,582-585, 2004.

[27] E. Kioupakis, et al., Indirect Auger recombination as a cause of efficiency droop in nitride light-emitting diodes. *Applied Physics Letters*, 98:161107, 2011.

[28] S. M. Sze and M. K. Lee. Semiconductor Devices. Physics and Technology. 2013.

[29] H. Xiangyu. Design, fabrication and optimization of III-nitride micro light emitting diodes for optical communication. PhD thesis, University of Strathclyde, 2021.

[30] A. Einstein, Zur Quantentheorie der Strahlung (On the Quantum Theory of Radiation), *Physikalische Zeitschrift.* 18: 121–128, 1917.

[31] L. A. Coldren, S. W. Corzine, M. L. Mashanovitch, Diode lasers and photonic integrated circuits, John Wiley & Sons, 2012.

[32] S. Nakamura, InGaN-based blue/green LEDs and laser diodes. *Advanced materials*, 8(8):689-692, 2004.

[33] A.kuramata, K. Horino, K.Domen, GaN based blue laser diodes grown on SiC substrate as light source of high-density optical data storage. *Fujitsu Science and technical Journal*, 34:191-203, 1998.

[34] M. Koike, et al., Room Temperature CW Operation of GaN-based Blue Laser Diodes by GaInN/GaN optical guiding layers. *MRS Internet Journal of Nitride Semiconductor Research*, 5:1–7, 2000.

[35] S. Hashimoto, et al., GaN-based violet-blue laser diodes. *Procedings SPIE Laser Optics*, 4354, 2000.

[36] D. F. Feezell, Status and future of GaN-based vertical-cavity surface-emitting lasers. Proceedings Gallium Nitride Materials and Devices X, San Francisco, United States, 2015.

[37] H. C. Yu et al., Progress and prospects of GaN-based VCSEL from near UV to green emission. *Progress in Quantum Electronics*, 57: 1–19, 2018

[38] J.M. Redwing, et al., An optically pumped GaN-AlGaN vertical cavity surface emitting laser. *Applied Physics Letters*, 69:1-3, 1996

[39] T. Someya, et al., Lasing emission from an In0.1Ga0.9N vertical cavity surface emitting laser. *Japanese Journal of Applied Physics*, 37:L1424-L1426, 1998.

[40] T. Someya, et al., Room temperature operation of blue InGaN VCSELs by optical pumping, Conference on Lasers and Electro-Optics, Baltimore, USA, 1999.

[41] T.C. Lu, et al., CW lasing of current injection blue GaN-based vertical cavity surface emitting laser. *Applied Physics Letters*, 92:141102, 2008.

[42] Y. Higuchi, K. Omae, H. Matsumura and T. Mukai, Room-Temperature CW Lasing of a GaN-Based Vertical-Cavity Surface-Emitting Laser by Current Injection. *Applied Physics Express*, 1:121102, 2008.

[43] J.T. Leonard, et al., Nonpolar, III-nitride vertical-cavity surface-emitting lasers incorporating an ion implanted aperture. *Applied Physics Letters*, 107: 011102, 2015.

[44] G. Cosendey, et al., Blue monolithic AlInN-based vertical cavity surface emitting laser diode on free-standing GaN substrate. *Applied Physics Letters*, 101:151113, 2012.

[45] J. T. Leonard, et al., Nonpolar III-nitride vertical-cavity surface-emitting laser with a photoelectrochemically etched air-gap aperture. *Applied Physics Letters*. 108: 03111, 2016.

[46] C.Y. Huang, et al., Challenges and Advancement of Blue III-Nitride Vertical-Cavity Surface-Emitting Lasers. Micromachines, 12*:* 676, 2021.

[47] A. V. Kavokin and J.J. Baumberg, OVERVIEW OF MICROCAVITIES, Microcavities, 1st edn, Series on Semiconductor Science and Technology (Oxford, 2007; online edn, Oxford Academic, 1 May 2008).

[48] J.F. Carlin, et al., "Progresses in III-nitride distributed Bragg reflectors and microcavities using AlInN/GaN materials". *Physica Status Solidi (b)*, 242:2326-2344, 2005.

[49] M. A. Khan, et al., Reflective filters based on singlecrystal GaN/AlxGa1-x N multilayers deposited using low-pressure metalorganic chemical vapor deposition. *Applied Physics Letters*, 59:1449, 1991.

[50] I. J. Fritz and T. J. Drummond, AlN-GaN quarter-wave reflector stack grown by gas-source MBE on (100) GaAs. *Electronics Letters*, 31:68, 1995.

[51] J. M. Redwing, et al, An optically pumped GaN–AlGaN vertical cavity surface emitting laser. *Applied Physics Letters*, 69:1, 1996.

[52] T. Someya, et al., Lasing Emission from an In0.1Ga0.9N Vertical Cavity Surface Emitting Laser. *Japanese Journal of Applied physics*, 37:L1424, 1998.

[53] Y. Zhang, et al., A conductivity-based selective etching for next generation GaN devices. *Physica Status Solidi (b)*, 247:(7):1713-1716, 2010.

[54] M. M. Braun and L. Pilon, Effective optical properties of nonabsorbing nanoporous thin films. *Thin Solid Films*, 496:505− 514, 2006.

[55] S.M.-Ul-Masabih1, et al., Nanoporous distributed Bragg reflectors on free-standing nonpolar m-plane GaN. *Applied Physics Letters*, 112:041109, 2018.

[56] C. Zhang, et al., Mesoporous GaN for Photonic Engineering - Highly Reflective GaN Mirrors as an Example. *ACS Photonics*, 2, 7, 980–986, 2015.

[57] P.H. Griffin, et al., The relationship between the three-dimensional structure of porous GaN distributed Bragg reflectors and their birefringence. *Journal of Applied Physics*, 127: 193101, 2020.

[58] T. Zhu, et al., Wafer-scale fabrication of non-polar mesoporous GaN Distributed Bragg Reflectors via electrochemical porosification. *Scientific Reports*, 7:45344, 2017.

[59] P.H. Griffin and R.A. Oliver, Porous nitride semiconductors reviewed. *Journal of physics D: Applied Physics*, 53:38, 2018.

[60] E. M. Purcell, H. C. Torrey, and R. V. Pound, Resonance Absorption by Nuclear Magnetic Moments in a Solid. *Physical Review*, 69: 37–38, 1946.

[61] Q. Gu, et al., Purcell effect in sub-wavelength semiconductor lasers, *Optics Express*, 21:15603, 2013.

[62] W. W. Chow and S. Reitzenstein, Quantum-optical influences in optoelectronics—An introduction. *Applied Physics Reviews*, 5: 041302, 2018.

[63] Y. Rakovich and J. Donegan, Photonic atoms and molecules. *Laser & Photonics Reviews*, 4:179–191, 2009.

[64] L. Rayleigh, CXII. The problem of the whispering gallery, *The London, Edinburgh, and Dublin Philosophical Magazine and Journal of Science*, 20:1001– 1004, 1910.

[65] F. Vollmer and S. Arnold, Nature Meth. vol. 5, p. 591 (2008).

[66] G. Zhu, et al., Research Progress of Gallium Nitride Microdisk Cavity Laser. *Frontiers in Materials*, 9, 2022.

[67] G. Zhu, et al., Whispering-Gallery Mode Lasing in a Floating GaN Microdisk with a Vertical Slit. *Scientific Reports*, 10: 253, 2020

[68] S. Vicknesh, Fabrication of deeply undercut GaN-based microdisk structures on silicon platforms. *Applied Physics Letters*, 90:071906, 2007.

[69] F.Tabata, et al., Analysis of low-threshold optically pumped III-nitride microdisk lasers. *Applied Physics Letters*, 117: 121103, 2020.

[70] C. Zhao, et al., Ultra-low threshold green InGaN quantum dot microdisk lasers grown on silicon. *Applied Physics Letters*, 117: 031104, 2020.

[71] J. Selles, et al., Deep-UV nitride-on-silicon microdisk lasers. *Scientific Reports*, 6 :21650, 2016.

Chapter 3: Experimental and characterisation techniques for III-nitride optoelectronics

3.1 Experimental techniques

This chapter presents the fabrication techniques used during this research to fabricate emitters on a micro-scale. Characterisation methods such as Photoluminescence (PL) and Electroluminescence (EL) are also introduced.

3.1.1 Metal organic chemical vapour deposition (MOCVD)

Metal-organic chemical vapour deposition (MOCVD), also known as metal-organic vapour phase epitaxy (MOVPE), is a technique used to produce epitaxial layers for III-V materials (e.g. GaN, GaAs, or InP) compounds for electronic and optoelectronic devices.

The MOCVD used for sample growth in this thesis was based on a close-coupled showerhead (CCS), allowing the group III and V precursors to be vertically injected into the chamber. Figure 25 illustrates the reactor used through this thesis, which was able to growth three 2-inch wafers per growth run. The distance between the showerhead and the susceptor (e.g. where the substrates are hold) is very short ($\approx$11mm) to minimise potential parasitic reactions between group III and V precursors. The susceptor uses a high rotation speed to ensure crystal growth uniformity.

Figure 25: Aixtron 3x2" flip-top CCS reactor used through this thesis.

The precursors for group III elements gallium (Ga), aluminium (Al) and indium (In) were Trimethylgallium (TMGa), trimethylaluminum (TMAl), and trimethylindium (TMIn), while ammonia (NH_3) was chosen as group V element precursor. The GaN film originates on a substrate as the result of a series of

complex gas-phase and surface chemical reactions between group III and group V precursors that takes place on a substrate under high temperature. For example, the growth of GaN on sapphire requires a mixture of NH_3 and vapourised TMGa as the reactants. Like gaseous NH_3, the vapourised TMGa involved in the reaction must be carried from the bubbler (where the metal organic source is held) by a carrier gas, which is usually either pure hydrogen (H_2) or pure nitrogen (N_2).

3.1.2 Photolithography

Photolithography is a technique that allows us to transfer a predefined pattern in a photomask to an epiwafer by using a UV sensitive polymer (photoresist). In order to eliminate any unintentional photoresist degradation, photolithography is carried out in a yellow room under a cleanroom environment. Photoresists are classified depending on how they react with UV light. The exposed area of a positive photoresist becomes more soluble and can be then removed by immersing in a developer solution, while a negative photoresist exposure to UV light causes polymerisation, becoming insoluble and extremely difficult to be dissolved through development processes [1].

The standard photolithography process includes an initial epiwafer soft baking at 100 °C for 1 minute to remove moisture possibly left in a previous wafer cleaning process, aiming to improve adhesion with a photoresist. Subsequently, the sample is placed in a spin-coating system (EMS model 400 spin coater), where a photoresist is deposited and the rotational speed of the spinning stage causes a centrifugal force that spreads the photoresist, generating a uniform film thickness. The thickness of the photoresist can be controlled by tunning the acceleration profile and the dwell time. The mask pattern designed is exposed to 365nm UV radiation from a Karl suss MJB mask-aligner, shown in Figure 26. For this project, SPR350 has been used as a photoresist, and the spinner speed is set at 4000rpm and 30s dwell time. A diluted solution of MF26A is used to remove the exposed photoresist. After developing for 60 seconds, another soft bake dry process is carried out during 1 minute. The final thickness of the photoresist is around 1.2 μm.

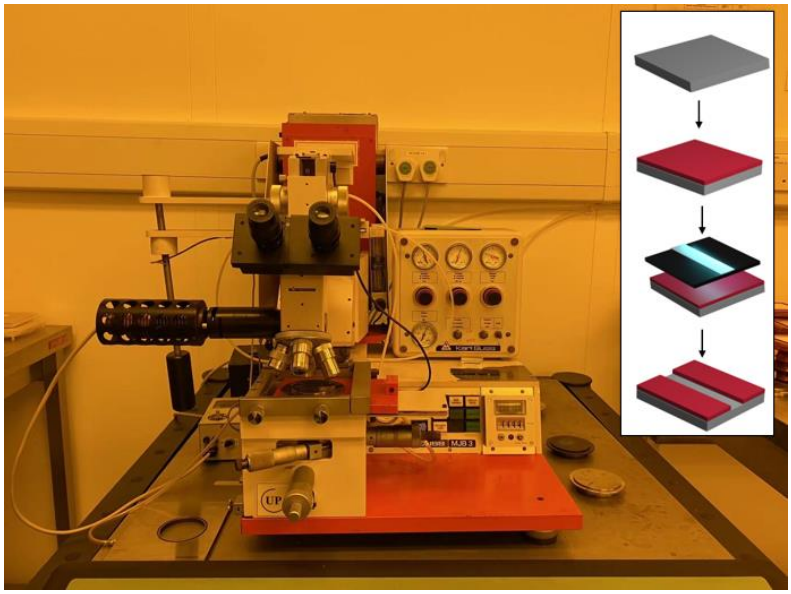

Figure 26: Karl suss MJB mask-aligner. Inset shows the standard photolithography process.

3.1.3 Etching techniques

3.1.3.1 Inductive coupled plasma etching

Dry etching process involves the utilisation of plasma and reactant gasses to etch undesired material. Two main mechanisms exist in plasma etching, physical ion bombardment and pure chemical etching. Ion bombardment relies on accelerating ions to collide with a sample and remove the material from the surface, the etching rate is highly dependent on the flux and energy of the ions. Besides, in a chemical process, the material surface is etched by free-radicals etchants forming volatile byproducts (i.e. $GaCl_3$) that are pumped out of the reactor. The etching rate is determined by the chemical reaction that occurs between exposed material and the gaseous environment [2].

Inductively Coupled Plasma (ICP) generates a high-density directional plasma by introducing gases above an inductive coil, placed around a ceramic tube with RF (electromagnetic induction). Figure 27 shows the Oxford Instrument Plasmalab System used in this work to etch GaN and SiO2. A mixture of Cl_2/Ar is used to etch GaN with high anisotropy. The etching rate is normally determined by the RF power used, which is usually kept a low level to minimise damage to sample (i.e. non-radiative recombination centres) [3,4]. Table 3 illustrate the conditions used to etch GaN throughout this thesis.

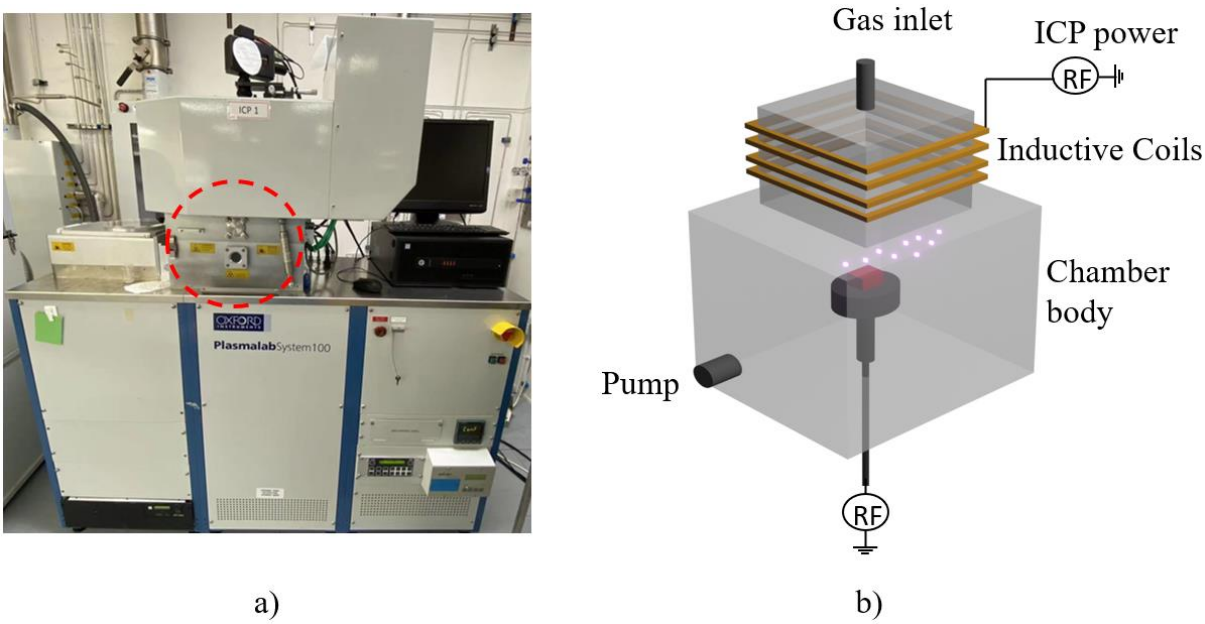

Figure 27: Plasmalab used during this project (a), schemattic representation of the ICP (b).

Table 3 : Etching recipe for GaN based materials

Pressure (mTorr)	ICP power (W)	RF Power (W)	Temperature (°C)	Ar flow (sccm)	SiCl4 flow (sccm)	Cl2 Flow (sccm)
4	450	150	20	4	1.5	15

3.1.4 Thin film deposition

The fabrication of p and n metal contacts is critical for high performance emitters. Two kinds of metal contacts are generally described, Schottky barrier and Ohmic contacts. Schottky barrier contacts form a large potential barrier (high resistance) at the interface between metal and semiconductor, while there is no potential barrier for ohmic contact and its current-voltage characteristic is ideally linear [5]. Figure 28 illustrates the current-voltage characteristics of the two types of contacts. Ohmic contact is necessary for the fabrication of III-nitride emitters. It is fairly straight forward to obtain Ohmic contact for n-type GaN [5], but more efforts are required to achieve ohmic contact for p-GaN. In order to form metal contacts, different deposition techniques can be used, followed by a thermal annealing process for metallisation to reduce the specific contact resistance.

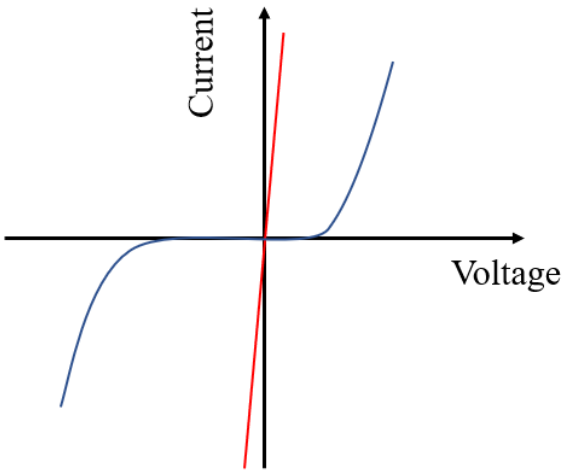

Figure 28:Schematic of the I-V characteristic of a Ohmic (red) and Schottky (blue) contact.

3.1.4.1 Metal thin film deposition

3.1.4.1.1 Thermal evaporation deposition and Electron beam deposition

A thermal evaporation is one of the traditional Physical Vapour Deposition (PVD) techniques that can be used to deposit a thin metal film under high vacuum conditions such as Al, Au, Ti, Ni. Figure 29 shows our Edwards system used for the deposition of n-contacts and bond-pads for LEDs and VCSELs. Another common method for thin film deposition is a sputtering technique. However, the lift off process becomes tedious as the deposition target is placed in an angle, enhancing sidewall deposition, the formation of a bi-layer structure can promote the lift-off. For thermal evaporation, high purity metals are placed in a tungsten coil. High current is applied through the coils to melt the metal, and the thickness of the deposited film is recorded by a quartz crystal monitor (QCM) placed besides the sample. The process is carried out under low pressure (~10^{-6}mTorr) allowing particles to travel directly to the sample, where condensation is produced. For this work a standard Ti/Al/Ti/Au was deposited to form the n-contact and Ni/Au was used as p-contact.

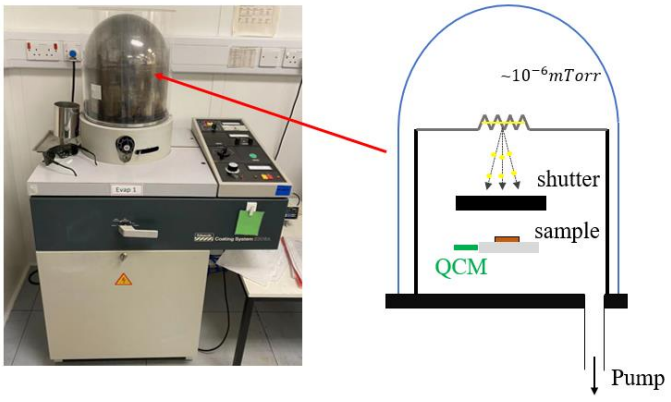

Figure 29: Edwards E used for thermal evaporation.

Electron-Beam physical vapour deposition

Indium Thin Oxide (ITO) or Ni/Au is commonly used to form p-contact for p-GaN. ITO offers better high optical transparency in the visible spectral region. In this work, ITO was chosen as a p-contact in Chapter 5, while Ni/Au was used in Chapter 4 and Chapter 6.

An E-beam technique is similar to the thermal evaporation technique described above, but a sample needs to be located on the top part of the chamber. An electron gun emits high energy (~10KV) electrons which bombard the desired target, i.e. solid ITO which is contained in a tungsten crucible. Due to the electron beam bombardment, the target material evaporates, allowing ITO to travel under low pressure and then deposit on the surface of the sample. The sample holder rotates at 10rpm to produce a uniform deposition. The deposited thickness is recorded by a crystal monitor.

Thermal annealing

A rapid thermal annealing (RTA) technique is used for thermal p-type GaN activation and contact metallisation [6]. Figure 30 illustrates our RTA system used during this project. A high temperature of up to 850°C can be reached. Annealing temperature is monitored by using a pyrometer accompanied by a thermocouple placed underneath the sample holder (carrier wafer).

Figure 30: Jipelec JETFIRST annealing system.

The activation of p-type dopants (Mg) was performed on an N_2 ambient at 700°C for 15 minutes. ITO annealing was carried out at 600°C in a mix air ambient (N_2/O_2) for 1 minute. More details about the ITO annealing optimisation can be found in Chapter 5.

3.1.4.2 Dielectric film deposition by PECVD

A Plasma Enhanced Chemical Vapour Deposition (PECVD) technique has been widely used to deposit dielectric layers such as SiO_2-SiN. Samples are placed in a vacuum chamber where reactant gasses are injected. For the deposition of SiO2, a combination of SiH_4-N_2-N_2O is used. The reaction takes place after plasma is formed between metal plates under a radio frequency wave. The quality of the films is higher than other CVD techniques. Furthermore, the deposition temperature of up to 300 °C can be controlled. Figure 31 shows our Plasma-Therm 790 used in this work.

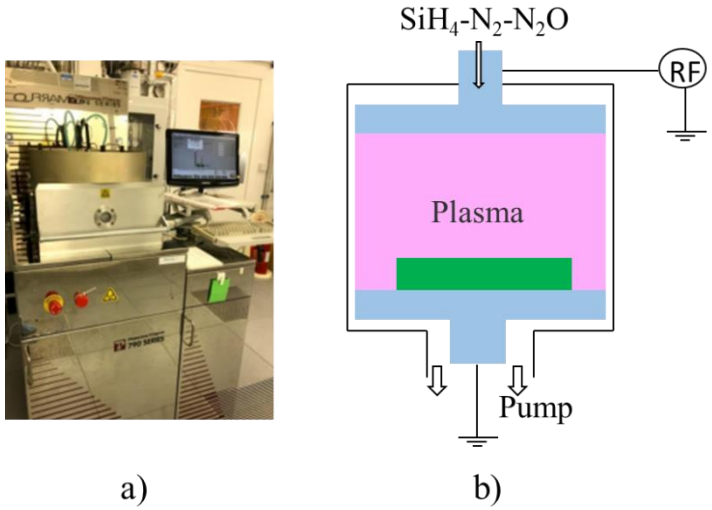

Figure 31: a) Image of Plasma-Therm 790 series PECVD system. b) Schemattic diagram of a PECVD.

A slightly modified version of PECVD is Inductive Coupled Plasma Chemical Vapour Deposition (ICPCVD), which has also been used in this work. ICPCVD allows the deposition of high-quality dielectric films at lower temperature (100 °C), preventing device degradation. Film thickness uniformity is also improved.

3.2 Optical and electrical characterisation

Characterisation techniques have been used in order to study the properties of the light emitting devices fabricated in this project. In the following sections, these techniques will be described in detail.

3.2.1 Photoluminescence (PL)

A photoluminescence spectroscopy is a non-destructive and non-contact technique used to study the optical properties of a semiconductor, such as band-gap, QCSE and crystalline defect [9]. A laser is used as an excitation source, the photon energy of the laser must be higher than the bandgap of the sample measured in order to optimally pump the active region. A 375nm continuous wave laser (Vortran Laser Technologies) is used as an excitation light for our PL system. The laser beam is incident and then focused on a sample with a diameter

beam spot of 200 µm via two high reflective Al mirrors and then lenses. The emission from the sample is then disperse by a monochromator and then detected by a cooled CCD detector. Figure 32 provides a schematic illustration of our PL setup used.

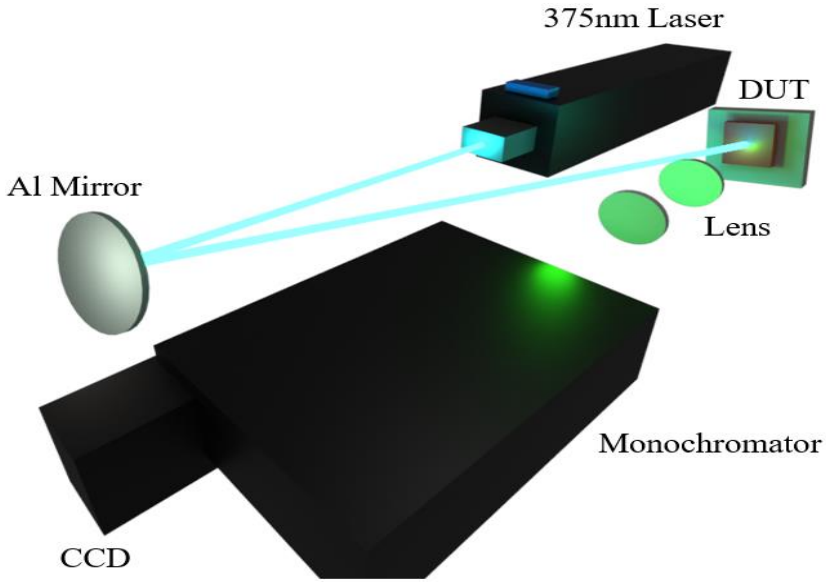

Figure 32: Schematic representation of our photoluminesence setup.

3.2.2 Confocal photoluminescence

Spectral imaging confocal microscopy has been measured by using WITec Alpha300. The principle is similar to the standard PL. However, in this case, a single point excitation and collection are both focused through a 10 µm pinhole. Therefore, light is rejected outside the image-plane, achieving a high lateral confocal resolution and imaging contrast. Figure 33 illustrates a simplified schematic diagram for our confocal spectral imagining system.

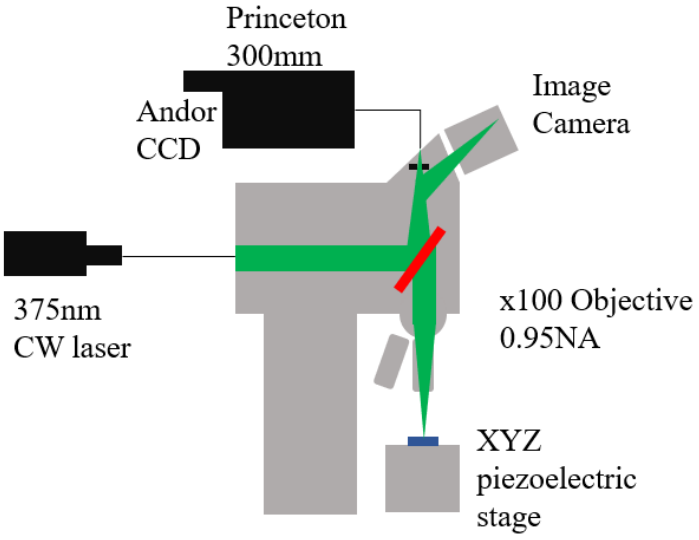

Figure 33: Schematic of the confocal microscopy system.

The sample position is controlled on a sub-nanometre scale using a 3 axis scan-stage with a lateral range of 100 x 100 µm and an axial range of 20 µm. A 375 nm diode laser supplied by Vortran Laser Technologies is coupled into a single mode fiber, which acts to eliminate any beam profile distortion. A 100x magnification objective with 0.95NA is used to focus and collect the light. Emissions are dispersed and then collected by Princeton Instruments SprectraPro 300i Czerny-Turner spectrometer and Andor Newton DU970N-UVB-353.

3.2.3 Micro-Photoluminesce

A micro-photoluminescence (µ-PL) system is a slightly modified version of the previously PL setup presented, which can spatially resolve photoluminescence. This system includes a 50x magnification objective, which allows the excitation laser to be focused into a beam with a diameter of 2 µm. Power dependant measurements are feasible due to a software that controls the excitation power. Figure 34 displays a schematic illustration of our micro-PL system employed. Two kinds of diode lasers are connected to this system: a 375 nm CW diode laser with a maximum power of 60 mW and a 375 nm pulse diode laser with an average power of 1 mW and a pulse width of 50 ps. The switching between the two diode lasers is achieved by using a flip mirror. The laser beam is reflected by 90° towards an objective by using a high reflectivity dichroic mirror (<99% at wavelengths shorter than 412 nm). Emission is collected through the same objective and then pass through a 50-50 beam splitter. The first part of the light is directed to a CCD imagining camera to visualize the sample surface. The remaining 50% is coupled into an optical fibre and finally connected with a 0.55m long iHR spectrometer which disperses the light. Emission is detected by a -70C TE cooled CCD array detector.

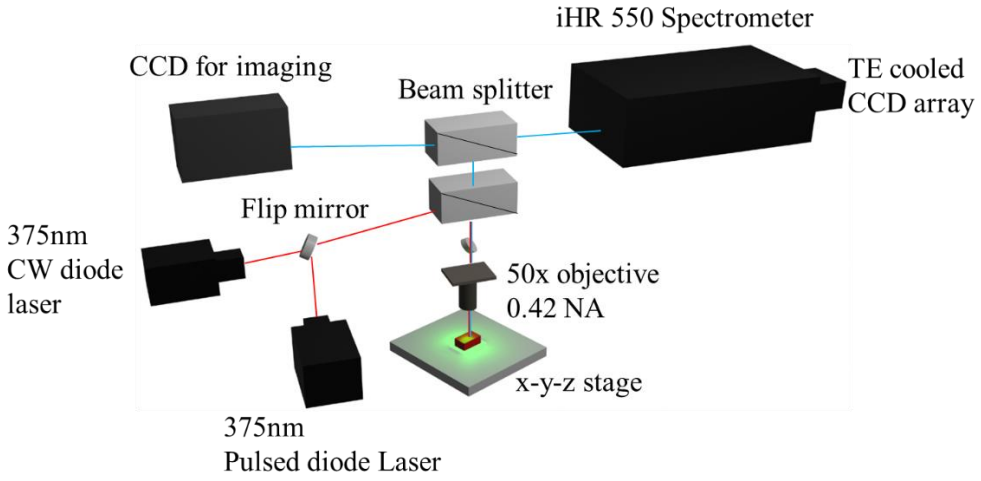

Figure 34:Schemattic diagram of the micro-PL system.

3.2.4 Electroluminescence (EL)

Electroluminescence is described as the formation of photons due to the recombination between and electron-hole under a forward bias. Figure 35 illustrates our home-made system used in this work. An optical microscope is mounted above the samples, equipped with a CMOS camera (XIMEA xiQ global-shutter) connected with a x12 objective (UltraZoom Navitar lens tube). Keithley 2400 SMU Current provides injection current into a device through the sample pads by using electrical probes. The emission is collected using an x50 magnification objective with 0.42NA. The emission with an area of 100x100um is observed. The collected emission passes through a 50:50 beam splitter and is then coupled into a fiber collimator. The emission spectra is recorded by using a Andor Newton CCD.

A standard XYZ motorised stage with a traveling arrange of 75 x 75 mm is used to allow for a focusing purpose. The system also includes a 360^{o} motorised rotation stage.

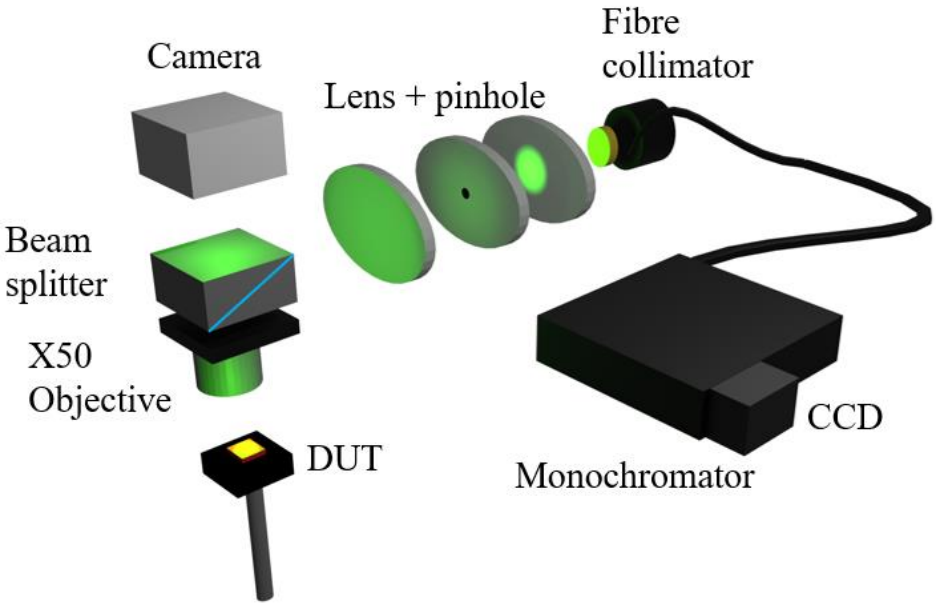

Figure 35: Schematic of the micro-EL setup used for spectrum characterisation.

3.2.5 Scanning electron microscopy (SEM)

Surface morphology can be measured on a high magnification (10-10^{5}) by using Raith EO Field-Emission Scanning Electron Microscope (FE-SEM). High energy electrons are emitted under vacuum conditions (10^{-5}mbar) with voltages ranging from 0.1 to 30KV. The electron beam is collimated and then focused on a testing sample after passing through several magnetic lenses [10]. The focus electron beam is scanned across a 3D topology. The bombarding electrons on a testing sample produce secondary electrons or back-scattered electrons, which are converted into electrical signals which reflect on the surface morphology of the

testing sample. The signals are finally converted into a 2D images. Figure 36 shows a schematic illustration of the configuration of a SEM machine.

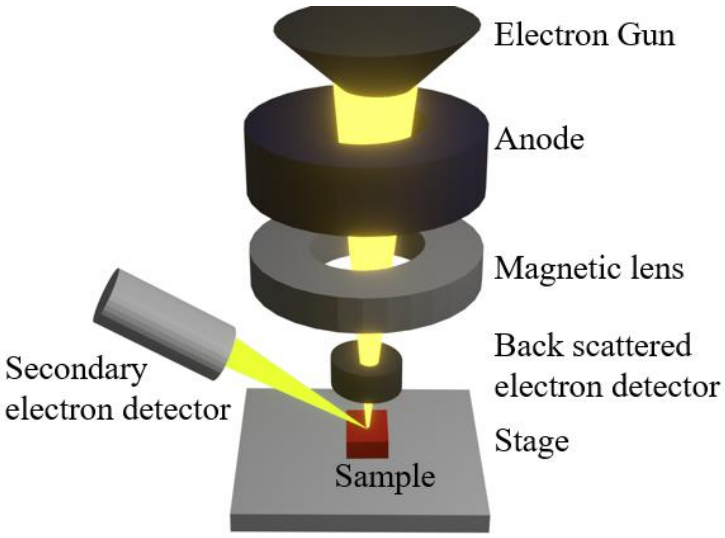

Figure 36: Schematic of an SEM.

3.2.5 Ellipsometry

Ellipsometry is a non-destructive technique which can be used to study the optical properties of dielectric materials. An ellipsometer measures the change of polarisation (Ψ) and phase difference (Δ) in a reflection or a transmission mode produced by a sample and compares it with a model. Typically, it can be used to measure the refractive index and the absorption coefficient of a film [11]. Figure 37 shows a schematic of a standard ellipsometer. A light source produces unpolarised light, which is then polarised and targeted to a sample, the reflection beam from the sample is collected and then detected by a detector. The collected information is compared to a calculated predicted response from a data input. Mean square error (MSE) is used to quantify the difference between curves. Chapter 6 discusses about modelling of dielectric layers to form DBRs.

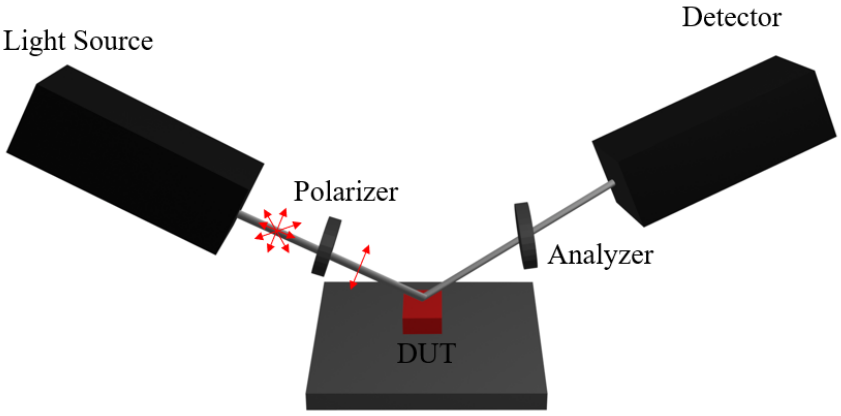

Figure 37: Diagram of an ellipsometer.

3.4 References

[1] S. Franssila. Introduction to microfabrication. John Wiley & Sons, 2010.

[2] S. M. Sze and K. K. Ng. Physics and properties of semiconductors a review. Physics of semiconductor devices, 3, 2006.

[3] J. K. Sheu, et al., Inductively coupled plasma etching of GaN using Cl2/Ar and Cl2/N2 gases. *Journal of Applied Physics*, 85:1970–1974, 1999

[4] Morkoç, H., Handbook of Nitride Semiconductors and Devices Vol. 1: Materials Properties, Physics and Growth. WILEY-VCH Verlag GmbH & Co. KGaA, 2008.

[5] T. V. Blank and Y. A Gol'Dberg. Mechanisms of current flow in metal-semiconductor ohmic contacts. *Semiconductors*, 41(11):1263-1292, 2007.

[6] J. K. Sheu, et al., The effect of thermal annealing on the Ni/Au contact of p-type GaN. *Journal of Applied Physics*, 83(6):3172-3175, 1998.

[7] M.F. Ceiler, P.A. Kohl and S.A. Bidstrup, Plasma-Enhanced Chemical Vapor Deposition of silicon dioxide deposited at low temperatures. *Journal of The Electrochemical Society*, 142:6:2067, 1995.

[9] S.G. Bishop, Characterization of semiconductors by Photoluminescence and Photoluminescence excitation spectroscopy. *Optical Characterization Techniques for Semiconductor Technology, Proc. SPIE* , 0276, 1981.

[10] K. C. A. Smith and C. W. Oatley, The scanning electron microscope and its fields of application, *British Journal of Applied Physics*, 6:391–399, 1955.

[11] P. Durgapal, J. R. Ehrstein and N.V. Nguyen, Thin film ellipsometry metrology, *AIP Conference Proceedings*, 449: 21, 1998

Chapter 4: Study of whispering gallery modes (WGM) in III-nitrides by FDTD

Small footprint microresonators, such as microdisk are one of the key components in photonic circuits. This chapter presents the state of the art of electrically injected III-nitride microdisk lasers. Then FDTD simulations of whispering gallery mode (WGM) in a conventional microdisk laser with an undercut structure (also known as pedestal) are discussed. A systematic study on an alternative approach based on micro-disk lasers with nanoporous GaN as a cladding layer instead of the undercut is presented. Furthermore, based on the simulation study, green emitting micro-disks have been fabricated and a detailed characterisation has been conducted, aiming at optical and electrical pumping. WGM modes have been observed under an optical excitation. Finally, an investigation of optical and electrical properties of InGaN MQWs has been conducted through *SiLENSE*.

4.1. Introduction

Micro or nano-cavities have been demonstrated in the fabrication of laser structures with excellent characteristics. Compared with edge-emitting lasers, microdisk lasers based on whispering-gallery mode (WGM) resonators have major advantages in terms of low threshold current, small mode volume and high-quality cavity factors (Q). This is particularly important for III-nitride lasers. These features allow them to be promising towards various fields, including optical storage, chemical and biological sensing, microdisplays etc [1-4]. However, so far, the fabrication of GaN based microdisk lasers mainly relies on the etching of a sacrificial layer to form an undercut structure, which provides vertical confinement due to the large refractive index difference between III-nitrides and air. Although this approach has achieved success in the fabrication of an optically pumped laser, the undercut structure compromises the current injection laterally (from p-GaN to n-GaN) and vertically (through the pedestal) [5-7]. Ultimately, more efforts are required in order to achieve an electrically injected laser.

Until now, the research on III-nitrides microdisk has been focused on GaN-on-Silicon substrates due to its low cost, low resistivity and high thermal conductivity. In 2018, the first electrically injected pulsed RT InGaN based microdisk was presented. Their device was based on a 20 µm diameter disk, with ‘pedestal-free’ architecture using AlGaN as a top and bottom cladding layer. The peak lasing was emitted at 412 nm with a lasing threshold of 250 mA [6]. In 2020,

the same research group achieved CW operation at 410 nm, while shrinking the diameter to 16 µm reaching a low threshold current of 18 mA [7]. Their study relied on the effect and suppression of unintentional incorporation of carbon impurities in the p-type AlGaN cladding layer. In 2021, a research group from Xiamen University reported a novel mushroom-type microdisk, based on a copper substrate and a copper pedestal [8]. Clear WGM lasing was observed under optical pumping. However, electrical injection lasing or the presence of modes was not achieved. Recently, a 20 µm diameter microdisk emitting in CW mode at 420 nm was reported [9]. Figure 38 illustrates the results typical characteristics of III-nitride microdisk lasers, previously mentioned. So far, electrically injected green emitting microdisk lasers have not been achieved either in GaN on Si or GaN or sapphire.

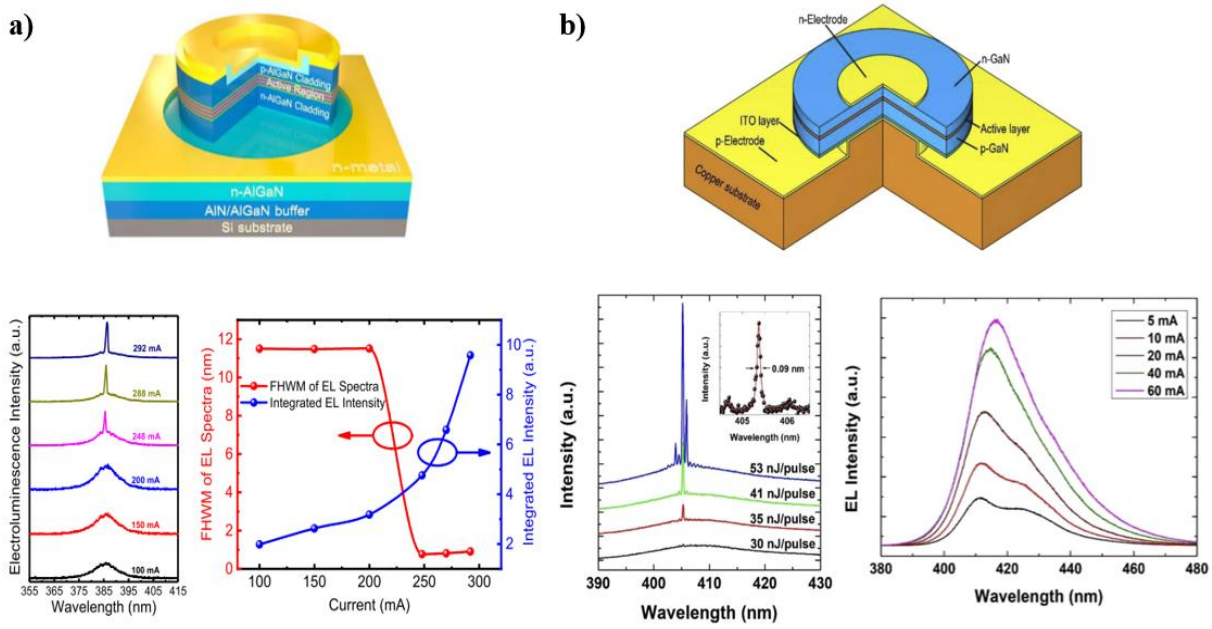

Figure 38: a) Pedestal free microdisk laser on Si. Reprinted with permision from American Chemical Society [9]. b) Mushroom approach showing lasing under optical pumping. Adapted with permission from Optics Express [8].

4.1 Finite difference time domain (FDTD) method algorithm

Finite-Difference Time-Domain (FDTD) is a powerful method used for solving Maxwell equations in complex geometries such as nano-scale optical devices. Although FDTD is a time domain method, a frequency solution can also be obtained by using Fourier-transforms. Therefore, useful properties such as transmission-reflection of light or the complex pointing vector can be calculated.

FDTD solves Maxwell's curl equation in non-magnetic materials:

$$\frac{\partial \vec{D}}{\partial t} = \nabla \times \vec{H} \tag{24}$$

$$\vec{D}(\omega) = \varepsilon_0 \varepsilon_r(\omega)\vec{E}(\omega) \tag{25}$$

$$\frac{\partial \vec{H}}{\partial t} = -\frac{1}{\mu_0}\nabla \times \vec{E} \tag{26}$$

where $\vec{H}$, $\vec{E}$, and $\vec{D}$ are the magnetic, electric, and displacement fields, respectively, while $\varepsilon_r(\omega)$ is the complex relative dielectric constant ($\varepsilon_r(\omega)$=n^2, where n is the refractive index).

Maxwell equations can be written in terms of their orthogonal field components producing six equations relating the electric (E) and magnetic fields (H): E_x,E_y,E_z and H_x,H_y,H_z. Assuming the independence of the fields of Z direction, and also that the structure in the Z direction is infinite, Maxwell equations are dived into two independent set of equations, formed by three vector quantities which only have a solution in the X-Y plane. These are commonly termed TE (transverse electric) and TM (transverse Magnetic). For the TM case, Maxwell equations are solved as:

$$\frac{\partial D_z}{\partial t} = \frac{\partial H_y}{\partial x} - \frac{\partial H_x}{\partial y} \tag{27}$$

$$D_z(\omega) = \varepsilon_0 \varepsilon_r(\omega) E_z(\omega) \tag{28}$$

$$\frac{\partial H_z}{\partial t} = -\frac{1}{\mu_0}\frac{\partial E_z}{\partial y} \tag{29}$$

$$\frac{\partial H_y}{\partial t} = \frac{1}{\mu_0}\frac{\partial E_z}{\partial x} \tag{30}$$

FDTD solves the set of equations on a discretised temporal and spatial grid, where each field component (E and H) is solved at a different location within the grid cell (Yee Cell). Figure 39 illustrates a typical representation of a Yee-Cell. *Lumerical FDTD solutions* is the software used through this thesis [10]. In these simulations a geometrical model of the structure was constructed in a 3D CAD environment, where material parameters were specified. Sources and monitors were used to inject and record electromagnetic fields into the simulation region.

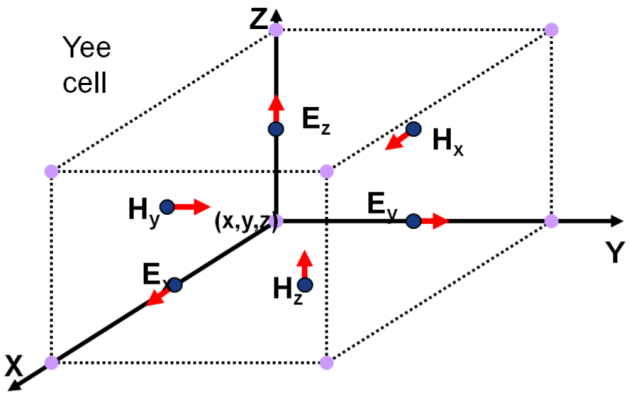

Figure 39: Representation of a Yee Cell. Reprinted with permission [10].

4.2 Modelling of WGM in microdisks based on an undercut structure

Dipole sources are used to produce electromagnetic fields, which can simulate point source radiators, such as the radiation from an emitter MQW structure [11-13].

In order to understand the spectral distribution of WGM modes, 3D FDTD simulations have been performed. To excite the WGM, broad band dipoles are placed at edge of the diameter of the 4 µm diameter microdisk to generate possible total internal reflection. The polarisation of the dipoles is in-plane to the InGaN MQW active region of a LED corresponding to TE polarisation which is dominant in InGaN emitters [14,15]. The dipoles are assumed to have a Gaussian emission wavelength of 520 nm with a FWHM of 50nm, emulating the measured PL of our green InGaN microLEDs. Figure 40a) illustrates the refractive index of the simulated microdisk structure, where the refractive indices of GaN and the active region are assumed to be 2.44 and 2.6, respectively. For simplicity, the active region has been defined as a single layer, instead of different MQWs-barriers. There is a minimum of ten mesh cells per wavelength in the simulation that runs for 5000fs. The electric field profile has been recorded at resonant wavelengths by frequency-domain power monitors. The simulation region is surrounded by perfectly matched layer (PML) absorbing boundaries on all sides. A series of 30 time-monitors are placed radially at the outer diameter of the cavity to record the WGM spectral distribution. Basically, the electric and magnetic field components are recorded as a function of time, the decay slope of the fields was used to determine resonant wavelengths and its Q-factor. Resonant modes have longer lifetimes than those off-resonance, so time the monitors are set to record data after 200fs, to avoid any initial transients of the dipoles.

Figure 40b) illustrates the spectral distribution of WGMs. The first order WGMs observed with a FSR (i.e. spacing between first order modes) of 8nm, which matches Equation 21 assuming the emission at 520 nm and a refractive index of

2.44. Furthermore, the second order WGMs can also be observed. Figure 40c) illustrates the Z-normal electric field distribution of the microdisk, labelled as $TE_{m,n}$ WGMs, where m and n are the radial and angular mode number order. Figure 40d) illustrates the electric field in the Y-normal axis, where a perfect overlap of the modal field and the active region is observed. The edge of microdisk has been marked by white dotted lines as a reference.

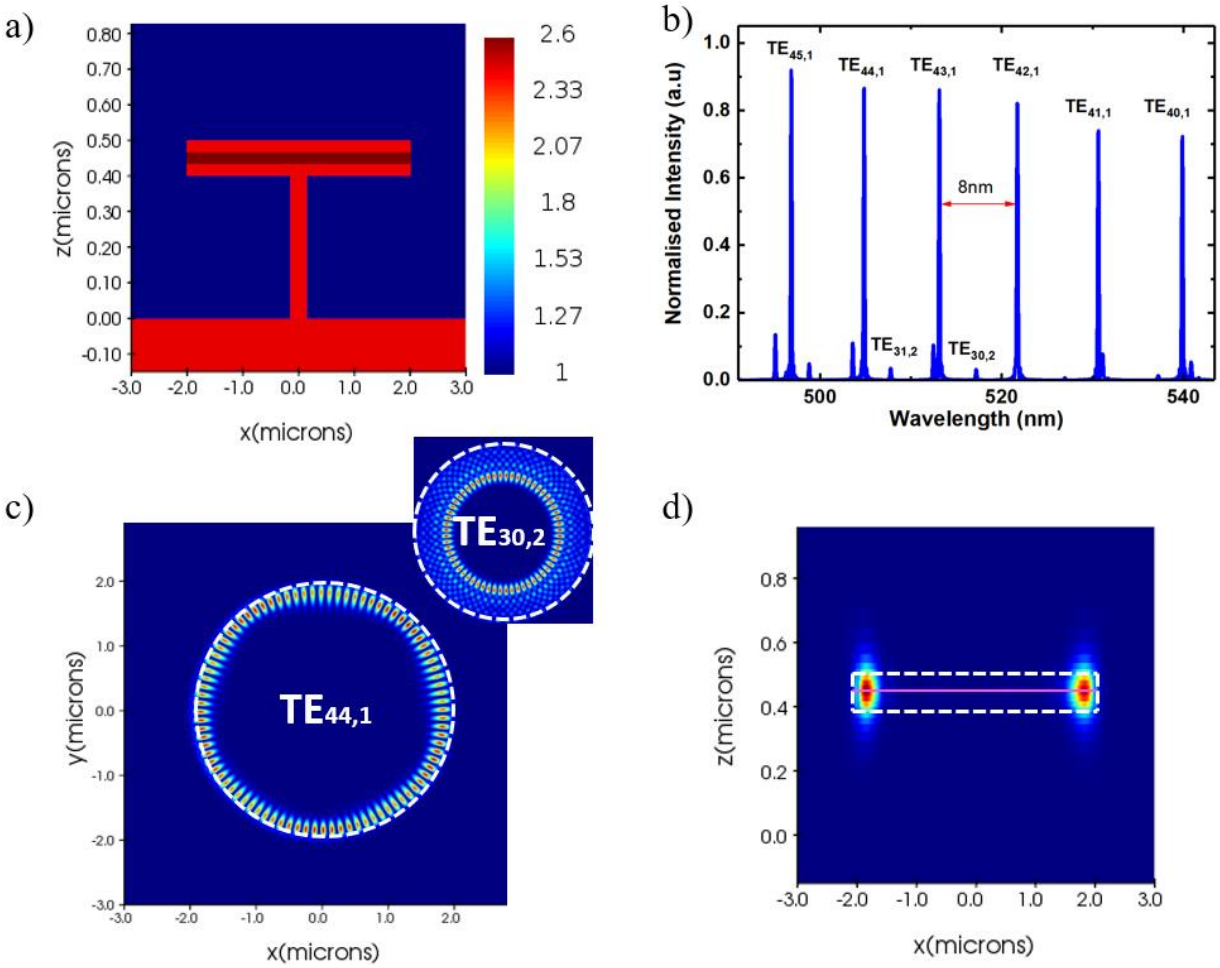

Figure 40: a) Refractive index map of 4µm diameter disk. b) Simulated spectral mode distribution. c) Electric field represnetation normal to Z, where red and blue represent the highest and lowest field intensity. d) Electric field represnetation normal to Y, where the pink line represents the active region.

The previous results showed the existence of WGM in a thin microcavity structure, which can be valid for optical pumping. However, the thickness of the active region of an III-nitride emitter is typically around 100 nm. Furthermore, an electrically pumped microdisk laser requires a p-type layer which is necessary for not only confining light, but also providing hole injection into the MQWs. The same procedure previously described has been used to simulate a thick pedestal structure, which is 500nm thick.

Figure 41a) illustrates the profile of the refractive index of a simulated microdisk. Electromagnetic fields are injected by dipoles using the same approach

previously described. Figure 41b) shows the mode spectra of such a structure which forms a thick microcavity. Although the spacing between fundamental WGM modes is 8 nm, several extra modes appear between them which are due to either FP modes along the vertical direction or hybrid modes (WGM-FP modes). The presence of the extra modes generates a mode-competition which potentially increase the lasing threshold [16-18]. Figure 41c) illustrates the electric field distribution along the Z and Y directions, respectively, indicating that the modal fields extend to the outside of the active region. This would have a negative impact in the confinement factor, Q-factor and mode volume, leading to a reduction in Purcell-enhancement.

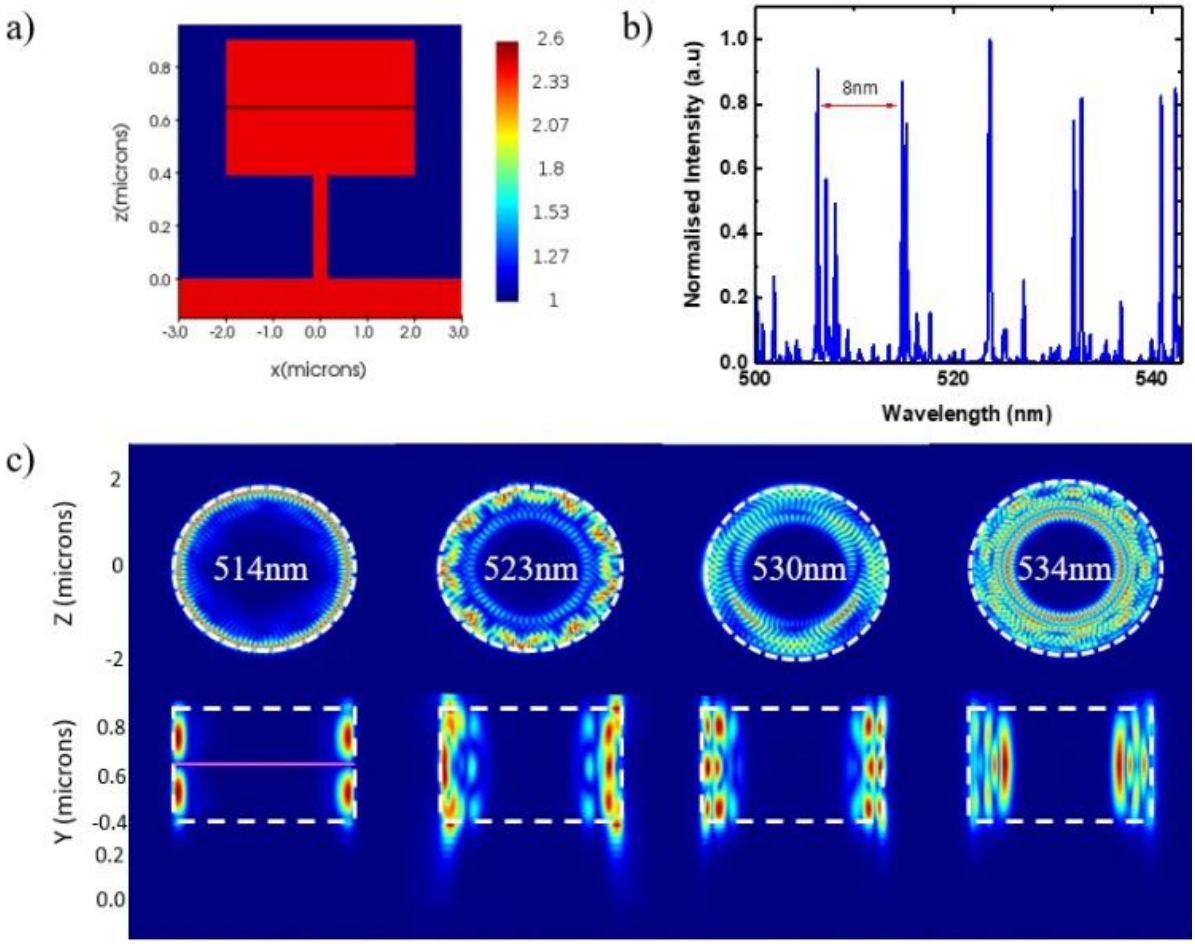

Figure 41:a) Refractive index map of the simulated thick pedestal cavity. b) Spectral mode distribution c) Electric field distribution Z-normal (top) and Y-normal, where the MQW has been outlined with a pink line.

Figure 42, illustrates the simulated Q-factor for a thin and a thick pedestal structure, respectively. The first order WGM have been marked with a red circle. As can be observed, the thick cavity led to lower Q-factor modes.

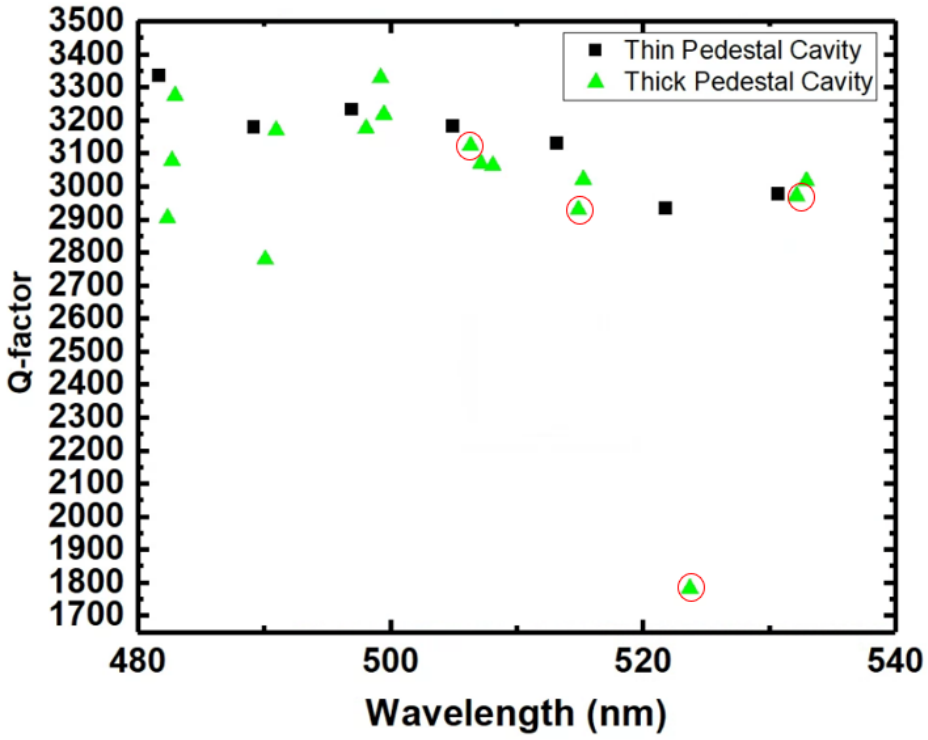

Figure 42: Simulated Q-factor of thin and thick pedestal cavities. The main WGMs in the thick pedestal has been rounded with a circle.

4.3 Modelling fabrication and characterisation of microdisks with nanoporous cladding layers

Even if WGM lasing has been achieved in an undercut structure, there is a great challenge associated with carrier injection, which is the major barrier for achieving electrically injected microdisk lasers.

Theoretically, a high refractive index contrast between a cladding layer and a cavity lead to a confinement in the fields of an active region. Typically, III-nitride materials use AlGaN as a cladding layer [19-25], while AlGaN generates tensile strain on a GaN surface due to the lattice-mismatch. Therefore, a trade-off between a high index contrast (labelled as Δn) and the tensile strain limits the Al composition in AlGaN to be less than 10%, giving $\Delta n < 0.04$. As described in Chapter 2, heavily doped n++ GaN can be porosified by using an electrochemical etching technique, significantly reducing its refractive index. This leads to a significant enhancement in Δn, up to 0.5 [19]. Furthermore, porous GaN is conductive, and such porous GaN as a cladding layer could be an alternative option for being used to replace a pedestal structure, forming a conductive channel for injecting current to achieve an electrically injected microdisk laser.

A 3D FDTD simulation has been carried out to simulate the effect of such a porous GaN based microdisk. The effective refractive index of porous GaN is assumed to be 1.9, taken from [19]. The injection of the fields and data collection

have followed the same approach described in the previous section. In fact, the position of the dipoles and time monitors remained unchanged. The simulated model spectrum shown in Figure 43b), illustrates that either vertical FP modes or hybrid modes disappear. Figure 43c) also provides the comparative data for a pedestal structure and a GaN porous based structure in terms of Q-factor, where a higher Q factor is obtained for the porous GaN disk.

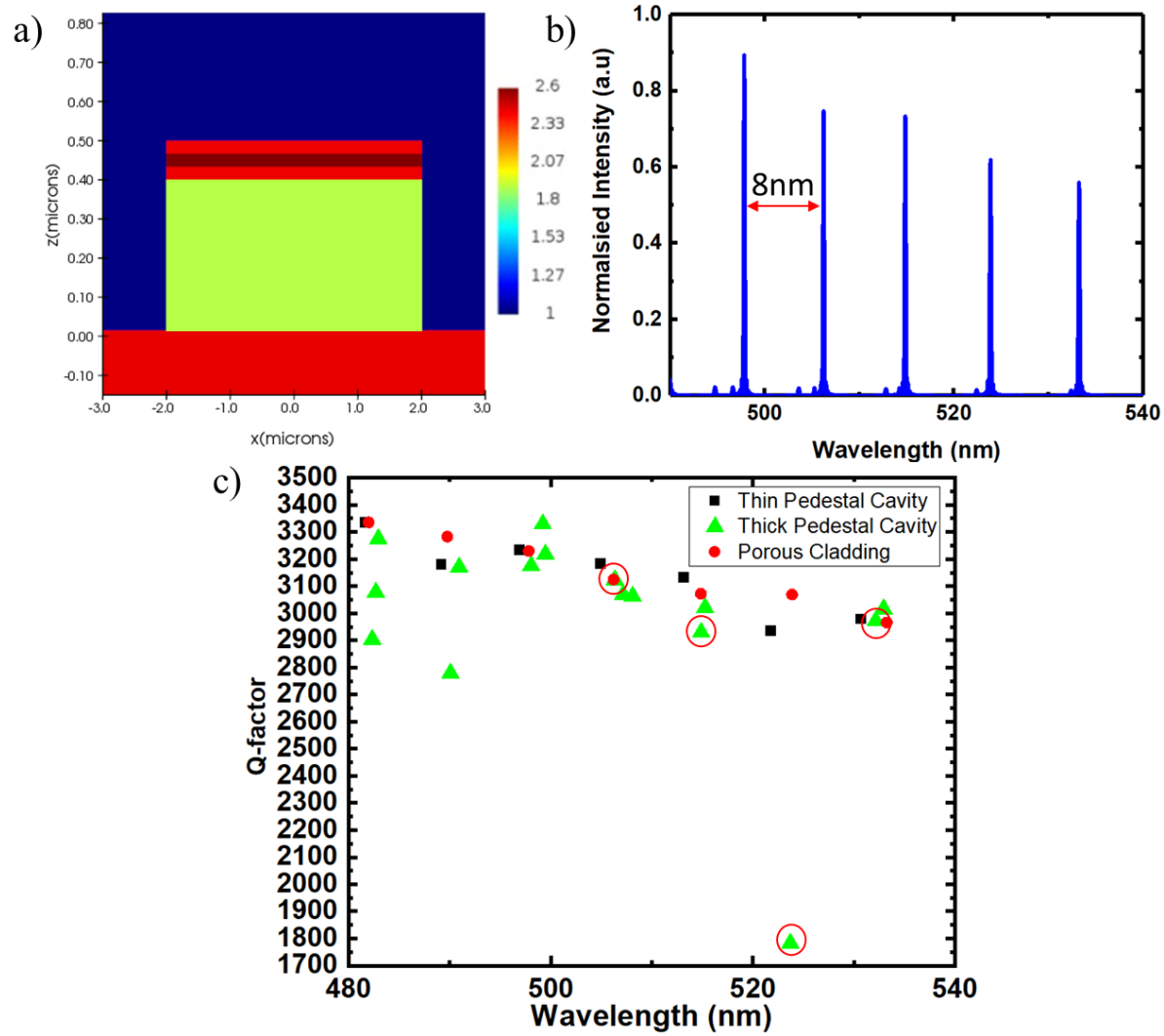

Figure 43: a) Refractive index map the simulated structure. b) Simulated WGMs with porous cladding layer. c) Simulated Q-factor of the three different kinds of cavities mentioned.

The presented results showed the potential of porous cladding layer to replace AlGaN. Thus, to validate the results, microdisks were fabricated. The samples were grown on c-plane sapphire using our MOVPE (Aixtron 3×2" flip-top CCS reactor). First, by using a standard two-step growth approach, a 6 µm-thick GaN layer was grown, followed by the growth of a 500 nm heavily doped n++$Al_{0.01}$GaN as a cladding layer, a standard 5 periods of $In_{0.27}Ga_{0.83}N$/GaN MQWs were then grown with the thicknesses of the barrier and quantum well of

12 nm and 2.5 nm, respectively. The emission wavelength of the MQWs is designed to be 520 nm.

Electrochemical etching was carried out under 7V bias at room temperature for 30 minutes. The electrolyte used was a solution of 0.3M HNO_3, which was constantly stirred during the etching process using a magnetic bar.

Once the AlGaN cladding layer was porosified, the sample underwent a patterning process and then a dry-etching process to form micro-disks with a 5 µm diameter. Figure 44, which shows a SEM image of the porous GaN based microdisk. Although the porous formation is successful, the sidewall of the microdisk show an inclination of 44 degree with respect to the vertical direction.

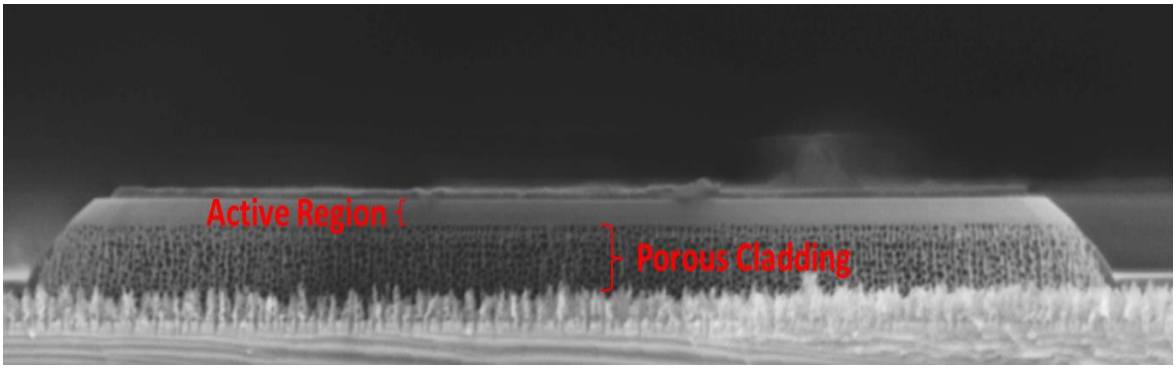

Figure 44: Cross section SEM image of a 5µm diameter Rod with nanoporous cladding layer.

Optical characterisation has been carried out by using our micro-PL system, as shown in Figure 45, which demonstrates the excitation power dependent PL spectra of a microdisk with porous GaN and a microdisk without porous GaN, respectively. The PL spectra of the microdisk without porous GaN shows equally spaced peaks separated 5 nm apart, which does not match with WGM free spectral range. The emission suffers a clear blue shift due to QCSE. In contrast, the microdisk with porous GaN shows sharp peaks uniformly distributed with a spectral spacing of 10nm which roughly agrees well with the WGM simulated. Modes are only observed on the low-energy side of the MQW spectrum, which is typical for GaN based microdisk with MQW as an active region, probably due to the reabsorption of high energy photons before coupling to cavity modes [27-32]. The peak at 507nm has been fitted through Lorentz fitting, which gives a FWHM of 1nm at 15mW. A spectral red shift can be seen between 15mW and 20mW, probably attributed to heating effects. The further increase in excitation power leads to more redshift, broadening and a decline in intensity. Although lasing has not been clearly observed, the great potential of porous GaN as a cladding layer for a microdisk laser has been demonstrated.

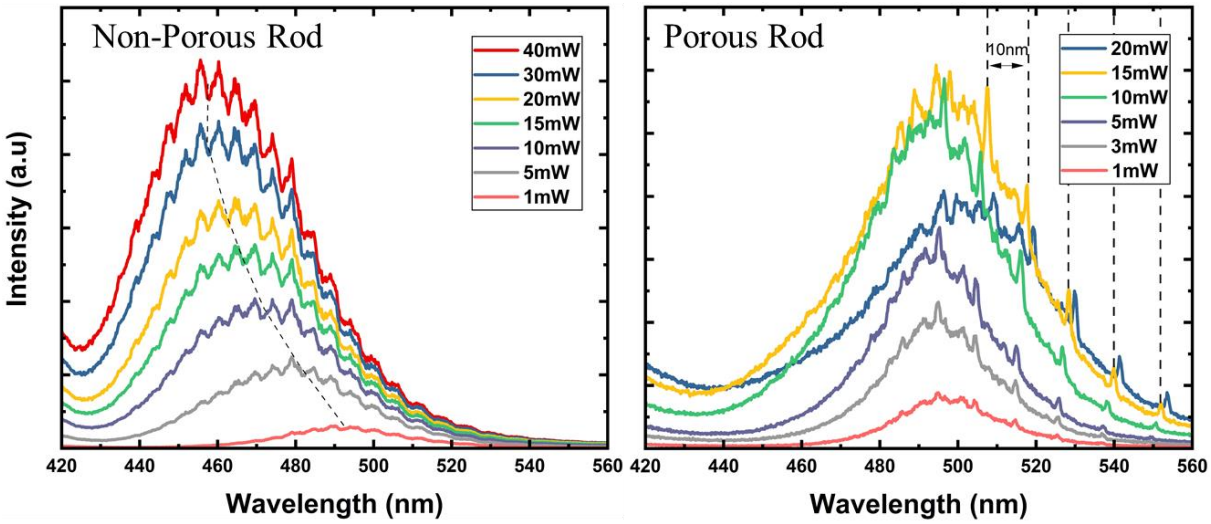

Figure 45: Micro-PL power dependent spectrum of 5 µm diameter a) Conventional Rod b) Nanoporous Rod.

A new growth run based on the same conditions but adding 100nm p-GaN took place. Electrical injected microdisk based on porous GaN have also been fabricated. In detail, a range of microdisk structures with a diameter ranging from 100 µm to 20 µm. First, EC etching took place in a 0.3M HNO3 electrolyte under 5V bias for 30 minutes. Thermal evaporation was used to deposit Ti/Al/Ti/Au as n-contact and a thin Ni/Au alloy as a p-contact. Both contacts were annealed in order to obtain a lower specific resistance. Electro-luminescence measurements have been carried out on these devices. The emission was collected by a multi-mode fibre which was placed on the edge of the device, and was detected by using a Flame UV-MIS spectrometer. Figure 46a) shows the emission image of a 40 µm diameter device under 20 mA (CW). Figure 46b) illustrates the current voltage characteristics of a porous and non-porous device, where a slightly increase of the series resistance for the porous device is observed (from 181Ω to 218Ω). Figure 46c) illustrates the SEM cross section image of a porous device. As it was expected the porosity of the cladding layer is lower than the optically simulated device, as the voltage bias was reduced. Figure 47 shows the EL spectrum as a function of the injection current for both devices. Unfortunately, no clear difference appears between them. Both samples are strongly affected by the QCSE, the blue shifting can be seen in Figure 47c). It can be observed that the sample with porous cladding is slightly less affected by QCSE, this can be due to strain relaxation obtained by the porous cladding layer. However, as the current increases to 60mA the intensity of the porous sample does no longer increase, in fact a wavelength shifting and a change in the FWHM may indicate the presence of heating issues.

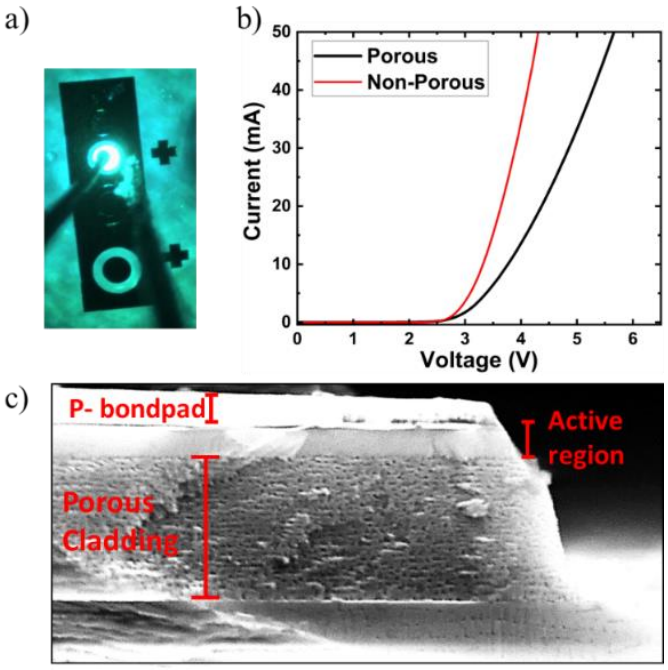

Figure 46: a) Emission image of a 40µm rod. b) Current Voltage characteristics of a 40um rod. c) Cross section SEM image from a 40 µm rod.

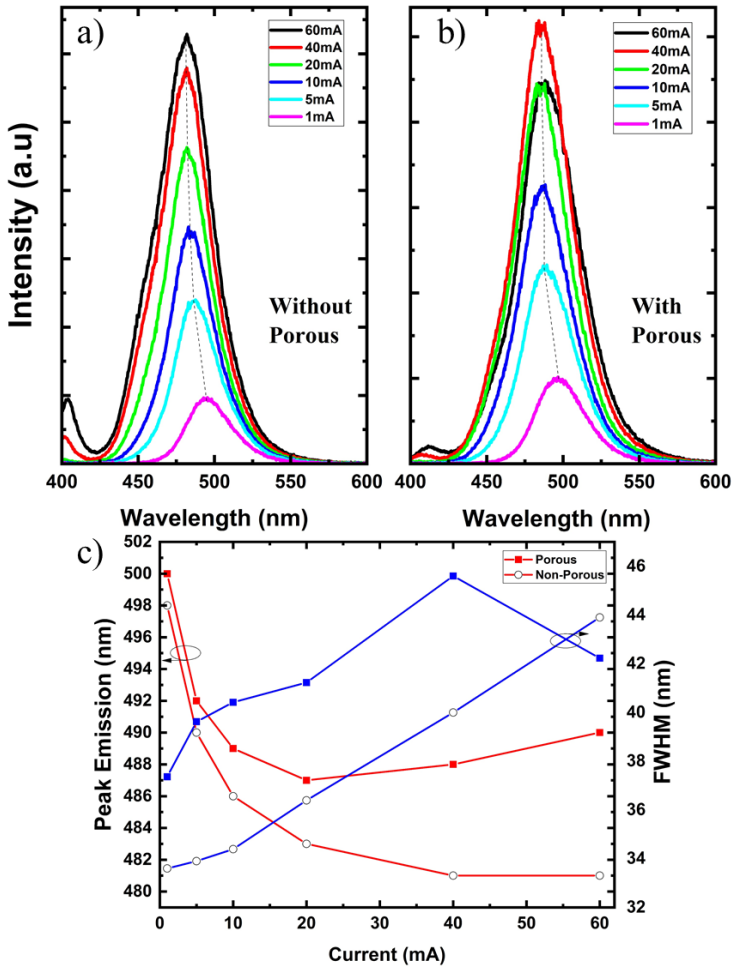

Figure 47:EL spectra of a non-porous (a) and porous (b) with 40 µm diameter rod. FWHM and emission Peak wavelength (c).

Although the porous cladding offers a good electrical injection, the refractive index difference is not as high as expected. A further increase on the bias voltage could increase the refractive index difference. However, the trade-off between high porosity and high series resistance is an inherent characteristic of porous GaN. In order to achieve lasing, 1-D photonic crystals (i.e. DBRs) could be used to generate feedback.

4.4 Simulation of InGaN/GaN active region using *SiLENSE*

SiLENSE 6.4 simulation package is a powerful software for simulating the band diagram, carrier concentration and emission wavelength of III-nitride based emitters. The computation is carried out using a 1-D drift-diffusion model, which is based on the self-consistent solution of the Poisson and fermi-Dirac equations in the heterostructure of an LED/LD [33].

A study on optimising the number of MQWs in microLEDs has been carried out. Figure 48a) provides a schematic illustration for a simulated III-nitride LEDs. The structure comprises a 500 nm GaN layer, followed by 30 pairs $In_{0.05}Ga_{0.95}N$/GaN (2.5 nm/4.5 nm) superlattice acting as a strain management layer and then $In_{0.28}Ga_{0.72}N$/GaN (2.5 nm/13 nm) MQWs as an emitting region which gives an emission wavelength of 525nm. Finally, a 20nm $Al_{0.2}Ga_{0.8}N$ electron blocking layer (EBL) and then a 150nm p-GaN form the top side of the structure.

Figure 48b) illustrates the simulated band structure of such a LED structure a under a bias of 4.5V. The present study is carried out as a function of the number of InGaN/GaN MQWs.

Figure 48c) shows the electron and hole carrier concentration for such a device with 7 MQW as an active region, exhibiting clearly that the hole concentration is dramatically reduced from the p-side to the n-side. By examining the data carefully, it has been observed that only the last quantum well which is close to the p-type layer produce emission. This is due to inefficient hole injection that limit the radiative recombination in the MQWs region [34]. In contrast, Figure 48d) illustrates the profile of the carrier concentration for a 3MQW structure, indicating the hole concentration is three orders of magnitude higher than the case with 7 MQWs.

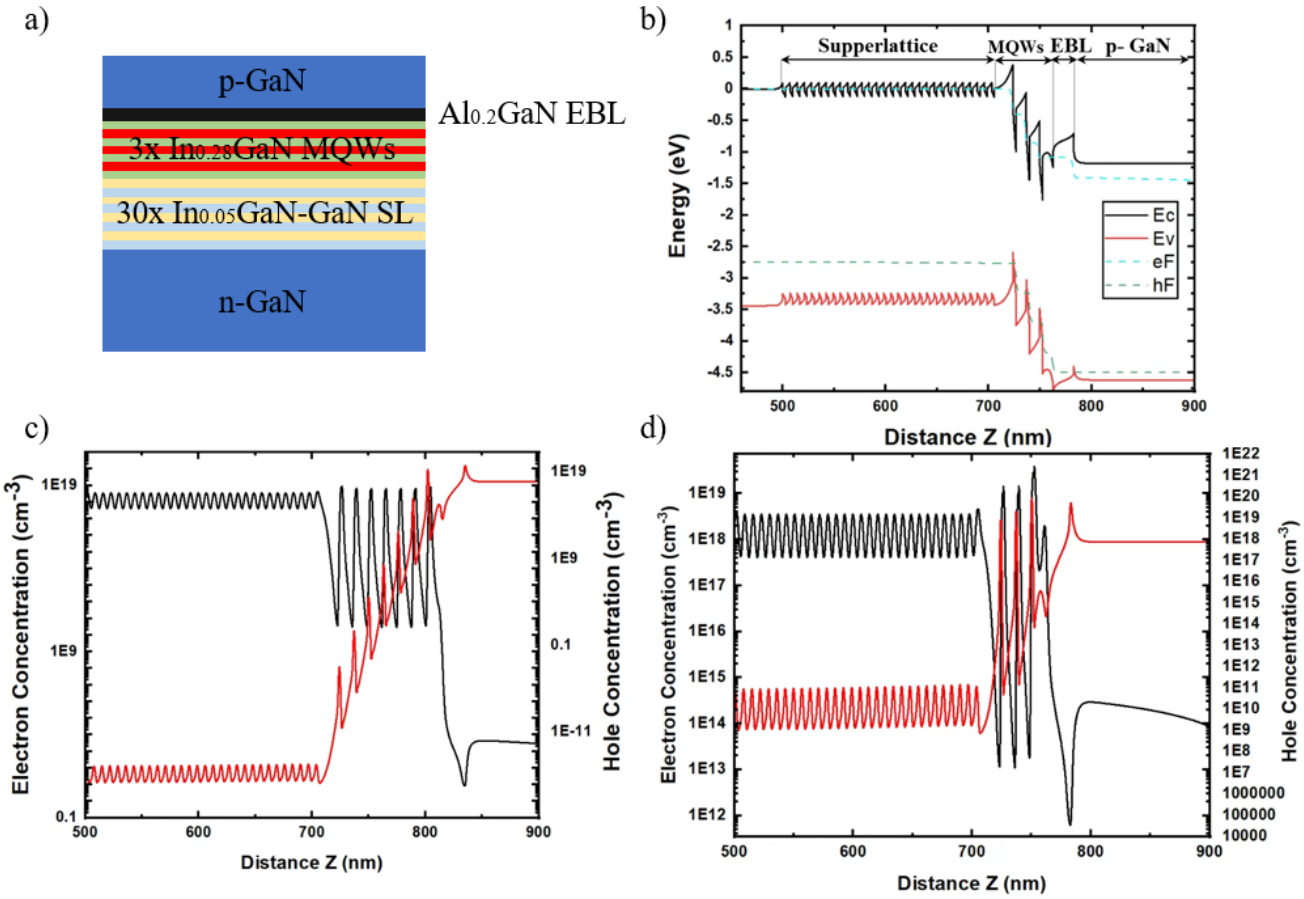

Figure 48: a) Schematic of the simulated LED structure. b) Band diagram simulated at 4.5V. c) Electron and hole distribution in a 7MQW device at 4.5V. d) Electron and hole distribution in a 3MQW device at 4.5V.

Figure 49a) shows the simulated influence of the number of MQWs on emission wavelength and emission intensity under optical and electrical pumping. In general, optical pumping measurements show the PL intensity of InGaN/GaN MQWs increases with increasing the number of InGaN/GaN MQWs assuming that there is no any extra structure. However, extra attention will have to be paid to design an electrically injected LED structure. The inset in Figure 49 (b) shows that the EL emission intensity for a LED with 7MQWs is two orders of magnitude lower than that of the LED with 3MQWs under 4.5 forward bias. This is due to the much less efficiency of hole injection as a result of the intrinsically high p-type activation energy and the intrinsically low mobility of p-type GaN in comparison to n-GaN.

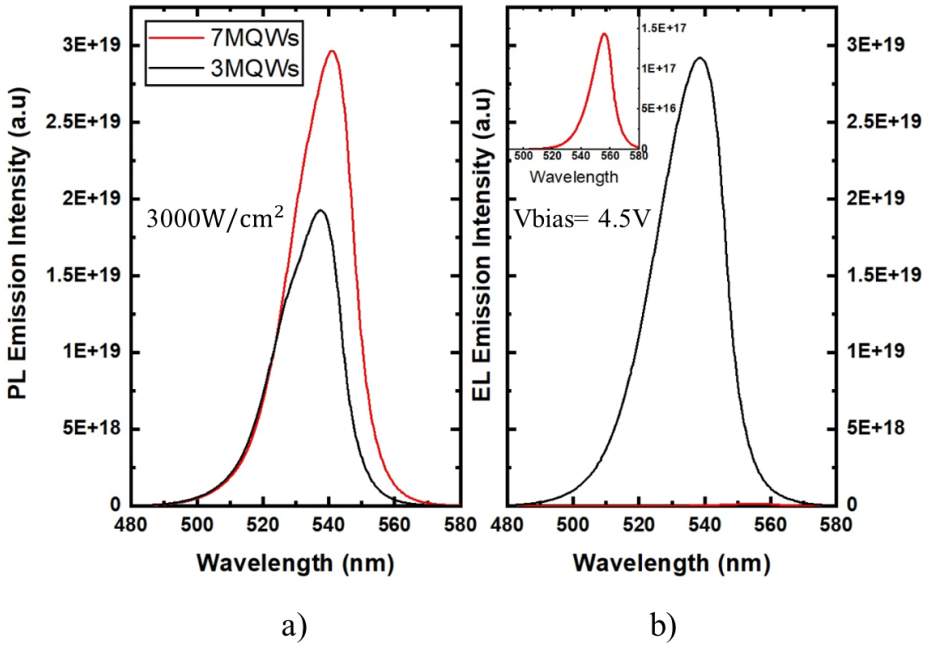

Figure 49: a) Simulated PL emission b) Simulated EL emission.

4.5 Conclusion

In summary, this chapter presents the development, advantages, limitations and potential applications of microdisk lasers. A methodical study of the thickness of the microdisk and its effects on the WGMs quality factor is conducted through FDTD simulations. Then, an alternative to the conventional pedestal approach is based on nanoporous GaN is presented. Finally, a study based on *SiLENSE* of the number of MQWs in III-nitride devices is carried out, the result showed fewer MQWs lead to a more efficient injection for lasers.

4.6 References

[1] X. Xu, et al., Wireless Whispering-Gallery-Mode Sensor for thermal Sensing and Aerial Mapping. *Light Science Applications*, 7:62, 2018.

[2] X. Jiang, et al., Whispering-Gallery Sensors. *Matter*, 3:2: 371–392, 2020.

[3] K. H. Li, Y. F. Cheung, and H. W. Choi, Whispering gallery mode lasing in optically isolated III-nitride nanorings. *Optics Letters*, 40:11:2564-2567, 2015.

[4] K. D. Heylman, K. A. Knapper & R. H. Goldsmith, Photothermal Microscopy of Nonluminescent Single Particles Enabled by Optical Microresonators. *Journal of Physics Chemical Letters*, 5:1917–1923, 2014.

[5] M. Athanasiou, et al., Monolithically multi-color lasing from an InGaN microdisk on a Si substrate. *Scientific Reports*, 7:10086, 2017.

[6] M. Feng, et al., Room-temperature electrically pumped InGaN-based microdisk laser grown on Si. *Optics Express*, 26:5043-5051, 2018.

[7] J. Wang, et al., Continuous-wave electrically injected GaN-on-Si microdisk laser diodes. *Optics Express*, 28:12201-12208, 2020.

[8] M. Yang, et al., Electrically injected GaN-based microdisk towards an efficient whispering gallery mode laser. *Optics Express*, 29:5598-5606, 2021.

[9] M.Feng, et al., Continuous-Wave Current Injected InGaN/GaN Microdisk Laser on Si(100). *ACS Photonics* XXXX:XXXX, 2022.

[10] Lumerical Inc, FDTD -3D Electromagnetic Simulator, Ansys.

[11] F. Gou, et al., Angular color shift of micro-LED displays. *Optics Express*, 27:12:A746-A757, 2019.

[12] H. Cho, et al., Enhancement of luminous intensity emission from incoherent LED light sources within the detection angle of 10° using metalenses. *Nanomaterials*, 12:153, 2022.

[13] L. Wang, et al., Issue of spatial coherence in MQW based micro-LED simulation. *Optics Express*, 29:20:31520-31526, 2021.

[14] C. Jia, et al., Length dependence of polarization in spontaneous edge emissions from InGaN/AlGaN MQWs laser diodes. *Physica Status Solidi (a)*, 204:1:257-261, 2007

[15] P. Zhao, X. Jiao and H. Zhao, Analysis of light extraction efficiency enhancement for InGaN quantum wells light-emitting diodes with microspheres. *IEEE Energytech*, Cleaveland-USA, 2012.

[16] H. Baek, et al., Selective excitation of Fabry-Perot or whispering-gallery mode-type lasing in GaN microrods. *Applied Physics Letters*, 105:201108, 2014.

[17] H. Zi, et al., Whispering-gallery mode InGaN microdisks on GaN substrates. *Optics Express*, 29:21280-21289, 2021.

[18] P.-M. Coulon, et al., GaN microwires as optical microcavities: whispering gallery modes Vs Fabry-Perot modes. *Optics Express*, 20: 18707-18716 (2012).

[19] G. Yuan, et al., Optical Engineering of modal gain in a III-Nitride laser with Nanoporous GaN. *ACS Photonics*, 3:9:1604–1610, 2016.

[20] S. Nakamura, et al., InGaN-Based Multi-Quantum-Well-Structure Laser Diodes. *Japanese Journal of Applied Physics*. 35: L74– L76, 1996.

[21] L. A. Coldren, S. W. Corzine and M. L. Mashanovitch, Diode Lasers and Photonic Integrated Circuits; John Wiley & Sons, 2012.

[22] S. Nakamura, et al., H. Room-temperature Continuous-wave Operation of InGaN Multi-quantum-well Structure Laser Diodes. *Applied Physics Letters*, 69:4056– 4058, 1996.

[23] U. T. Schwarz, et al., Optical gain, carrier-induced phase shift, and linewidth enhancement factor in InGaN quantum well lasers. *Applied Physics Letters*, 83:4095– 4097, 2003.

[24] K. Kojima, et al., Optical Gain Spectra for near UV to Aquamarine (Al,In)GaN Laser Diodes. *Optics Express*, 15:7730, 2007.

[25] T. Lermer, et al., Waveguide design of green InGaN laser diodes. *Physica Status Solidi (a)*, 207:1328– 1331, 2010.

[26] J. Piprek, Nitride Semiconductor Devices: Principles and Simulation; John Wiley & Sons, 2007.

[27] A.C. Tamboli, et al., Room-temperature continuous-wave lasing in GaN/InGaN microdisks. *Nature Photonics*, 1:61-64, 2007.

[28] S. Chang, et al., Stimulated emission and lasing in whispering-gallery modes of GaN microdisk cavities. *Applied Physics Letters*, 75:166–168 (1999).

[29] N. B. Rex, R. K. Chang, and L. J. Guido, Threshold lowering in GaN micropillar lasers by means of spatially selective optical pumping. *IEEE Photonics Technology Letters*, 13 :1–3, 2001.

[30] R. A. Mair, et al. Optical modes within III-nitride multiple quantum well microdisk cavities. *Applied Physics Letters*, 72:1530–1532 ,1998.

[31] E. D. Haberer, et al. Free-standing, optically pumped, GaN/InGaN microdisk lasers fabricated by photoelectrochemical etching. *Applied Physics Letters*, 85:5179–5181, 2004.

[32] E. D. Haberer, et al. Observation of high Q resonant modes in optically pumped GaN/InGaN microdisks fabricated using photoelectrochemical etching. *Physica Status Solidi (c)*, 2:2845 –2848, 2005.

[33] http://www.str-soft.com/products/SiLENSe/index.htm.

[34] S.Lu, et al., Designs of InGaN Micro-LED structure for improving Quantum Efficiency at low current density. *Nanoscale Research Letters*, 16:99, 2021.

Chapter 5: Enabling emission stability to microLED arrays by using microcavity effects

Intrinsic polarisation determines all the fundamental properties of III-nitride semiconductors. The intrinsic polarisation of III-nitride leads to piezoelectric fields induced by strain across the active region, which normally is InGaN/GaN quantum wells for III-nitride visible emitters. As described in Chapter 2, QCSE shifts the electron-hole wavefunction apart as the injection current increases, thus decreasing the quantum efficiency [1-4]. Phenomenally, QCSE causes a blue shift in emission wavelength. The RGB integration of microLEDs is detrimentally affected by the colour instability, specifically in microdisplays such as AR/VR, which are typically utilized at the proximity to the eye. Therefore, any tiny colour change can be sensitively identified (especially human eyes are most sensitive to green) [5].

Chapter 5, presents the effect of QCSE on microLEDs arrays. First, a theoretical reasoning is presented to achieve emission stability by means of microcavity effects. Then, a study of nanoporous based DBRs is presented. Simulations and measurements show the potential of n++GaN/GaN as a high reflectance structure. The etching conditions were optimised in order to achieve high reflectivity and a wide bandstop. Finally, an approach to epitaxially integrate green microLEDs and form a microcavity is demonstrated. Hence, the coupling between the microcavity mode and the microLED emission, lead to a negligible emission wavelength shift with increasing injection current. In contrast, identical microLEDs but without a microcavity show a large emission wavelength shift from 560 nm down to 510 nm, measured under identical conditions. This approach provides a simple solution to resolving the 30-year issue in the field of III-nitride optoelectronics.

5.1 Introduction

Since the 1990s the world of solid-state lighting (SSL) has been in constant evolution. III-nitrides have raised as the ideal candidate to produce energy efficient devices.

The next generation of displays require high density pixels in order to achieve high resolution. Liquid Crystal Displays (LCD) are considered to be the mainstream technology that has been dominating the display's field for the last two decades. However, the need for a back lighting, slow response, low efficiency and low colour saturation lead into the need of a technological change. In 1997, Organic Light Emitting Diodes (OLED) emerged as the candidate to replace

LCDs due to their pixel self-emissivity, wide viewing angle, high-contrast, and faster response. MicroLEDs are called to become the next key-game changer component of this new generation displays. In theory, microemitters can provide higher brightness, improved contrast ratio, higher resolution and response time, longer lifetime and wider viewing angles than LCD and OLED. Therefore, MicroLEDs could potentially be used in a wide range of applications, ranging from wearable devices [6], Visible Light Communications (VLC) [7], high resolution big area displays and micro displays for virtual reality (VR) or augmented reality (AR) [8]. Table 4 list the comparison of MicroLED, OLED and LCD.

Table 4: Comparison between microLED, OLED and LCD technology. Adapted with permission from [9]

Item	MicroLED	OLED	LCD
Mechanism	Self-emissive	Self-emissive	Backlighting and colour filter
Luminance	Max $>10^5$nits (full colour)	Max $<5x10^3$ nits (full colour)	Max. 7 $x10^3$ nits (full colour)
Contrast ratio	>100000:1	>10000:1	5000:1
PPI	Max. 30000 PPI	Max. 1433 PPI	Max. 806 PPI
Pixel size	Min. submicron	Min. 18µm	Min. 32 µm
Compactness	High	Medium	Low
Lifetime	>100000	10000	30000-60000
Operation temperature	-100° C - 120° C	-50° C - 70° C	-20° C - 80°C
View angle	Max. 180°	Max. 89°	Max. 89°
Response time	ns	µs	ms
Power consumption	Low (in theory)	Medium	Medium
EQE	10%-30% (~80% in theory)	10% - 40%	5% - 12%
Cost	High	Low	Low

Despite all the advantages and potential applications, many challenges still involving microLEDs. Some argue that the biggest challenges are mass transfer, manufacturing of thin-film transistors (TFT) substrates to drive the circuit, and the full colour RGB implementation [10]. Others consider that the main issue is the efficiency, due to the low p-type conductivity related to the intrinsic properties of GaN [11]. The standard fabrication of III-nitride microLEDs rely on standard photolithography and dry etching processes. In order to minimize costs, the pixel size must be decreased <5-10 µm. However, as the pixel size is shrunken the External Quantum Efficiency (EQE) is reduced. Due to their small footprint, microLEDs are impacted by severe sidewall effects related to the formation of defects during the dry etching processes, which act as a non-radiative recombination centres, leading to a reduction on the optical performance [11]. Sidewall passivation with dielectric materials have been applied to reduce the

damage after dry etching, but the improvement is marginal even when advanced techniques such as atomic layer deposition (ALD) is used [12].

There is an absence of reports for microLEDs <5 μm. The reported EQE was limited to 1-5%, meaning that those microLEDs could not offer better efficiency than OLEDs. To overcome the mentioned challenge, another epitaxial approach was presented in 2019 by our group. In that work, the authors presented a novel selective overgrowth method to create sidewall damage free microLEDs. Our method relies on formation of micro-hole pattern on a dielectric material deposited on a previously GaN grown wafer (termed template). Then, the template is placed into the MOVPE, where the microLEDs grow inside the hole. The dimension, the pixel location, the interpitch and the shape are fully controlled. Thus, microLEDs with 3.6 μm diameter and 2 μm interpitch achieved 9% EQE at 500 nm [13].

As described in Chapter 2, one of the main challenges of III-nitrides is their intrinsic polarisation which leads to piezoelectric fields induced by the strain on the InGaN/GaN MQWs. The most noticeable effect of QCSE is the emission wavelength shift caused under increasing current. Figure 50 illustrates the blue shifting on microLEDs arrays, exhibiting that it emits yellow at 2mA, but green when the injection current rises to 5mA.

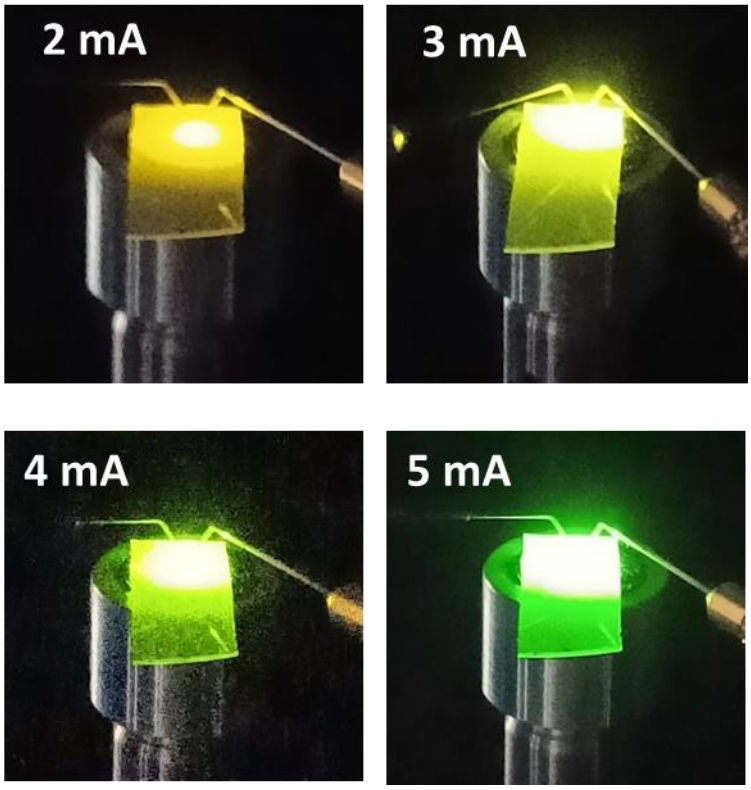

Figure 50: Blue shifting on InGaN microLED under increasing current, demonstrating a clear colour change. Reproduced with permission from ACS Photonics 2022, 9, 6, 2073–2078.

5.2 Experimental

5.2.1 Enabling mode stability with microcavity effects

As introduced in Chapter 2, microcavities are optical resonators close to or below the dimension of the wavelength of light, normally formed when a spacer layer is placed between two reflectors. The mode wavelength of a FP cavity is determined by both the cavity length and the refractive index, given by:

$$2nL = m\lambda \tag{31}$$

Where L is the cavity length, m is the order of modes in the cavity and n is the refractive index [14]. From equation 31, we can see that the mode wavelength will be determined by the refractive index for a fixed cavity length. However, it is well known that in most cases, the refractive index decreases linearly as a function of the free carrier density, expressed by:

$$n = n_o - \left(\frac{2\pi n_e q^2}{n_o m^* \omega^2}\right) \tag{32}$$

Where n_o is the refractive index when the free carrier density is zero, m^* and ω are the effective mass of carriers and the frequency of emission, respectively, n_e is the free carrier density, and q is the electron charge [15]. Considering an InGaN based device emitting at 520 nm, $m^*=0.2m_o$ (m_o is free electron mass) and $n_o=2.5$, Equation 32 can be redefined to:

$$\Delta n = n - n_o = -5.3 \times 10^{-22} n_e \tag{33}$$

Figure 51 illustrates the effect of the carrier density in the mode wavelength, where the cavity length is assumed to be 850nm, n_o=2.44 and m=8. As can be seen, the impact of the injection carrier is ideally negligible, the shifting could be around 1nm when the carrier density reaches the transparency density for reported pulsed LDs ~10^{19}/cm^3 [16,17].

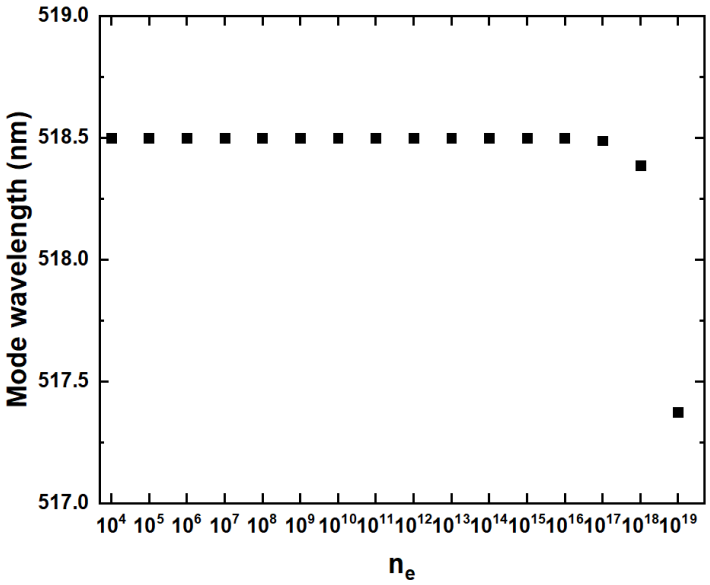

Figure 51:Calculated mode wavelength shifting due to free carrier density. Calculation based on Eq.32, assuming L=850nm, n_o=2.44 and m=8.

Theoretically, the mode resonance wavelength of the cavity would not be affected under high injection current conditions. Therefore, if the coupling between an LED emission and a cavity mode is possible, the shifting on the emission wavelength produced by QCSE would be reduced.

5.2.2 Nanoporous GaN based Distributed Bragg Reflectors

Chapter 2 described the potential of porous GaN to form lattice-matched Distributed Bragg Reflectors (DBRs).

3D-FDTD simulations were used to estimate the number of pairs needed to form a high reflectance DBR. Thus, a stack of materials with different refractive index was formed. The refractive index used for the u-GaN (before porous) was extracted from [18]. The nanoporous layer (after etching) refractive index was taken from [18], where VAT is used to estimate the effective refractive index for a known porosity (see Chapter 2). The thickness of each layer was $\frac{\lambda}{4}$ in order to maximise the Bragg reflection. An incident plane wave source with a centre wavelength of 550nm and 300nm span injected the electric field from above the surface of the DBR. Frequency monitors were used to record the reflected field from the stack. The simulation run for 5000fs, periodic boundary conditions were assumed in the X-Y direction and perfect matched layers (PML) on the Z axis.

Figure 52a) shows that a stack of 11 pairs could produce a high reflectance (99%) with a 100nm FWHM band. Figure 52b) illustrates the change of FWHM due to the refractive index of the porous layer. Thus, a high reflectance DBR with a centre wavelength of 520nm and 120nm FWHM was expected.

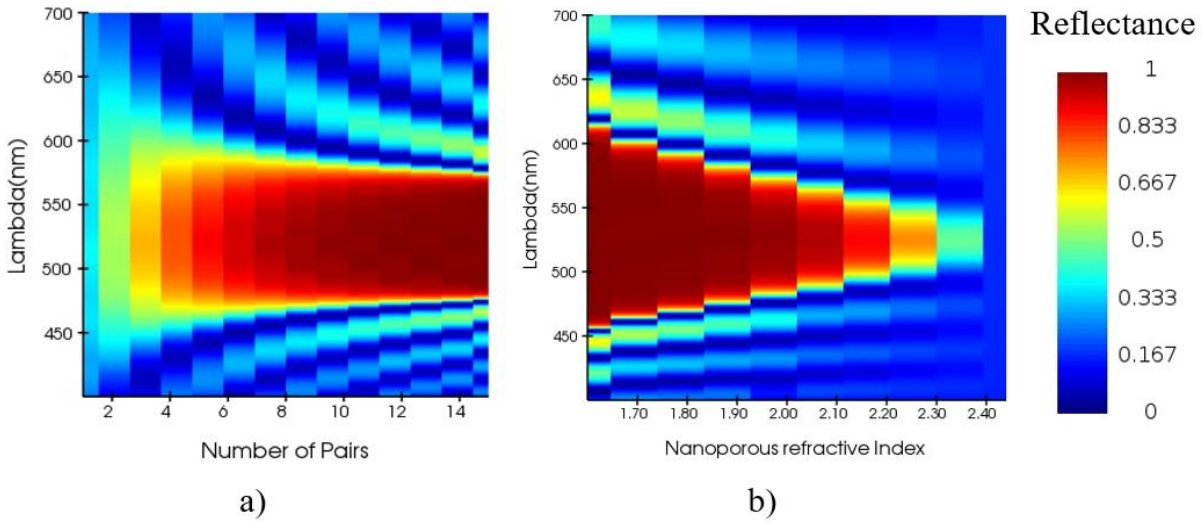

Figure 52:Peak reflectance and number of pairs (a), effect of the porous refractive index on the DBR FWHM.

Once the number of pairs was decided, an epi wafer was grown on c-plane sapphire by means of MOVPE (Aixtron 3×2" flip-top CCS reactor). The thickness of each layer was controlled using real time monitoring. The doping of the n++GaN was tuned with Si_2H_6 flow rate, which acts as a precursor for Si doping. The doping was reported to be ~ 5×10^{19} cm^{-3} [19].

The epiwafer was cleaved to form a rectangular shape of 2 cm x 4 cm. An indium contact was placed at the edge of the sample to form the anode path. After that, the sample was immersed into the electrolyte (0.3M-HNO_3), as described in Chapter 2. The sample was etched for 30min at a constant voltage bias of 6V. As described in previously, the porosification process is conductive-selective, only the n++ layers will be etched, forming nanoporous GaN. During the EC process, the acid flows through dislocations, forming vertical etching pathways where each layer is etched sequentially from top to bottom, forming subsurface pores. Figure 53, shows the microscope view of a DBR sample etched under different voltages. Under low voltage conditions (bias <5V), no porous formation was observed, as the energy bands are not bend enough to allow tunnelling from holes. As the voltage is increased, the band-bending produces holes to penetrate from the electrolyte-semiconductor interface. Figure 53a) illustrates the porous path formation through defects and pits, where the green dots correspond to the top layers being porosified. Furthermore, it is possible to observe that uniform porosification occurs at the edge of the sample. Figure 53b) shows that as the voltage is further increased to 6V, the porous layer starts to merge. However, as the voltage increased to 7V, surface cracks appeared at some specific points (Figure 53c)), a further increase to 8V causes the lift-off of the top layer, as can be seen in Figure 53d).

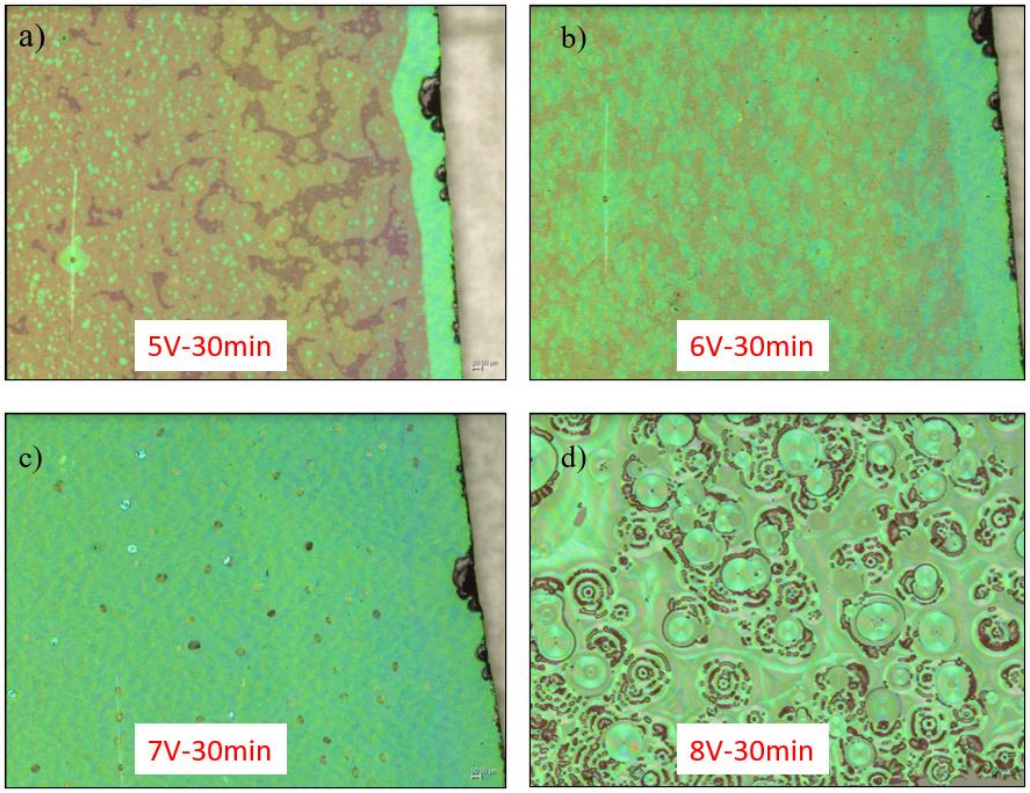

Figure 53: Samples etched in 0.3M HNO_3 electrolyte during 30 minutes under different bias.

The inherent trade-off exist between bias and sample cracking plays an important role in nanopores formation. Therefore, the voltage was reduced to and the etching time increased. Figure 54 shows the cross-section view of a porous DBR etched with 6V during 1 hour. The thickness of the NP layer and u-GaN layer are 90nm and 40nm respectively.

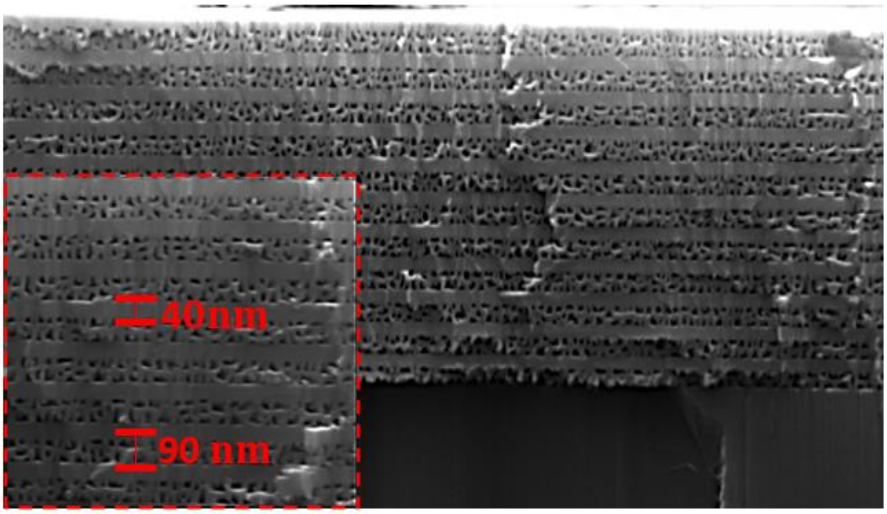

Figure 54: Cross section image of a porous DBR etched with 6V bias during one hour. Inset shows the thickness of the NP-GaN/u-GaN layers.

Reflectance measurements of DBRs were carried out using the micro-EL setup described in Chapter 3. An unpolarised light lamp that covers a wide spectral range (UV-IR) was used as a source. An aluminium reflectance standard (STAN-SSH) was used to know the peak reflectance. Figure 55, shows the measured and simulated reflectance of the DBR, where a good agreement between them can be observed. The DBR exhibits a central wavelength at 520, with a high reflectivity ~99% and a broad stop band of 122nm.

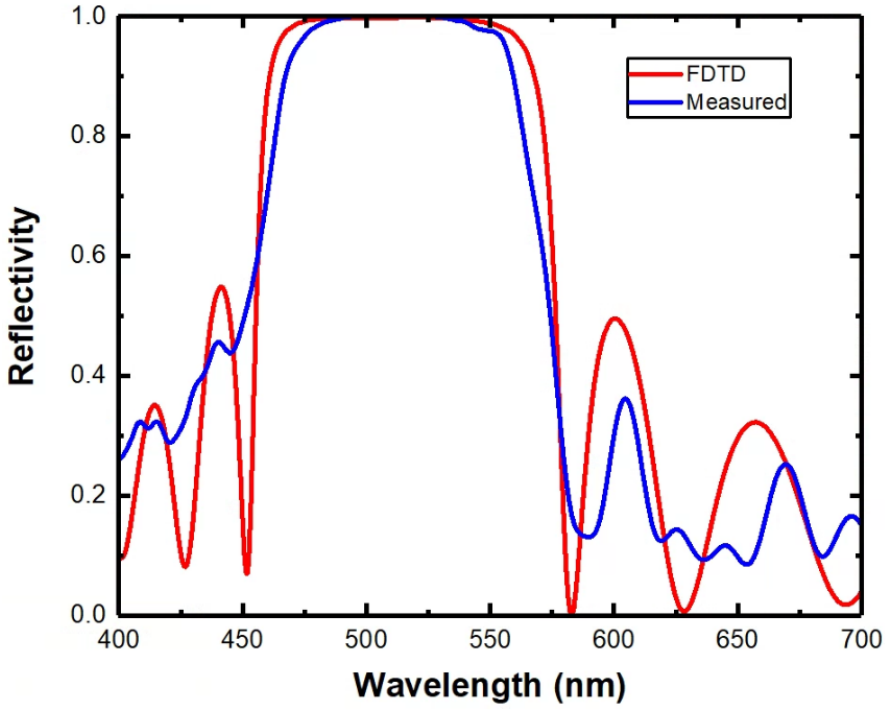

Figure 55: Measured and simulated (FDTD) reflectance of a porous DBR.

Once the DBR growth and etching conditions were totally optimised to provide high reflectance at the desired wavelength, microLEDs were formed by means of the selective overgrowth method described in the previous section. In order to achieve coupling, the emission of the MQWs must spectrally overlap the centre wavelength of the DBR. The LED structure is standard, starting with a thin n-type GaN layer and then an $In_{0.05}GaN_{0.95}$/GaN superlattice structure, followed by 5 periods of green $In_{0.27}GaN_{0.73}$/GaN MQWs (InGaN quantum well: 2.5 nm and GaN barrier: 13.5 nm) as an emitting region, then a 20 nm p-type $Al_{0.2}Ga_{0.8}N$ electron blocking layer and a final 200 nm p-type GaN. The total thickness of the overgrown layers is ~550 nm, which is levelled with the SiO_2 masks. A 300 nm n-GaN layer was grown between the DBR and the microemitter to allow n-contact formation. Figure 56a) represents the final growth structure. Photoluminesce measurements were carried out around the 2-inch wafer by means of the standard PL setup described in Chapter 3. Figure 56b) illustrates the PL at different wafer locations, the shifting in wavelength is attributed to be a

consequence of temperature instability during the growth, the different peaks correspond to interference fringes produced due to GaN-Air interface. The centre emission wavelength is around 525 nm, with a FWHM of 45 nm, which overlaps with the measured reflectance of the porous DBR. Therefore, coupling between the MQW emission and an optical mode could be allowed.

The samples were EC etched in a 0.3M HNO3 electrolyte at a constant 6V bias voltage. Figure 56c) illustrates a cross-section view SEM image of the nanoporous microcavity, where the thickness of the total microcavity is 850 nm. The inset illustrates the top view SEM image of the high density microLED array.

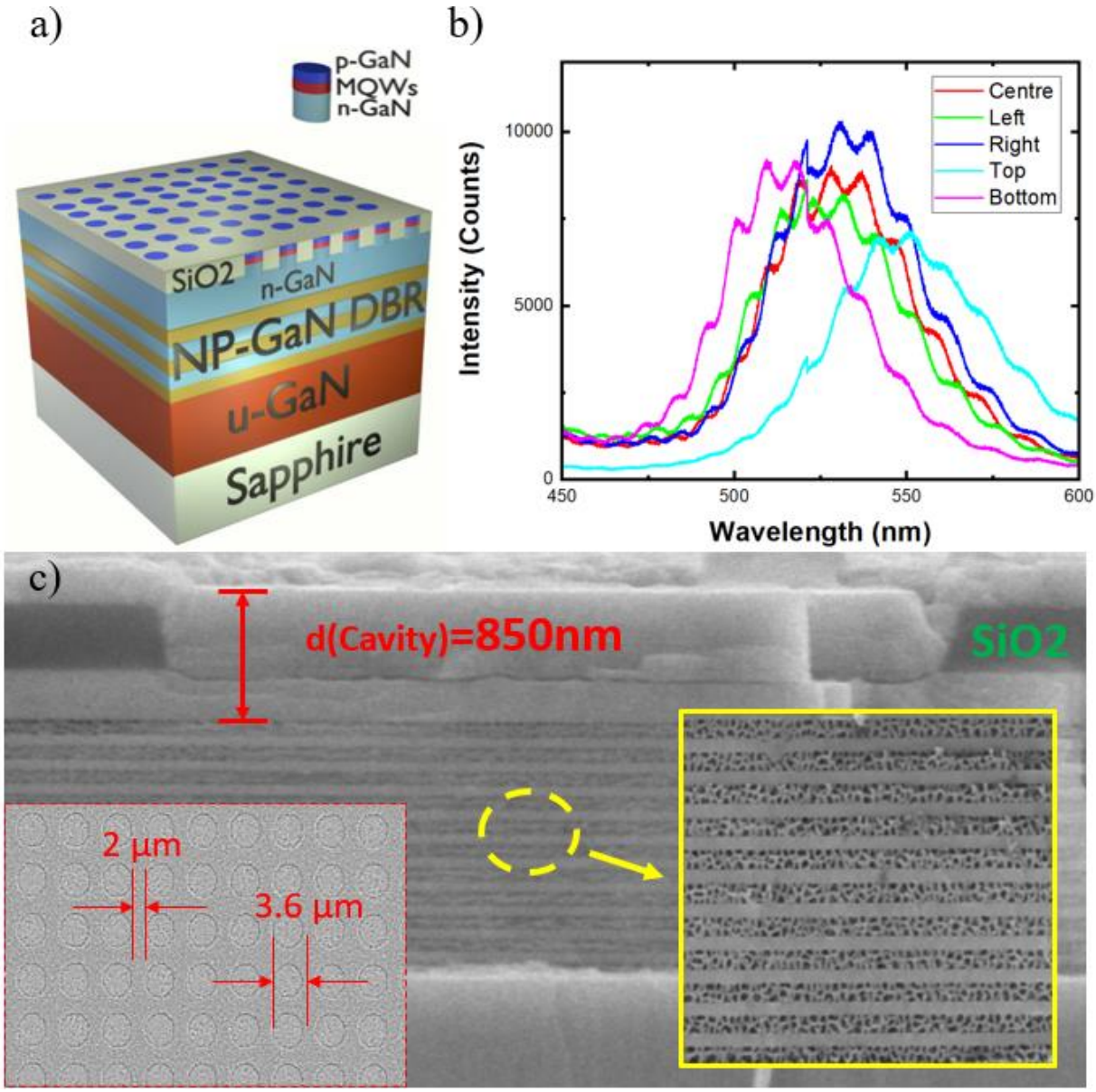

Figure 56:a) Representation of the overgrowth emitters. b) Photoluminescence of the grown micro-emitters. c) Cross section SEM image of the µLED with porous DBR, inset shows the top view of the array. Reprinted with permission from ACS Photonics 2022, 9, 6, 2073–2078. Copyright 2022 American Chemical Society.

Standard device fabrication has been performed on both the microLED sample with the EC etching process (meaning with DBR) and the microLED sample without the EC etching (meaning without DBR) in the same batch. First a p-activation in a N_2 ambient at 650°C for 15 minutes took place. Then, 330x330 µm and 150x150 µm mesas were etched through the microLED template by ICP. A Ti/Al/Ti/Au alloy was used as a n-contact, after deposition, the sample was annealed in a N_2 ambient for 1 minute at 700°C. ITO (Indium Thin Oxide) was chosen as a p-contact due to its high transparency. A room temperature deposition of 100 nm took place in our Electron-beam. Finally, bondpads were deposited on top of the current spreading layer to facilitate the electrical testing.

5.3 Results and discussion

5.3.1 Electrical and optical characteristics

The ITO annealing conditions were studied to enhance the I-V characteristics. E-beam was used to deposit 100nm thick ITO at room temperature on sapphire substrate. Rapid Thermal Annealing (RTA) was used in a mixed air configuration (N_2-O_2) with different annealing profiles and temperatures. 4-point probe measurements were carried out to decide which approach provides a lower resistance. Table 5 summarises the Hall-effect results. Sample E, provides the lower sheet resistance, which almost one order of magnitude smaller than the sample without annealing. Therefore, the conditions of sample E were used.

Table 5 : ITO annealing conditions and 4-point probe measurements

Sample	Thickness (nm)	Post-Annealing	200°C intermediate step (30s)	Temperature (°C)	Time (s)	Sheet Resistance (Ω/sq)
A	100	No	No	No	-	1742.6
B	100	Yes	Yes	600	60	110.1
C	100	Yes	No	600	60	162.34
D	100	Yes	Yes	500	60	280.5
E	200	Yes	Yes	600	60	100.2
F	200	Yes	Yes	600	120	102.6
G	200	Yes	Yes	550	60	129.5

After the devices were fabricated, electrical testing was performed on bare chips, without any heat sink, no other additional processes were used to enhance the extraction efficiency. The emission spectra were recorded using the µEL setup described in Chapter 3. All the measurements were taken at room temperature under the same conditions.

Figure 57, illustrates the emission spectra under different injection currents of the sample with and without DBR, the red dashed line represents the emission shifting. It is possible to observe that for the microcavity based device the emission wavelength has a stable main peak at around 525nm. In remarkable contrast, the sample without DBR, starts to emit yellow light under low current injection. After that, it shows a clear blue shifting due to the QCSE. As explained in Chapter 2, the piezoelectric field in the InGaN/GaN MQWs grown on c-plane tilt the band structure, causing a first a red shift on the emission wavelength. However, under injection current the carrier gather at the heterostructure interface screening the electric field, which leads to a blue shifted emission.

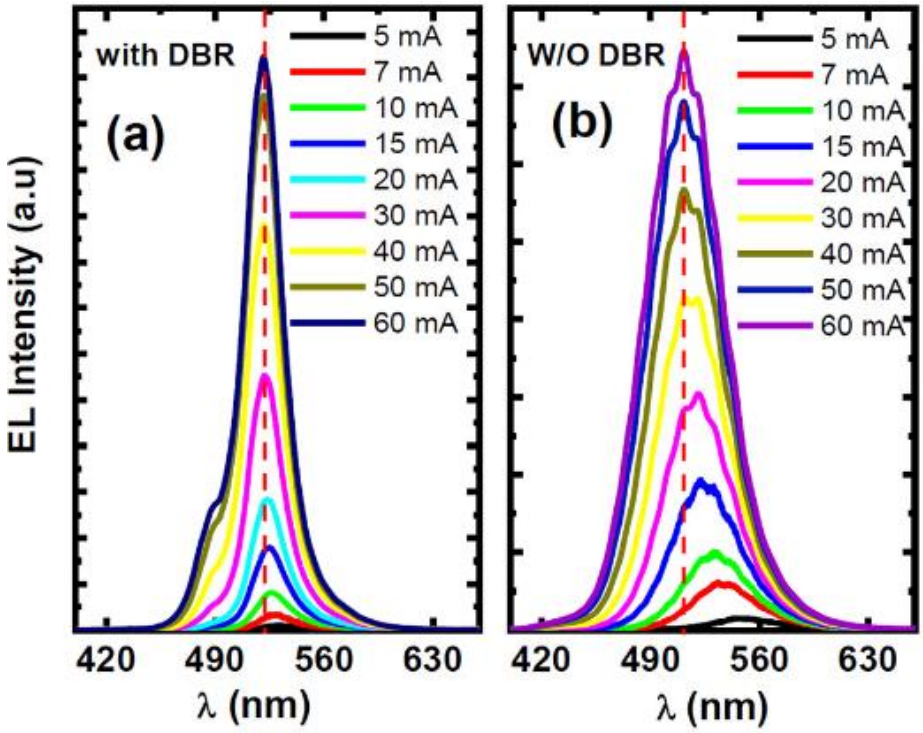

Figure 57: Emission spectra of the device with porous DBR (a) and without DBR (b). Reprinted with permission from ACS Photonics 2022, 9, 6, 2073–2078. Copyright 2022 American Chemical Society.

Figure 57a), illustrates that at 40mA the microcavity based device has a little shoulder at around 480 nm, which is believed to be a second mode, giving a potential FSR of 45 nm. In fact, this has been demonstrated later in this chapter. The mode-competition does not affect the dominance of the main mode at 525nm. The FWHM and peak wavelength as a function of injected current is illustrated in Figure 57. The spectral linewidth is reduced by almost by a factor of two due to microcavity effects.

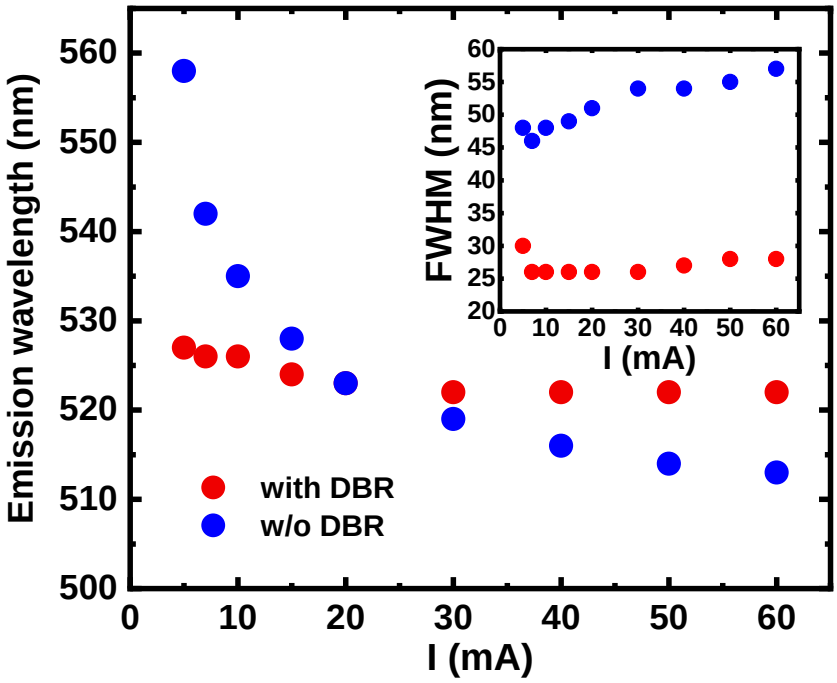

Figure 58: Emission wavelength shifhting due to QCSE in standard (blue) and microcavity based device (red). Inset illustres the FWHM reduction.

It can be observed that the sample without DBR suffers a peak shifting of 50nm between 5mA to 60mA. Nevertheless, the microcavity based device shifts only 3nm. In section 5.2.1 we assumed that the mode wavelength should not affected by the injected carriers. The slight mode shifting can be described because of the bias current as follows: the chip temperature rising modifies the effective refractive index of the cavity, altering the effective cavity length and thus the cavity resonance wavelength [19].

Figure 59, exemplifies how the consequence of the QCSE has been partially mitigated for the microcavity based device, allowing colour emission stability under increasing current injection. While the standard microLED evolves initially from yellow at 5 mA, through yellow/greenish at 10 mA, then pure green at 20 mA, and finally to green/blueish at 60 mA. Therefore, the microcavity device partially mitigates the widely studied issue of blue shifting on III-nitrides.

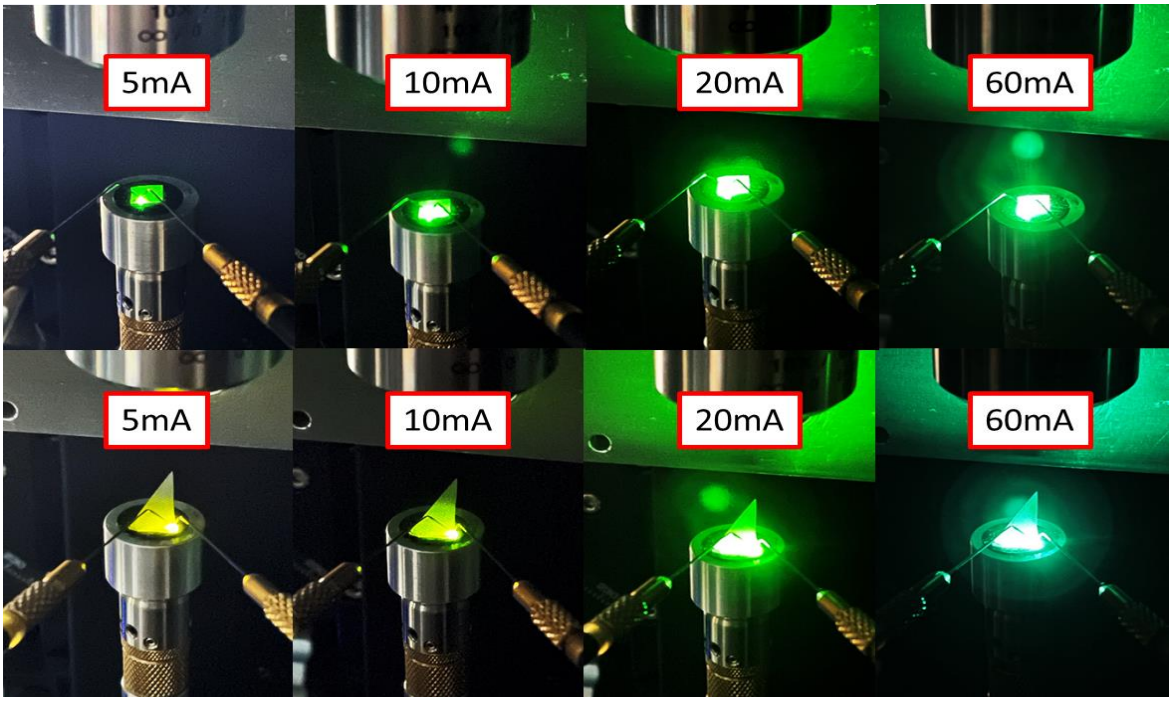

Figure 59: Emission image of the device with (top) and without DBR (bottom). Reprinted with permission from ACS Photonics 2022, 9, 6, 2073–2078. Copyright 2022 American Chemical Society.

It is important to clarify, that although there is no top DBR, the Air-GaN interference acts a reflector which has a 20% reflectance, leading to a microcavity formation [20-21]. In order to verify the existence of modes, 3-D FDTD simulations have been performed. The geometrical data of our devices were taken from the cross-section view image shown in Figure 56c). In a similar way as described previously, a plane-wave was used as an excitation source. However, in this case, time-monitors were added through the microcavity region to record the decay slope in the electric field, which is used to determine the wavelength of the resonant modes. Figure 60a), illustrates the simulated cavity modes, where a dominant mode appears at 526 nm and second mode is at 480 nm. As stated in Section 5.2.1, the cavity mode is not greatly affected by the refractive index change due to free carriers, this fact is demonstrated in Figure 60b). The free spectral range of the measured spectrum is 46 nm, which in principle does not match with a physical cavity thickness of 850 nm. However, as it is explained in Chapter 2, the effective cavity length is affected by the penetration depth of the field into the DBR structure. Figure 60c) illustrates the effective cavity length and the electric field for two different wavelengths (in/out) resonance.

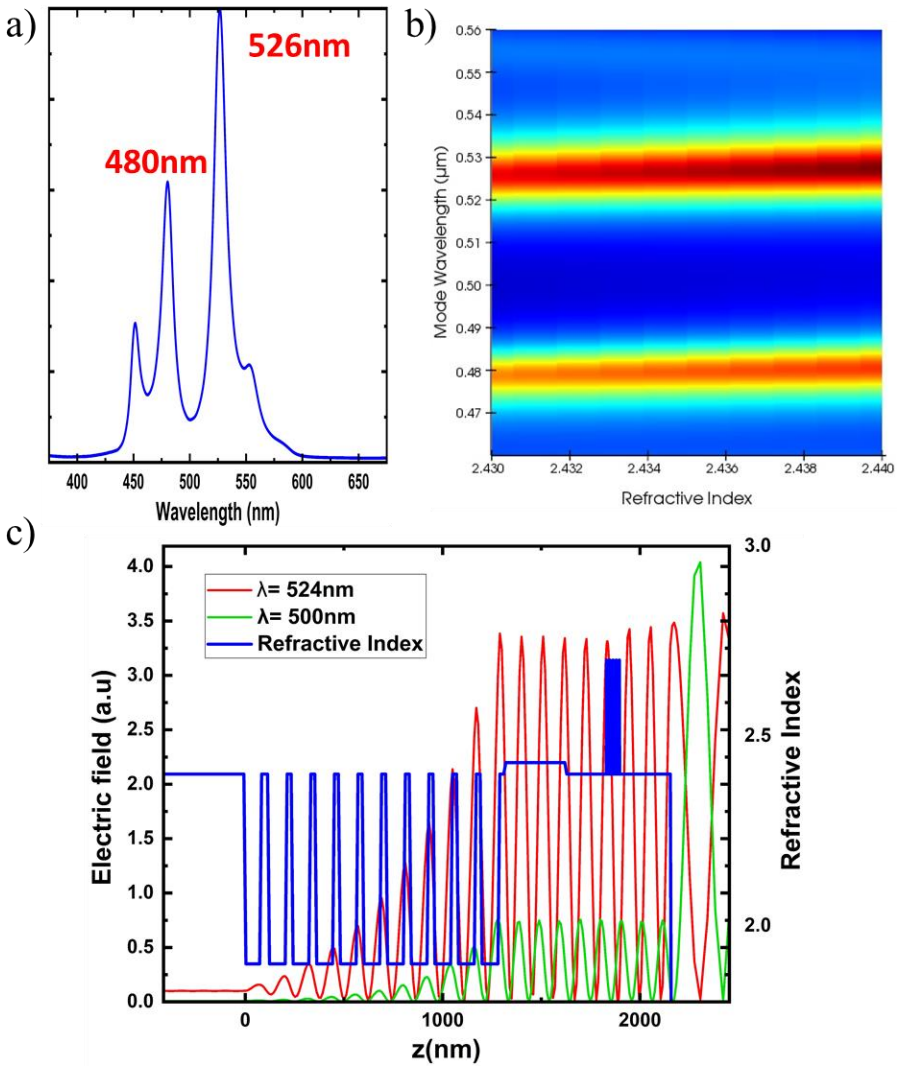

Figure 60: a) Simulated Cavity modes. b) Simulated mode wavelength for different cavity refractive indices. c) Simulated Electric field (E_z) in the cavity at the mode wavelength (red) and out of resonance (green).

Unfortunately, the formation of the porous DBR lead into a higher device resistance, therefore the IV characteristics are poor while compared to the un-etched device, as shown in Figure 61a). This can be explained due to parasitic etching of the n-GaN placed above the DBR occurring during the porous formation. Parasitic etching during the EC process is a matter of concern by different authors [22-23]. Figure 61b), illustrates how the damage can also affect the superlattice layers of the microLEDs, which definitely will have detrimental effects on its performance. Next chapter will discuss etching optimisation to improve the unintentional etching.

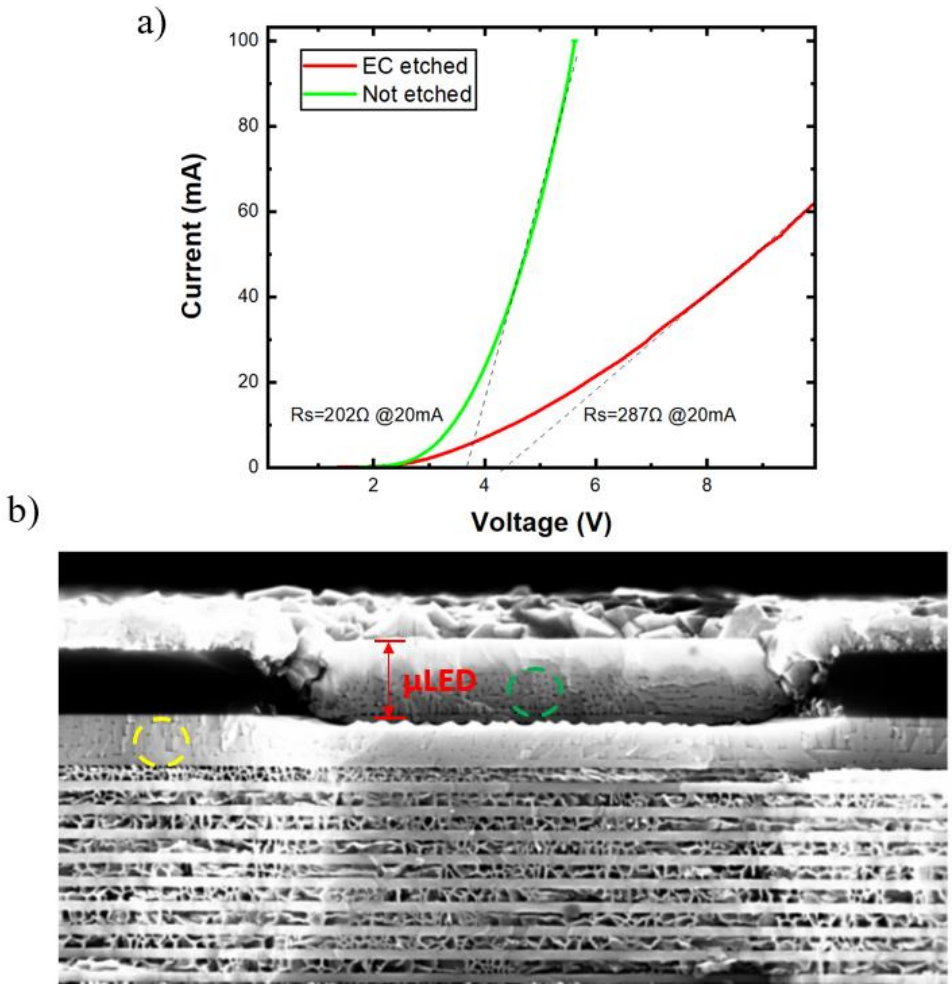

Figure 61: a) I-V characteristic of a 150x150µm device with (red) and without DBR (green) using ITO as a P-contact. b) Cross section SEM image showing the parasitic etching on the microemitter (green) and n-GaN (yellow).

5.4 Conclusion

In summary, this chapter presents the design, fabrication and performance characterisation of microcavity based III-nitride microLEDs. By means of selective overgrowth on a patterned substrate, sidewall defect-free microLEDs with 3.6 µm diameter were formed. An array of few thousands microemitters were driven under difference injection current conditions. The peak emission wavelength of the unetched devices shows a shifting of almost 50 nm from 5 mA to 60mA. While the microcavity based device only shifts 3nm under the same current conditions, due to the coupling of the emission LED and an optical mode. The proposed microcavity effect, partially mitigates the QCSE. Furthermore, the spectral linewidth is reduced from 50nm to 25nm. Thus, this approach could clearly benefit the fabrication of full colour micro displays.

5.5 References

[1] T. Takeuchi, et al., Quantum-Confined Stark Effect due to piezoelectric fields in GaInN strained quantum Wells. *Japanese Applied Physics*, 36:L382, 1997.

[2] F. Bernardini, V. Fiorentini and D.Vanderbilt, Spontaneous polarization and piezoelectric constants of III-V nitrides. *Physical Reviews B*, 56: R10024, 1997.

[3] C. Wetzel, et al., Electric-field strength, polarization dipole, and multiinterface band offset in piezoelectric Ga1–xInxN/GaN quantum-well structures. *Physical Reviews B*, 61:2159– 2163, 2000.

[4] A. Khan, K. Balakrishnan and T. Katona, Ultraviolet light-emitting diodes based on group three nitrides. *Nature Photonics*, 2: 77– 84, 2008.

[5] W. Meng, et al., Three-dimensional monolithic micro-LED display driven by atomically thin transistor matrix. *Nature Nanotechnology*, 16:1231– 1236, 2021.

[6] Z. Liu, et al., GaN-based LED micro-displays for wearable applications. *Microelectronics Engineering*, 148:98–103, 2015.

[7] L.Yu, et al., High-speed micro-LEDs for visible light communication: challenges and progresses. *Semiconductor Science and Technology*, 37:2:023001, 2021.

[8] F. Templier, High-resolution GaN microdisplays and solution for full-color devices for AR/MR applications. International Conference on Display Technology (ICDT), 52:S1, 2021.

[9] Z.chen, S. Yan and C. Danesh, MicroLED technologies and applications: characteristics, fabrication, progress, and challenges. *Journal of Physics D: Applied Physics*. 54:123001, 2021

[10] C.-H. Lin, et al., Invited Paper: Quantum dots based full-color display on micro-light-emitting-diode technology. SID Symposium Digest of Technical Papers, 49:S1:267–70, 2018.

[11] J. Y. Lin and H. X. Jiang, Development of microLED. *Applied Physics Letters*, 116:100502, 2020.

[12] Yu, J., et al., Investigations of sidewall passivation technology on the optical performance for smaller size GaN-based Micro-LEDs. *Crystals*, 11:403, 2021.

[13] M. S. Wong, et al., High efficiency of III-nitride micro-light emitting diodes by sidewall passivation using atomic layer deposition. *Optics Express*, 26:21324, 2018.

[13] J. Bai, et al., A direct epitaxial approach to achieving ultrasmall and ultrabright InGaN micro light-emitting diodes (μLEDs). *ACS Nano*, 14: 6: 6906–6911, 2020.

[14] H. Kogelnik and T. Li, Laser Beams and Resonators. Applied Optics, 5:1550– 1567, 1966.

[15] H. X. Jiang and J. Y. Lin, Mode spacing "anomaly" in InGaN blue lasers. *Applied Physics Letters*, 74:1066, 1999.

[16] W. W. Chow, A. F. Wright, and J. S. Nelson, Theoretical study of room temperature optical gain in GaN strained quantum wells. *Applied Physics Letters*, 68:3:296 -298, 1996.

[17] M. Suzuki and T. Uenoyama, Optical gain and crystal symmetry in III–V nitride lasers. *Japanese Applied Physics Letters*, 69:22:3378, 1996.

[18] G. yuan, et al., Optical engineering of modal gain in a III-Nitride laser with Nanoporous GaN. *ACS Photonics*, 3:9:1604-1610, 2016.

[19] Y. Tian, et al., Nearly lattice matched GaN distributed bragg reflectors with enhanced performance. *Materials*, 15(10):3536, 2022.

[20] J.Wu, W.Xiao, Y-M.Lu, Temperature and wavelength dependence of gain and threshold current detuning with cavity resonance in vertical-cavity surface-emitting lasers. *IET Optoelectronics*, 1:5:206-210, 2007.

[21] C. Hums, et al., Fabry-Perot effects in InGaN / GaN heterostructures on Si-substrate. *Journal of Applied Physics*, 101:033113, 2007.

[22] D. Zhu, et al., Efficiency measurement of GaN-based quantum well and light-emitting diode structures grown on silicon substrates. *Journal of Physics*, 109:1, 2011

[23] X. Lu, et al., Performance-Enhanced 365 nm UV LEDs with electrochemically etched nanoporous AlGaN Distributed Bragg Reflectors. *Nanomaterials*, 9:6:862, 2019.

[24] P.H. Griffin and R.A. Oliver, Porous nitride semiconductors reviewed. *Journal of Physics D: Applied Physics*, 53:38, 2020.

Chapter 6: Towards micro-Vertical Surface Emitting Lasers (VCSELs) based on III-nitride selective overgrowth

GaAs or InP based VCSELs have been well developed in the last two decades and have been widely commercialised. However, the development of III-nitride VCSELs is still in an infant stage due to a number of technological challenges. The necessity of top and bottom DBRs with approaching a reflectance of 100% presents a major challenge due to the growth of III-nitride on a large lattice-mismatched substrates. The early development of epitaxial DBR was based on alternating layers of lattice-mismatched Al(Ga)N and GaN. Due to the large lattice mismatch (~2.4%) between AlN and GaN tensile strain is generated, potentially causing cracking. The small refractive index contrast between AlN and GaN require a large number of pairs (~40) to achieve reasonably DBRs, making the case even more challenging.

The lasing threshold for a VCSEL depends on the size of an aperture region open on top of the device, which allow for injection current, typically a few micrometres in diameter. A standard procedure for the fabrication of III-nitride VCSEL involves tedious steps to form the current aperture by means of dry-etching techniques, leading to sidewall damage and thus optical losses. Furthermore, due to the nature of p-type GaN, there exists a current spreading issue.

This chapter demonstrates a novel, patented approach to the fabrication of III-nitride VCSELs, which is achieved by developing a direct epitaxial method based on selective epitaxial growth. Although lasing behaviour has not been confirmed yet, microcavity effects have been observed under both optical or electrical pumping.

6.1 Introduction

The research on GaN-based VCSELs has faced a good progress during the last decade, although the performance III-nitride VCSEL performance stills far away from GaAs VCSELs. As described in Chapter 2, there exist several great challenges associated with both device fabrication and epitaxial growth. In 1999, Arakawa's team at the University of Tokyo reported the first room-temperature optically pumped GaN VCSEL emitting at 339 nm, where 43 pairs of

AlGaN/GaN bottom DBR and 15 pairs ZRO_2/SiO_2 based oxide top DBR were used [1]. The optical threshold was estimated to be 43nJ/pulse.

The conventional fabrication of VCSEL, for example, GaAs-based VCSELs, employs a standard annular p-contact [2,3]. However, it is extremely difficult to apply this method in the fabrication of III-nitride based VCSEL due to current spreading problems as a result of the nature of p-type GaN.

In 2008 the first electrically pumped GaN-based VCSEL operated at 77K in CW mode was reported [4]. Their device was based on a combination of an epitaxial grown bottom DBR (AlN/GaN) and a dielectric top DBR (Ta_2/SiO_2) with a current aperture in a diameter of 10 μm. Lasing with a linewidth of 0.15 nm was achieved with a current threshold of 1.8 K/cm^2 at 462.8 nm. Furthermore, high spontaneous emission coupling (β) has been observed, which is three orders of magnitude higher than that for a typic EEL. In 2010, the same research group reported electrically pumped lasing at room temperature with a threshold current density of 12.4 KA/cm^2, although the lasing threshold was not impressive compared to InGaN edge emitting lasers [5].

Nichia Ltd in Japan, one of the major III-nitride emitter suppliers reported the first electrically VCSEL with dielectric top and bottom DBRs in 2008 [6]. Their approach does not rely on the crystal quality of the microcavity on a single GaN epilayer, as they removed the foreigner substrate by using a laser lift-off (LLO) technique and then bonding to a Si substrate. In this case, the cracking issue could be mitigated. Although, the LLO process presents challenges itself due to high UV energy flux through the back side of GaN/Sapphire, such as thermal decomposition of GaN into N_2 and Ga droplets, Nichia managed to successfully develop VCSELs with a lasing threshold of 13.9 KA/cm^2 emitting at 414 nm by means of using an 8 μm diameter current aperture, SiO_2/Nb_2O_5 DBRs and ITO as a p-contact. In 2011, CW VCSELs at 451 nm and pulsed VCSEL at 503 nm operation have been achieved with a lasing current threshold of 3 KA/cm^2 and 28 kA/cm^2, respectively [7]. The dramatical increase in threshold current with increasing emission wavelength was assumed to be due to QCSE.

Sony joined the development III-nitride VCSEL, reporting a room-temperature CW green VCSEL grown on {20−21} semi-polar GaN [8]. Oxides have a low thermal conductivity around 1 WmK^{-1}, and thus the dielectric DBRs block the heat out of the cavity. One approach to mitigating the issue would be to extend the cavity length by using high thermal conductive GaN (130 WmK^{-1}). However, if the length of a cavity is on a scale of 20-50 μm, the diffraction losses increase potentially preventing lasing operation. Sony's approach used a curved surface

mirror, creating a waveguide that eliminate diffraction loss and thus minimising thermal resistance for GaN VCSELs.

In 2008, the first optically pumped blue-green VCSEL was reported, where lasing at 498.8 nm with a spectral linewidth of 0.15 nm was observed at room temperature (RT) [9]. In 2016, continuous wave lasing with a low threshold of 0.61 mA at RT was achieved using quantum dots (QD) at 560.4 nm [10].

DBRs are the key component to form an optical cavity. However, the growth-related challenges of III-nitride lattice-mismatched DBRs needs to be addressed. The potential of porous GaN based DBRs has been presented in Chapter 2. During the last decade, different groups focused their research on enhancing LED-Laser characteristics by using porous GaN. In 2015, Seung-Min Lee et al. reported the first optically pumped VCSEL based on top-bottom NP DBR leading to lasing at 410 nm and a low threshold density of 7-8 × 10^3 W/cm^2 [11]. Although their approach to forming top porous DBR is valid for violet emission, it presents challenges to reach longer wavelengths, as the temperature which is required above 1000^{o}C for the growth of top epitaxial DBR decompose InGaN MQWs (In~27%-green). Therefore, most of the research groups adopt a hybrid epitaxial-dielectric approach, namely, dielectric top DBRs and epitaxial bottom DBR.

In 2017, C. Zhang et al. presented the first electrically pumped blue-violet resonant cavity light emitting diode (RC-LED), based on nanoporous DBR and dielectric top DBR, emitting at 420 nm [12]. The linewidth emission of their device was narrowed down from 20 nm to 2.5 nm. In 2019, S.M. Mishkat-Ul-Masabih et al. reported the first electrically injected nonpolar m-plane VCSEL using nanoporous (NP) bottom DBRs and SiO_2/SiN dielectric top DBRs, where 20 pairs bottom NP-GaN DBRs with a 99.5% reflectance and 10 pairs of SiO_2/Ta_2O_5 dielectric DBRs were used [13]. Lasing at 408.7 nm with a threshold current of 20 KA/cm^2 was observed under a pulsed injection mode. In 2020 Chia-feng Lin et al. reported an InGaN based RCLED with an embedded bottom NP-GaN DBRs and top dielectric Ta_2O_5 / SiO_2 DBRs, which also shows a stimulated emission at 431.8 nm with a spectral linewidth of 0.7 nm under optical pumping [14]. In the same year, R. T. ElAfandy et al. presented the first room-temperature electrical pumping operation of c-plane GaN based VCSEL in a pulsed mode by using conductive NP-GaN bottom DBRs and SiO_2/HfO_2 top DBRs. The measured threshold current was 42 KA/cm^2 at 434 nm [15].

Clearly, the formation of the current aperture presents some challenges, due to anti-guiding effects and the etching down of a few nanometres of dielectric material [16,17]. In order to overcome the challenges, this thesis develops a new approach based on selective epitaxy. Figure 62 illustrates the schematic process

flow, where a GaN layer is grown on top of an epitaxial grown DBR, after that, SiO_2 is deposited, micro holes are patterned and etched down, then a subsequent growth forms microemitters inside the holes, finally a current spreading layer and a dielectric DBR is deposited. Thus, as the microemitter is selectively growth and confined into the SiO_2, anti-guiding effects could be avoided.

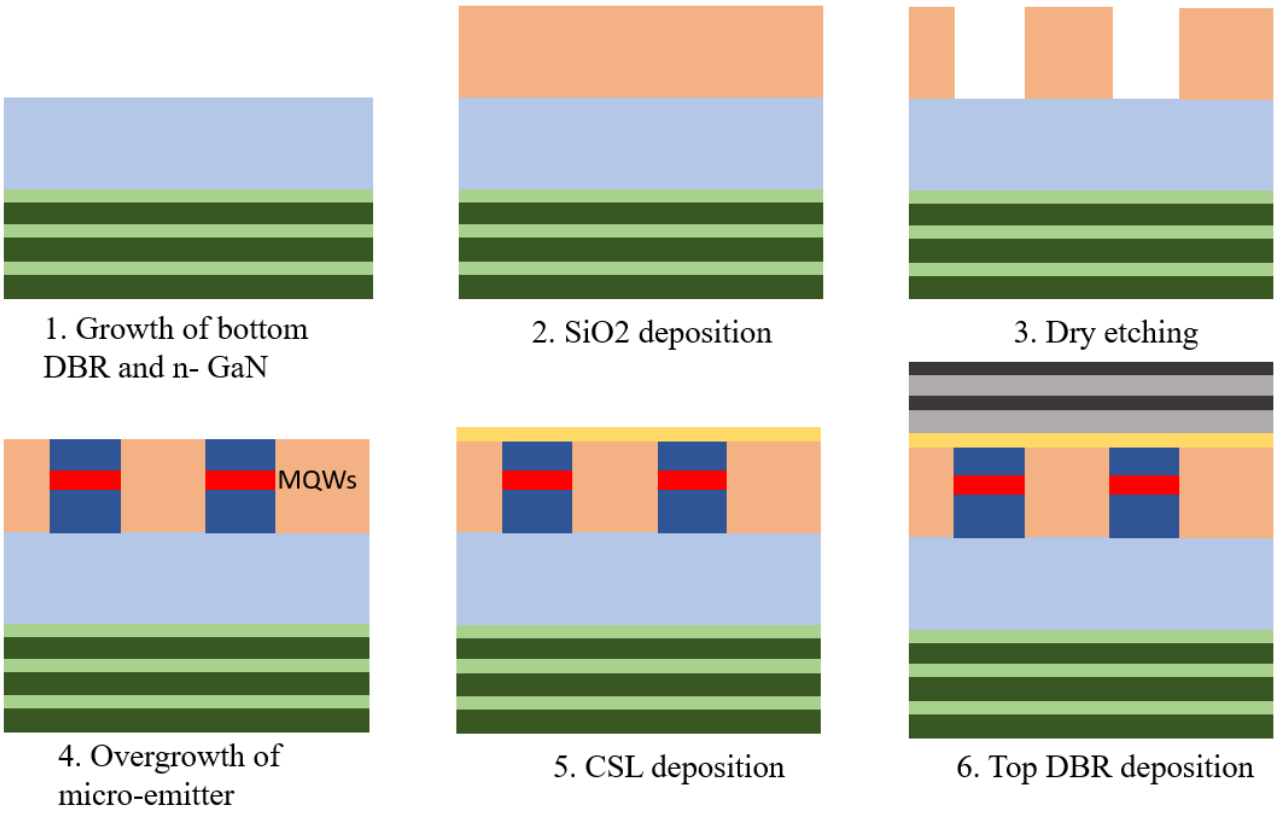

Figure 62: Concept of micro emitter growth on a micropatterned structure.

6.2 Experimental

6.2.1 Dielectric DBR deposition and refractive index tunning

The previous chapter described the development of high reflectance NP-GaN DBRs on c-plane. In order to form a hybrid VCSEL, top dielectric DBRs must also be optimised. It is necessary to optimise the deposition of dielectric materials such as SiO_2 and SiN and number of pairs using PECVD, aiming to achieve >99% reflectance. It is worth noting that the refractive indices of SiO_2 and SiN depends on a number of parameters including the PECVD manufacturer and the recipe used (i.e. temperature, gas ratio, pressure and power). Thus, it is critical to obtain the refractive index and the deposition rate of our dielectric layers.

For optimisation purposes, dielectric films (SiO_2-SiN) were deposited on a sapphire or a silicon substrate by means of a Plasma-Therm 790 PECVD system. The imaginary part of the refractive index which is related to the absorption loss is considered to be negligible at 520 nm [18]. In both cases, SiO_2 or SiN is

deposited at 300 °C. The optical properties of the dielectric film were characterised using an ellipsometer system, measuring the spectroscopic scan is taken at 60° and 65°. The experimental data was then compared to a model where the dielectric layers are described as a Cauchy material.

Figure 63a) illustrates the measured spectroscopic spectrum which is compared with the model. PSI (Ψ) represents the change in polarisation described as an amplitude ratio and Delta (Δ) is the phase difference. The dashed line represents the calculated data from the model, a good agreement is obtained with an MSE<10.

Figure 63b) shows the dispersion plot for the refractive index of SiO_2 and SiN as a function of wavelength. The measured refractive index difference (Δn) is 0.47 at 520nm (n_{SiO2}=1.45, n_{SiN}=1.92), giving the stopband of the DBR to be estimated > 100 nm using Equation 13 provided in Chapter 2.

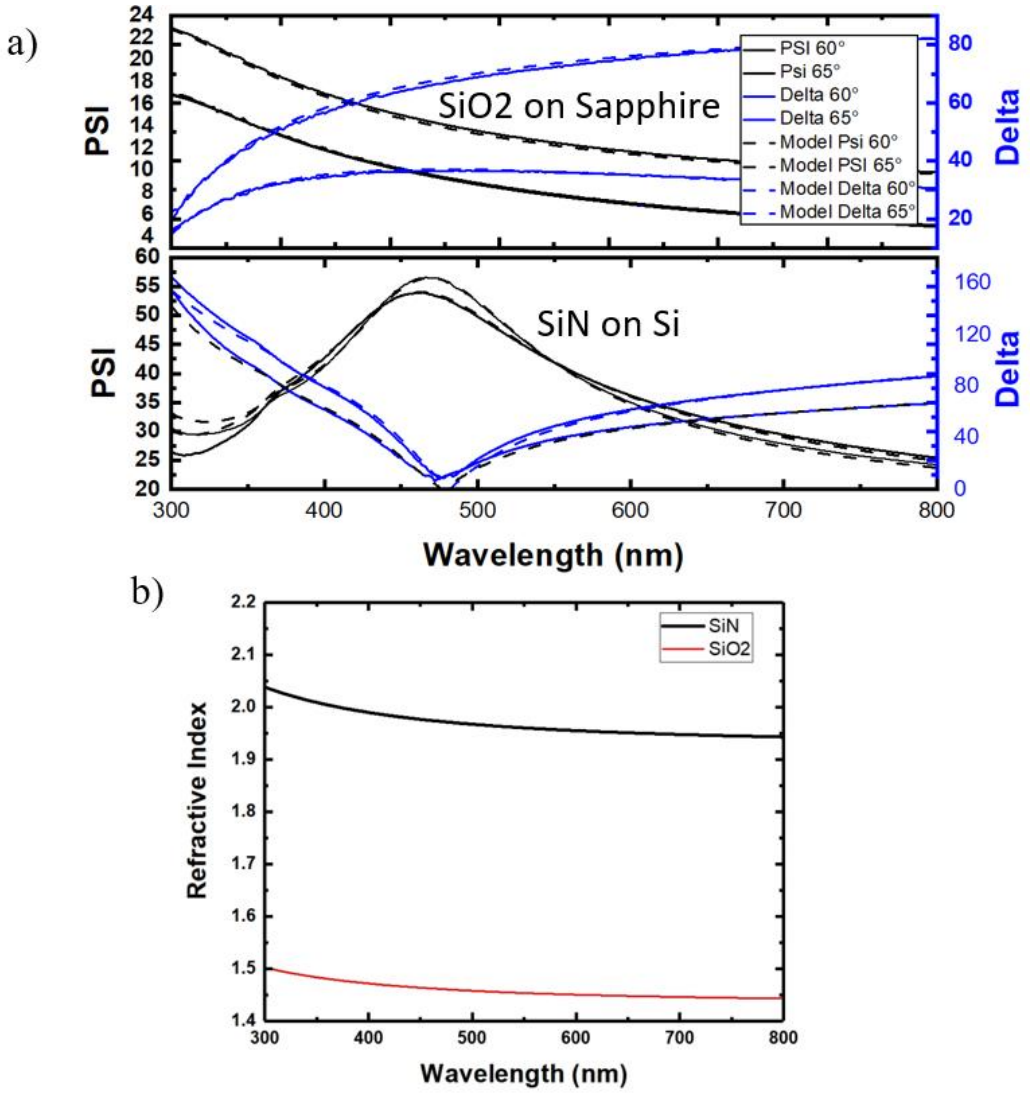

Figure 63: a) Ellipsometer modelling and measured data of SiO2 on sapphire and SiN on Si. b) Obtained refractive index.

Such a DBR structure with a stopband of 100 nm is large enough to spectrally overlap InGaN microemitters whose FWHM is typically around 45 nm, as demonstrated in Chapter 5. A study of the peak reflectivity of DBRs with centre wavelength of 520 nm was carried out. The deposition of the oxide layer was carried out at 900 mTorr, with RF power set to 25 W and a mixture of gasses (SiH_4, NH_3, N_2) with flow rates of 160, 900 and 240 sccm respectively. Meanwhile, to obtain the nitride layer the flow rate of SiH4, NH3, N2 was slightly modified to 100, 5 and 900 sccm. Thus, quarter lambda layers were deposited on sapphire substrate, corresponding to an approximated thickness of 90 nm and 67 nm for the oxide and nitride layer respectively. FDTD simulations were carried out in order to validate the experimental results.

Figure 64 demonstrates the peak reflectivity of a DBR as a function of the number of pairs, showing that the reflectivity saturates once the number of pair exceeds 12.

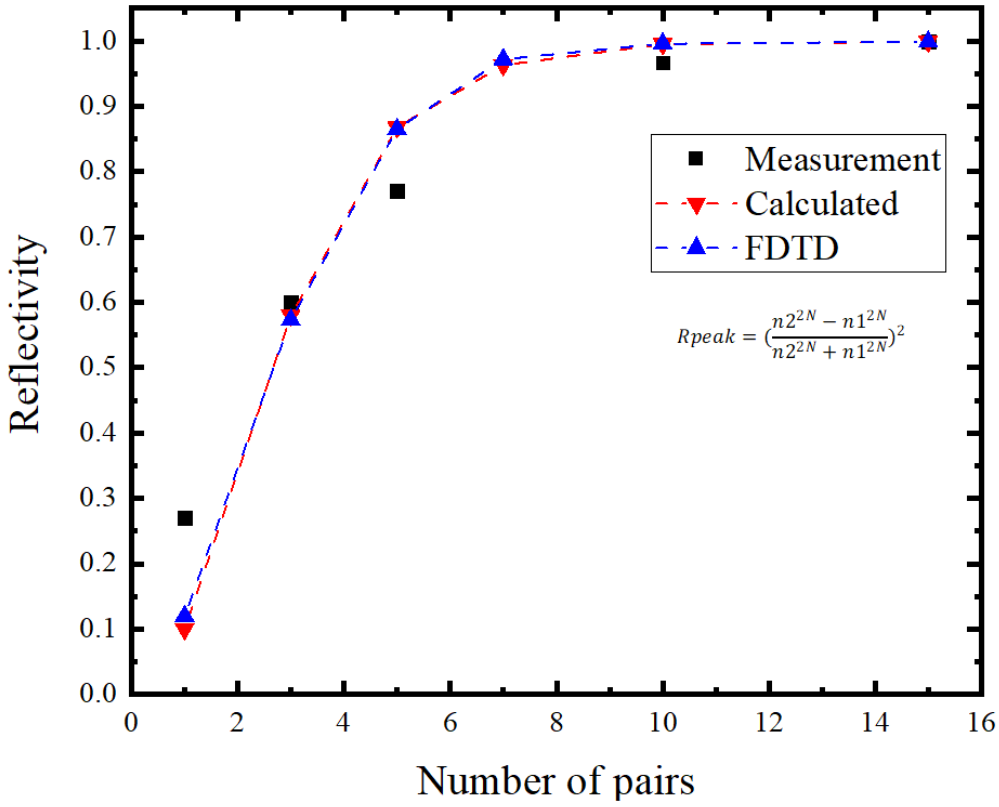

Figure 64:Peak reflectivity of a 520nm DBR as a function of the number of pairs.

After the top DBR was properly optimised, the fabrication process was carried out as described in Figure 64. An initial run formed the GaN templates on sapphire with 11 pairs of bottom n++GaN/u-GaN DBR, SiO_2 was deposited, patterned and etched, to be used as a mask to form the micro emitter array (Figure 65a)). Then, the selective overgrowth took place to grow the microemitter inside

the prepatterned hole, Figure 65b). After that, electrochemical etching was carried out in order to form the porous DBR. Subsequently, standard device fabrication was carried out (see Chapter 5). After p-activation, the MESA was etched to allow n-contact formation (Ti/Al/Ti/Au) and ITO/Ni-Au was used as a current spreading layer. Thick metal bondpads were deposited in order to carry out electrical measurements, as shown in figure 65c). Finally, the top DBR was deposited on top of the fabricated device, and window openings were etched through the DBR to allow the electrical path. Thus, the sample is repatterned and ICP dry etching technique is used to etch the DBR from the bondpads, Figure 65e).

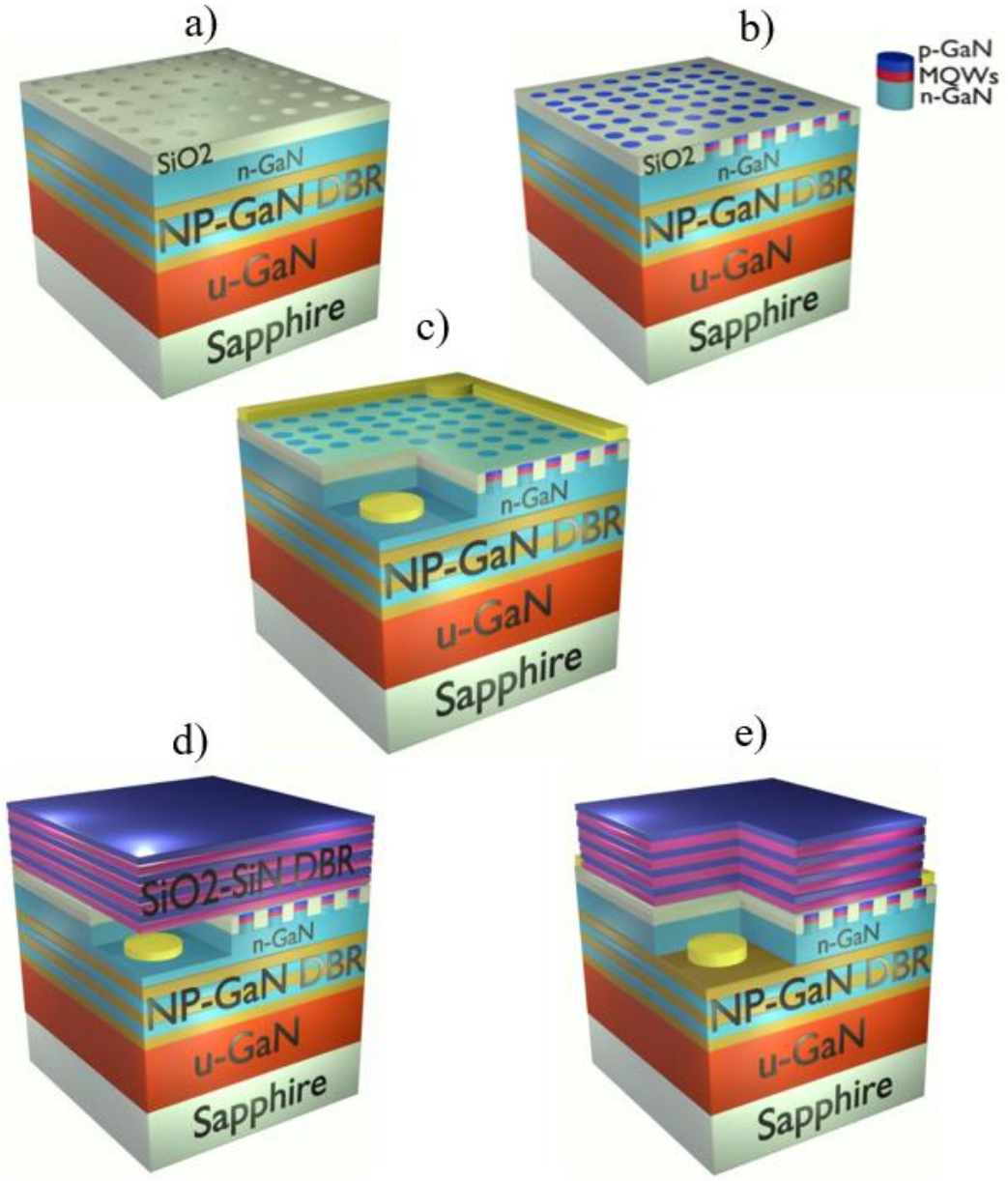

Figure 65: a) Deposition and formation of microholes through PECVD and ICP etching. b) Overgrowth of microemitters into the prepatterned µhole. c) Standard device with µLED and DBR. d) Dielectric DBR deposition. e) Opening of windows through the DBR to reach the bondpads.

6.2.2 Modelling of a hybrid dielectric-nanoporous based VCSEL

In order to confirm the potential existence of cavity modes in our micro-emitters achieved by selective epitaxy approach on micro-patterned templates, a 3D FDTD simulation has been carried out. The refractive index of NP-GaN sensitively depends on porosity, which can be accurately characterised by using a cross-section SEM image, where a binary image formed from the cross-section SEM was used to determine the porosity. A good agreement has been obtained between simulation and measurements, which can be confirmed as Figure 66 shows the agreement between simulated and measured reflectance of the NP-GaN based DBR. The extracted refractive index for the porous layer is 1.92.

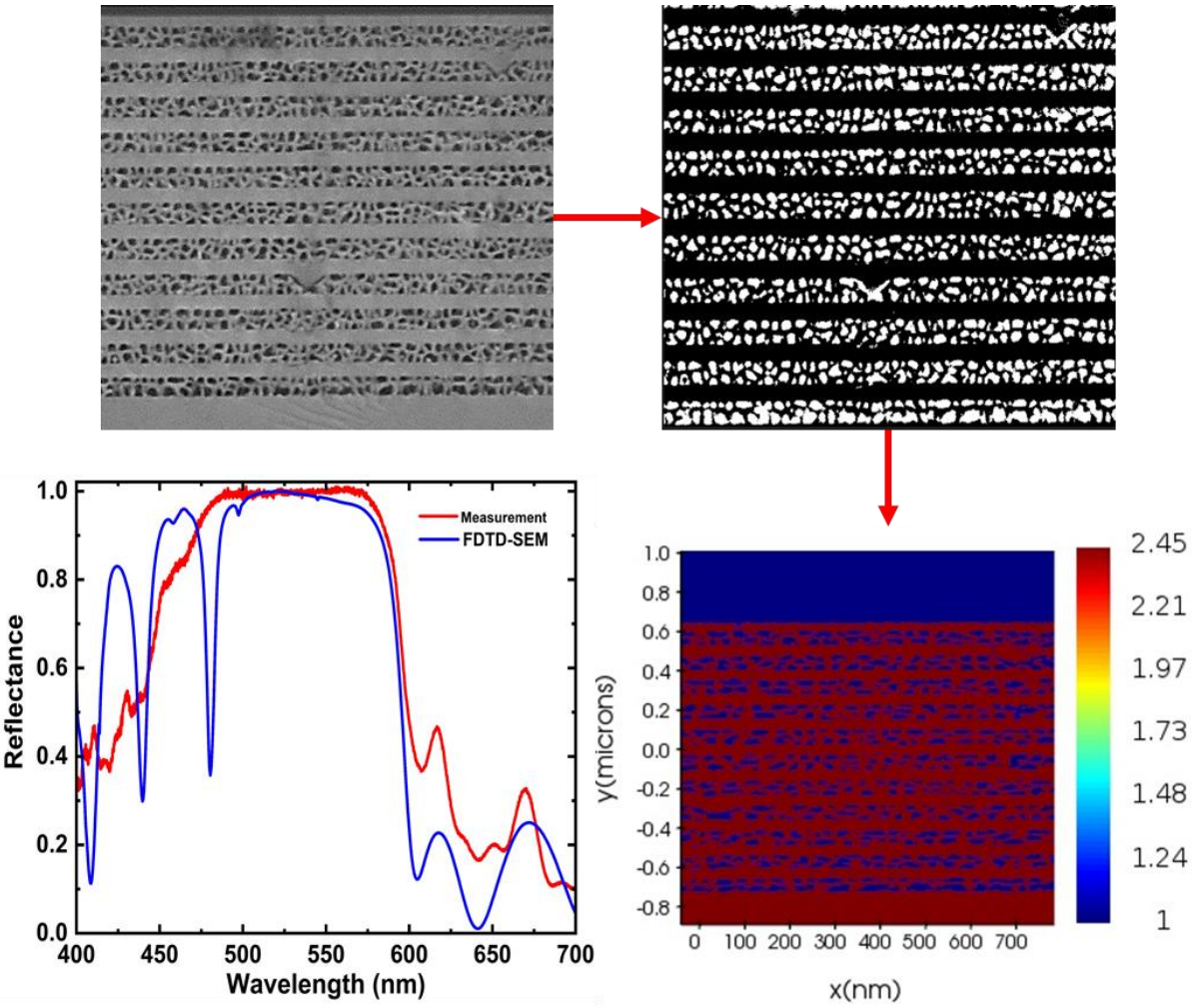

Figure 66: SEM image processing to estimate the refractive index on porous GaN.

A full microcavity was then simulated by adding the top dielectric DBR which consists of 12 lambda quarter pairs of SiO_2 and SiN. In order to determine the cavity resonances, time monitors were placed in the micro-emitter area. For the details, please refer to the procedure stated in Section 5.3.1.

Figure 67a) illustrates the simulated reflectivity spectrum of such a hybrid microcavity, showing spectral dips corresponding to the cavity modes. In order to study the fields inside the cavity, a linear monitor was placed in the Z axis to record the field at the chosen wavelength of 540 nm. The electric field distribution inside the cavity and the refractive index can be seen in Figure 67b), where the MQW and the ITO have been placed at an antinode and node of the electric field to maximise the confinement factor and minimise the absorption losses respectively. The free-spectral range of the cavity modes is 42nm, which agrees with the estimated FSR ~ $(\frac{\lambda^2}{2Ln})$,considering $\lambda = 520\text{nm}$, L_{eff}=1300nm and n_{eff}=2.44.

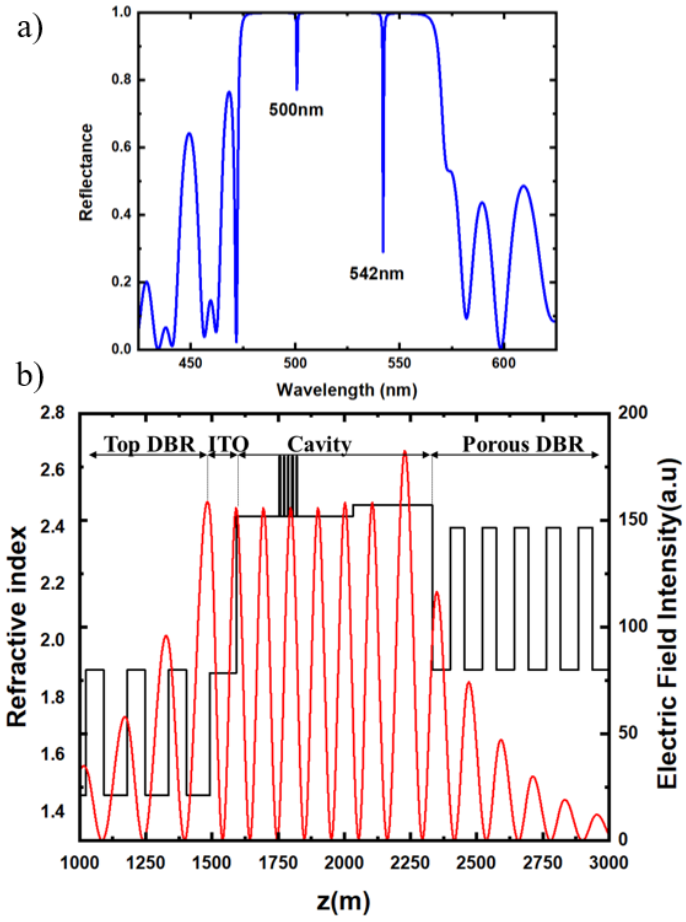

Figure 67: a) Simulated reflectance of the microcavity. b)Electric Field (Ez) at the mode wavelength (540nm).

The presented simulations demonstrate the existence of cavity modes at the given green emission wavelength. Therefore, coupling between the modes and the MQW could lead into microcavity effects.

6.2.3 Current voltage characteristics optimisation

6.2.3.1 Nanoporous Etching optimisation conditions

The last part of chapter 5 introduced a drawback of the EC etching, where the microemitters and the n-GaN layer beneath of it, were unintentionally porosified, leading into a high differential resistance. In order to maximise the injection of carriers into the active region, to increase the chances of lasing, the I-V curve need to be optimised. Furthermore, it has been observed that although the sample appears to be etched under the microscope, some areas are highly ununiform. Figure 68, illustrates the SEM cross section view of a microemitter with a porous DBR, where only 6 pairs are porosified successfully. Thus, based in the simulation presented in Chapter 5, the reflectance in this area could be reduced to 85%, which would have a negative impact in the lasing threshold.

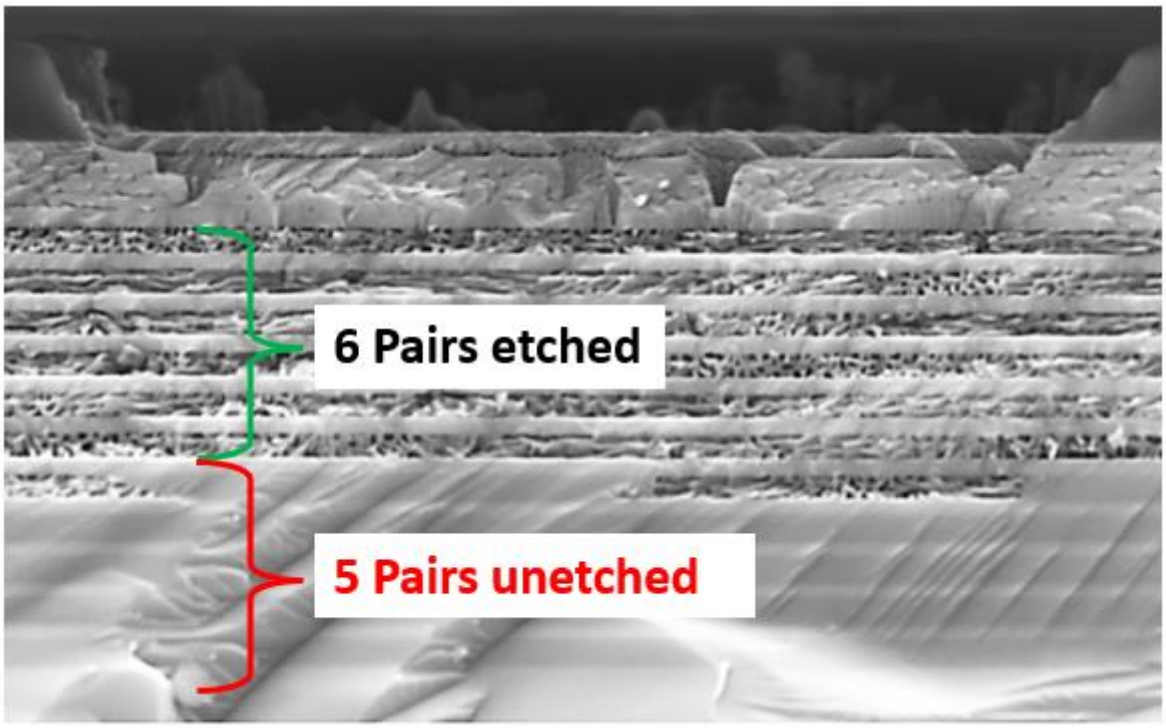

Figure 68: SEM image of a microemitter with ununiform porous DBR.

In order to achieve a uniform etching, a lateral EC etching approach via opening trenches was adopted. This was achieved by depositing a 500 nm SiO_2 layer at the surface by means of PECVD. Trenches with 100 µm width and 1 mm pitch were patterned and successively etched by standard photolithography techniques and inductive coupled plasma (ICP) etching. The electrochemical etching was carried out using the same approach described in Chapter 5. However, in this case a study on the acid concentration and etching voltage was implemented. Reflectivity and SEM characterisation were used to find the best etching conditions.

As it was explained in previous chapters, a high reflectance (>99%) is critical for VCSEL devices. However, an inherent trade-off between FWHM (related to etching voltage) and n-GaN parasitic etching damage exist in our samples. The EC etching voltage was reduced from 6V to 4V, to minimise the etching on the n-GaN while the nitric solution concentration was increased to 1M. The laterally etched sample relies on trench openings, from now referred as a sample A. The vertically etched sample is etched directly and is referred as sample B. An epi-wafer was grown using the same approach explained in Chapter 5, were a 11pairs n++GaN/u-GaN is formed above a thick GaN layer, previously grown on sapphire by means of a MOVPE. In addition, another wafer was grown with an extra 300nm n-GaN on top of the DBR to verify the existence of parasitic etching. Figure 69 shows an optical microscope image of the surface of both samples.

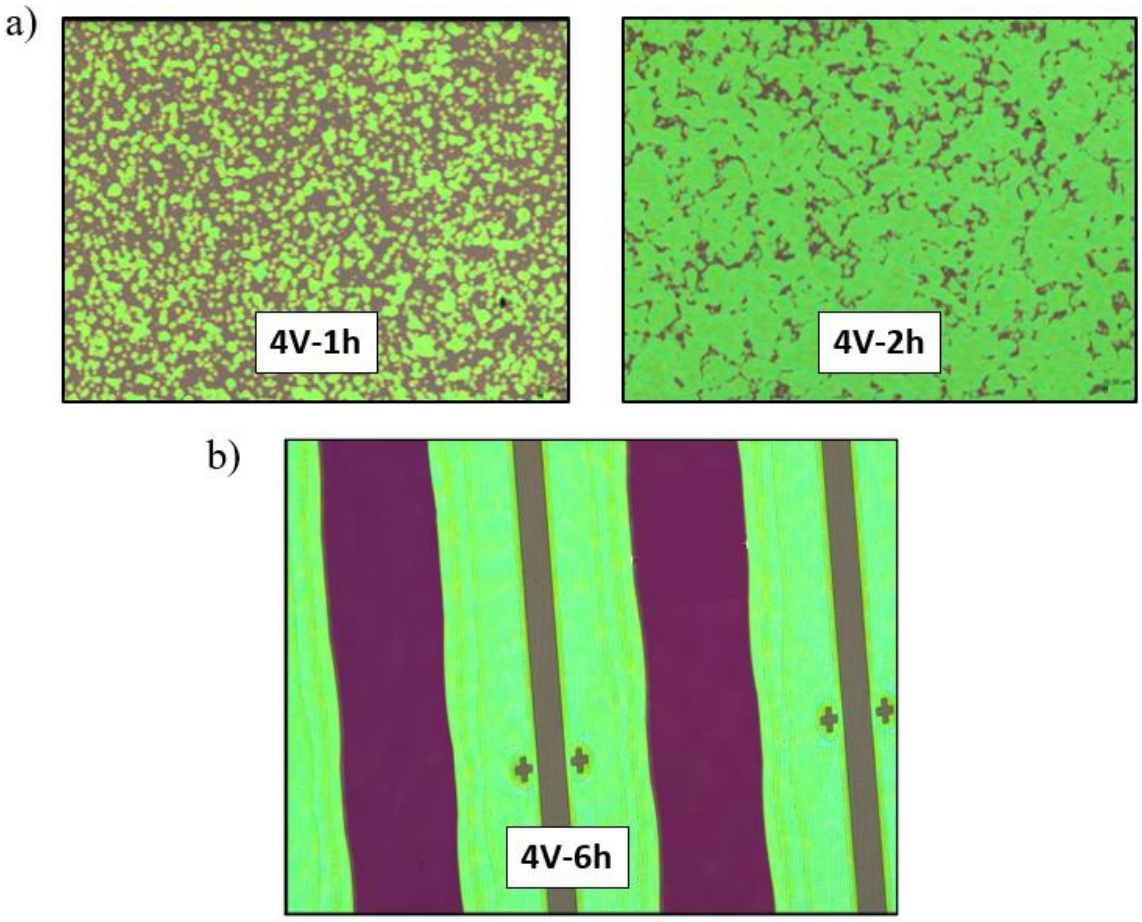

Figure 69: a) Microscope view of a sample etched during 1h (left) and 2h (right) at 4V. b) Microscope view of a sample etched with a lateral approach.

The major difference between vertical EC etching and lateral EC etching has been observed. Thus, sample A shows a circular etching pattern where the EC process is conducted through V-pits, which are formed from screw and mixed type dislocations. In this mechanism, such defects form nanopipes as channels to allow the electrolyte to access the doped layers. Therefore, etching behaves along the

vertical direction through layer by layer sequentially from the top. In contrast, sample B is etched perpendicular to the trench lines. Figure 70 shows the cross-section images of a DBR etched along the vertical direction and the lateral direction, respectively, demonstrating the major advantages of EC etching along the lateral direction, namely, much more uniformly distributed porosities formed along the lateral direction than those formed along the vertical direction.

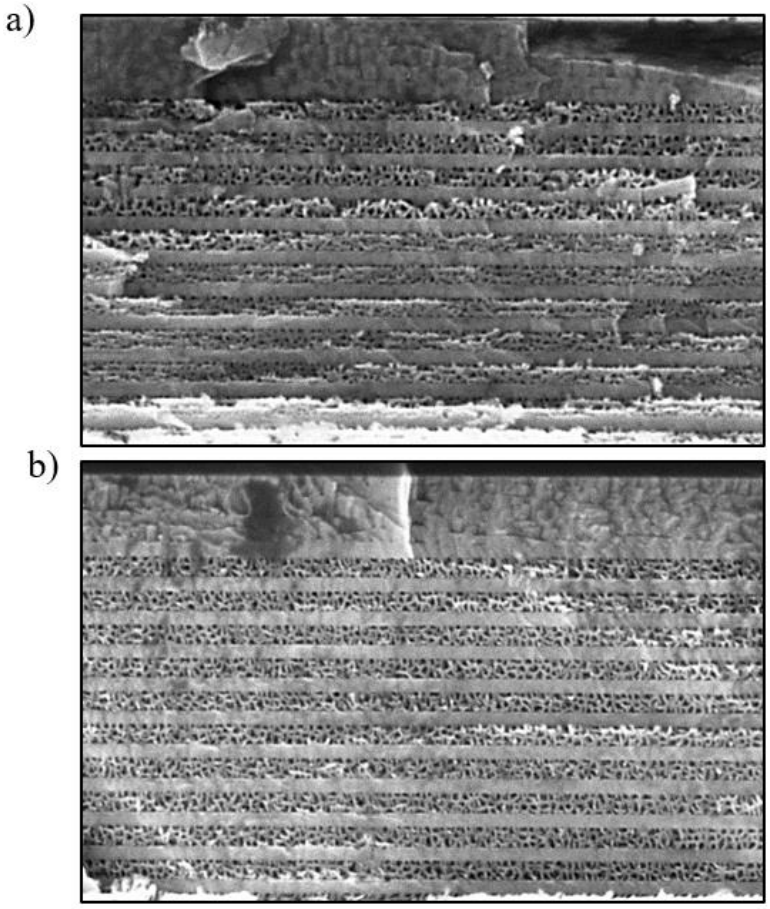

Figure 70: Cross section SEM image of a vertical (a) and lateral (b) etching with 300nm n-GaN on top.

The reflectance was measured on the DBRs formed along the different directions at normal incidence using the micro-EL setup described in Chapter 3. Figure 71, shows that the DBR formed along the lateral direction (Sample A) exhibits a minimum stopband of 98 nm, meanwhile for the vertically etched DBR (sample B) the minimum stopband is 90 nm, this fact is related to the higher porosity achieved through the lateral etching. It is worth noting that the DBR formed along the vertical direction presents a shift in wavelength from 520 nm originally desired, especially for the top part which has a centre wavelength of 563 nm. The FWHM has been slightly reduced from 120 nm to 94 nm, compared to the DBR presented in Chapter 5, mainly due to a lower bias voltage.

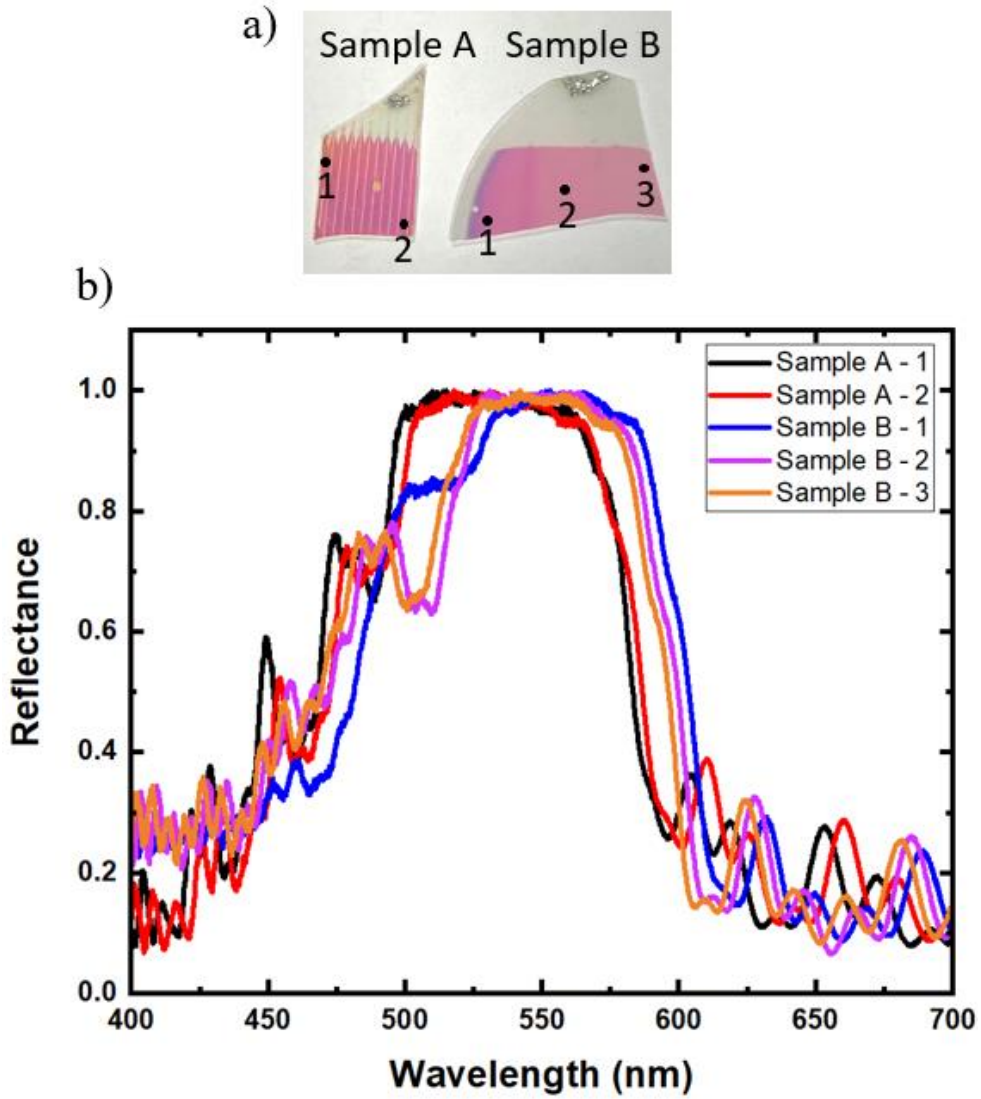

Figure 71: a) Image of Sample A (Lateral etching) and sample B (defect-etching), where the number indicates the position where the reflectivity was measured. b) Measured reflectivity in Sample A and sample B

The effect of the nitric solution concentration on the DBR characteristics has been also studied on another set of samples. Thus, in order to measure the difference in peak reflectance, the same etching bias (4V) and different electrolyte molar fraction were applied to different pieces of the same wafer. Figure 72 illustrates the reflectance measurements of two different samples, with a dielectric DBR as a reference. It can be observed that the centre wavelength of the DBR can be tuned by changing the acid concentration which leads to the porosities with different diameters.

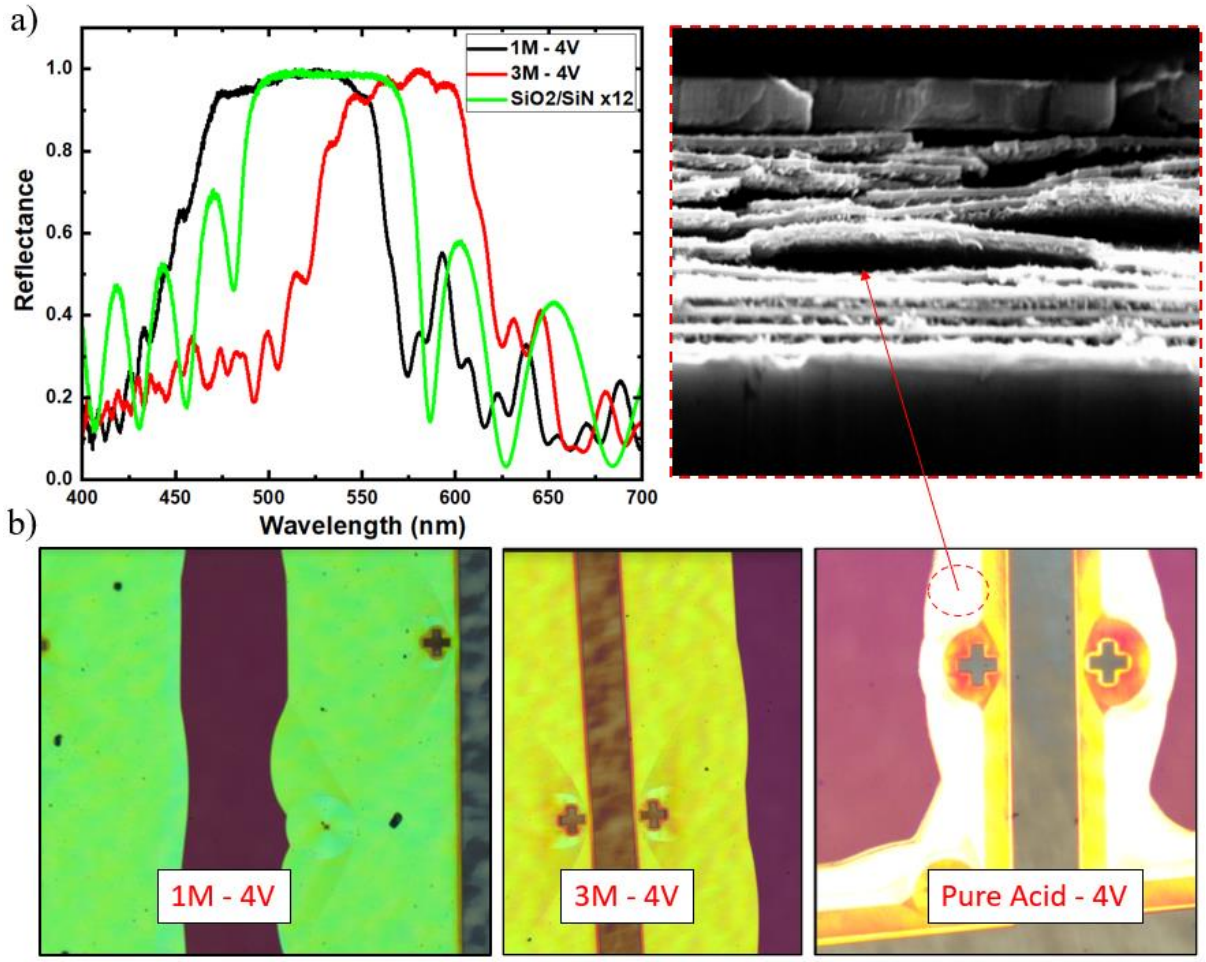

Figure 72: a) Reflectance of DBR under different acid concetration, dielectric DBR added as a reference. b) Microscope image of the same sample etched under different electrolyte conditions.

The ripple on the pass band is assumed to be related to the SiO_2 interference. Figure 72b) illustrates the microscope and CSV images of studied samples. Clearly, another trade-off appears between etching rate and the acid concentration, the etching rate was measured to be 1.25 µm/min and 0.83 µm/min for the 3M and 1M electrolytes. Etching on pure acid resulted in the highest etching rate ~2.46 µm/min, however the DBR layers were completely cracked, giving place to lift off.

Lateral porous formation has been reported by other groups since 2010 [20-23]. However, the etched area has been always kept to a few hundreds of micrometres. In this work a 1mm etched has been achieved by EC etching during 11h, which is the larger reported as per our knowledge. Figure 73a) shows the measured reflectance at different areas of an etched quarter wafer. Figure 73b) shows a microscope image of the etched sample. In order to check the continuity of the process, the etching was stopped multiple times, the observed lines correspond to changes in porosity due to process stoppage.

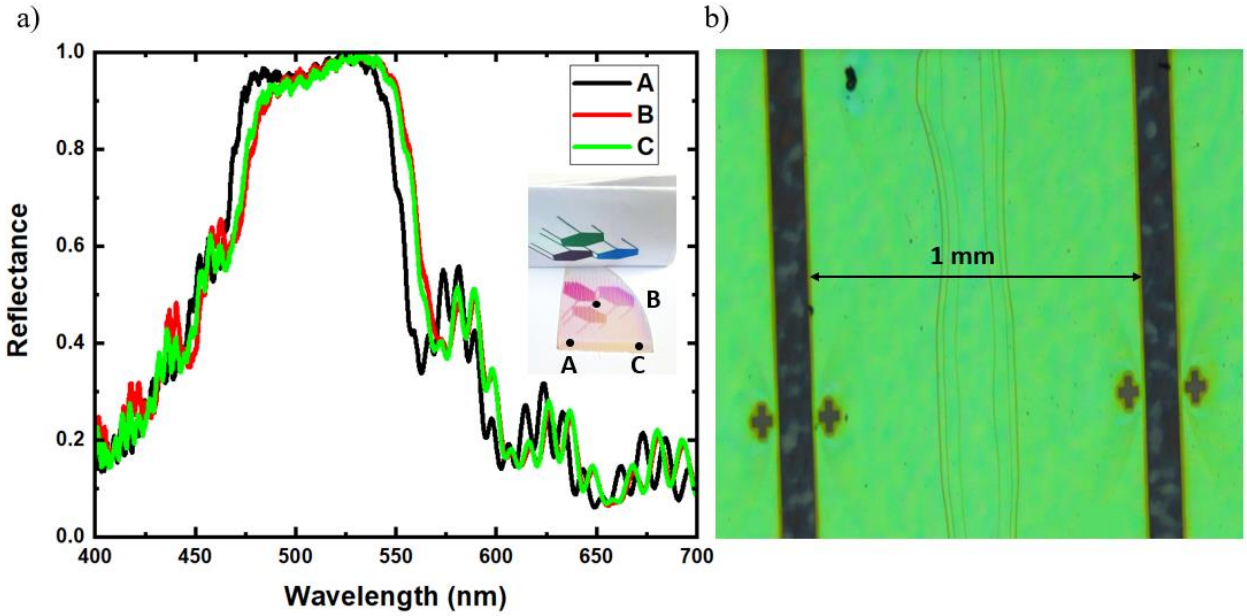

Figure 73: a) Measured reflectance taken at three different points. b) Optical image of a sample etched 1mm.

One of the concerns of NP-GaN based devices is the porosity distribution randomness. However, as shown in the cross-section SEM image (Figure 70), the lateral etching approach led to a more uniform porous distribution, which also is proved with the reflectance spectrum around the quarter wafer, shown in Figure 73a). Therefore, a potentially uniform wafer-scale approach formation could be feasible. Thus, the remaining half wafer was etched under the same conditions (4V bias – 1M electrolyte) during 18h. Unfortunately, the porosification process seems to be drastically slowed down, and finally stopped, leaving a 380 µm gap unetched between trenches (Figure 74). The main reason seems to be a limiting factor in the kinetics of the reaction due to the relation size ratio between the sample and the Pt pad (2cm x 2cm) [23]. In principle the surface area of the counter electrode should be must larger than the working electrode.

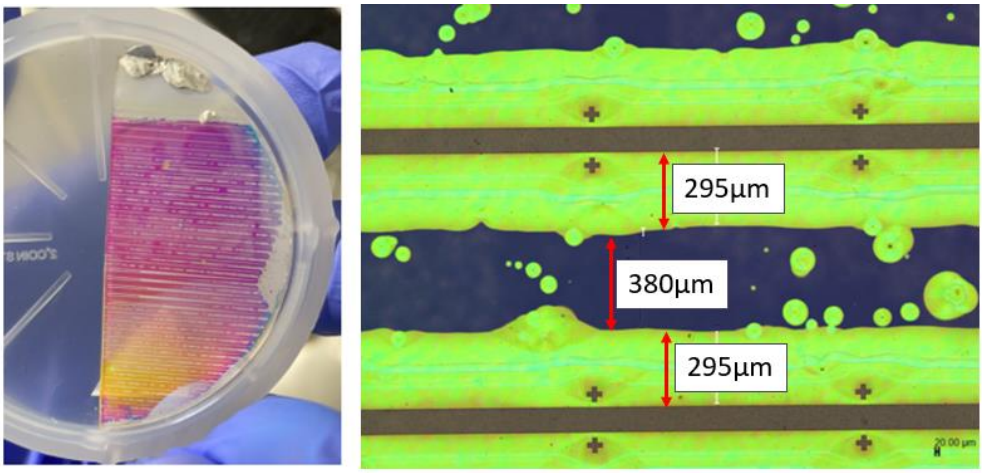

Figure 74: Picture of the etched half 2" wafer (left) and its optical image (right).

The new etching conditions (4V - 1M) could lead to less parasitic etching into the microemitter and the n-GaN layer above the DBR. Thus, improving the injection of carrier into the active region. In order to prove this fact, two pieces of the same wafer used in Chapter 5 (containing microemitters) were EC etched. Sample A corresponds to vertical etching using 6V and 0.3M HNO_3, while Sample B is the sample etched at 4V bias and 1M HNO_3 electrolyte. Figure 75a) and Figure 75b) illustrate the cross-section SEM image of a microemitter etched with old and new conditions, where the microemitter in the lateral etched sample seems to be less damaged. Finally, standard LED fabrication process was carried out to quantise the device resistance improvement. However, in order to increase the current density of each microemitter, the size of the MESA has been reduced to 80 x 80 µm and 100 µm x 100 µm. It is well known that III-nitrides performance is limited by the poor ohmic contact at the metal/GaN interface. Semi-transparent ITO and thin Ni/Au layers are normally used as a p-contact. In terms of transparency, ITO seems a better option. However, Ni/Au forms a better Ohmic contact on p-GaN. Therefore, aiming for a enhanced electrical characteristics a thin layer of 10 nm - 10 nm Ni/Au was used as a p-contact.

Figure 76 illustrates the current voltage characteristics improvement due to the optimised EC etching conditions. The corresponding total resistance based on the I-V plot is 198 Ω for the unetched device (without DBR). Meanwhile, the device vertically etched under 6V presents a high resistance ranging from 3.3 KΩ to 666Ω, proving the non-uniformity of the vertical porous formation. The resistance of the device with optimised conditions is 248Ω. Thus, the overall performance of the device could greatly be enhanced.

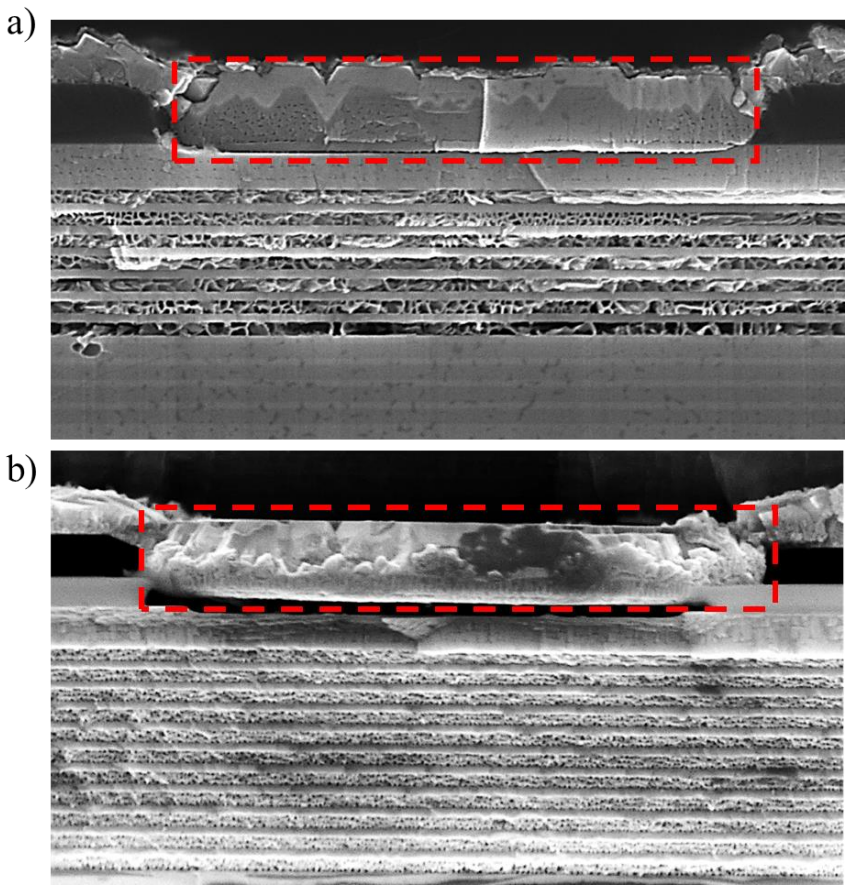

Figure 75:a) Cross section view of a sample vertically etched at 6V - 0.3M for 1h, where 5 pairs of n-GaN still unetched. b) Lateral etched sample at 4V-1M for 12h.

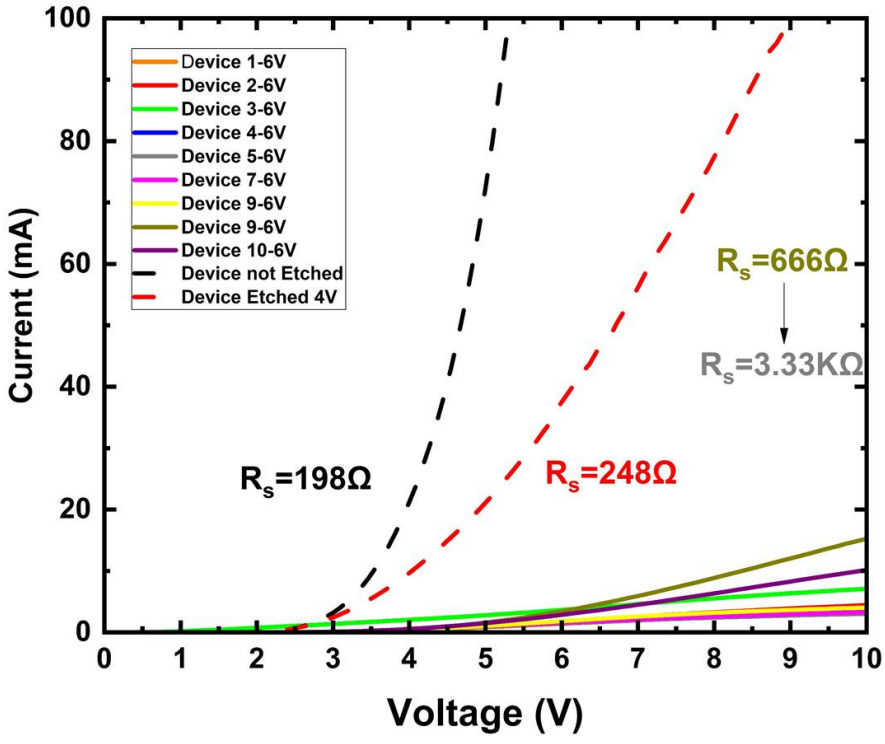

Figure 76: I-V characteristics of devices with old etching conditions and the optimised etching conditions.

6.3 Results and discussion

6.3.1 Electrical and optical characteristics

The overgrowth VCSELs were characterised first under photoluminesce excitation. Thus, power-dependant PL measurements were performed to investigate microcavity effects. The measurements were carried out by means of a commercial confocal microscopy (described in Chapter 3), allowing excitation of single microemitter devices. Figure 77, illustrates the normalised emission from the same sample measured at different stages of the fabrication, where as-grown refers to the sample without any DBR, and porous and top and bottom DBR refer to the sample with a bottom and top and bottom DBR respectively. As, it was expected the deposition of the top DBR produces stronger cavity modes, a sharp peak appeared at 547 nm with a linewidth of 4 nm. Furthermore, the other lower peaks appear in the emission spectra.

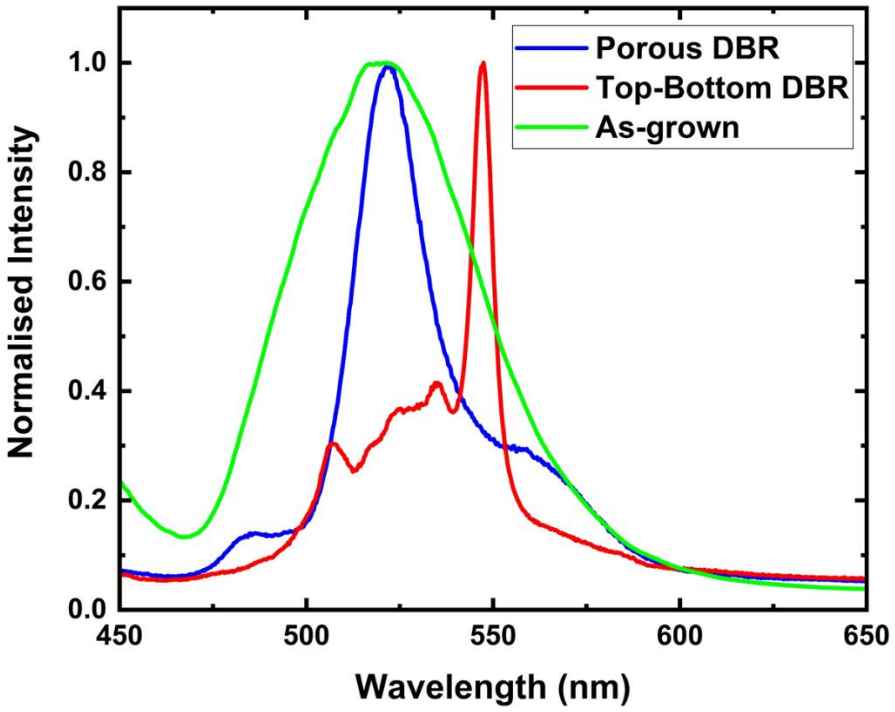

Figure 77: Normalised confocal PL of the sample without DBR (green), with porous DBR (red) and with porous-dielectric DBR.

In other to prove that the observed peaks are modes and the presence of lasing, power dependant PL was carried out. Figure 78 displays power-dependant PL spectra with an excitation power from 0.25 mW to 1.5 mW. It can be observed that as the power increases a possible mode located at 547nm dominates the emission. However, no clear reduction of the FWHM or an abrupt change on the integrated intensity has been observed, therefore lasing it is not achieved. The spectrum shows another mode at 506nm, the spacing between modes matched well with the simulation presented in the last section. However, other possible

modes appeared with a spacing of 10nm, which does not match with the expected FP. In order to verify the experimental results, a complex study of the modes was carried out in a 3D-FDTD simulation.

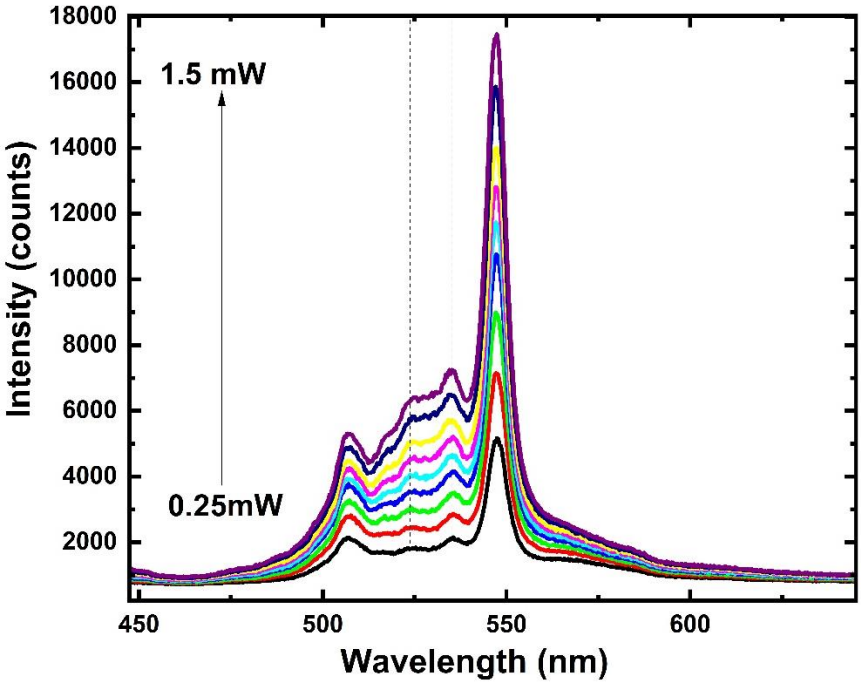

Figure 78: Power dependant PL of a microemitter with porous and dielectric DBR.

In order to find any possible kind of resonance (FP or WGM), electric dipoles were placed around the active region of the microemitter. Time monitors were located the periphery and the centre of the cavity region, which are the areas that can have strong field interactions. To reduce the memory requirements the cavity was defined with a single layer acting as active region, instead of individual MQWs. Figure 79 illustrates the normalised confocal data and the simulated spectral distribution. The free spectral range between the observed peaks is within the range of the FP spacing obtained in the simulations. The position of the spectral peaks is shifted due to inaccuracies in the modelling.

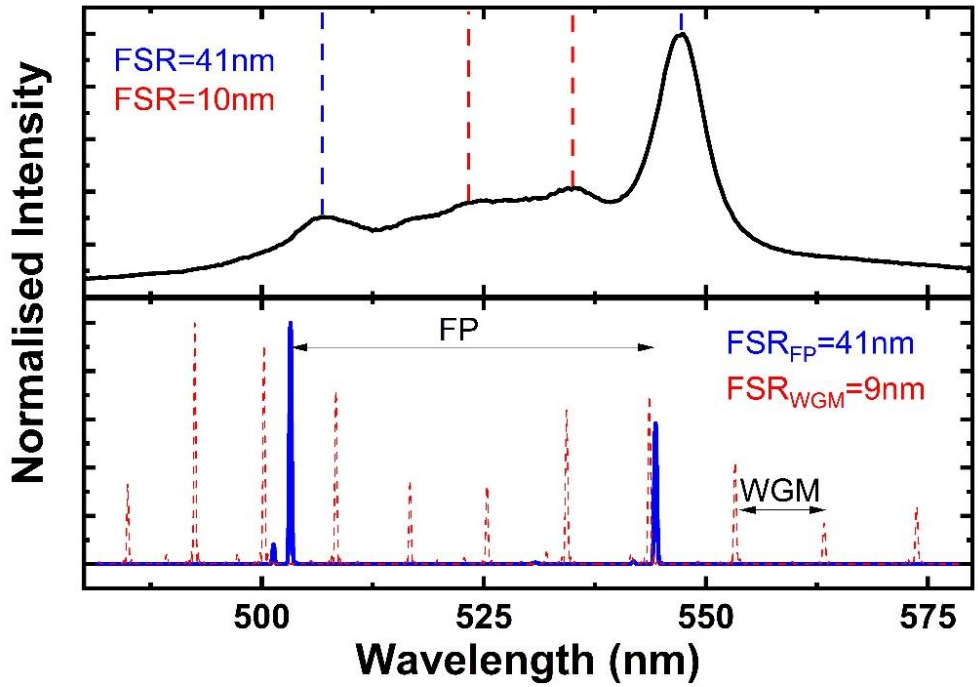

Figure 79: Normalised confocal PL. Simulated WGM (red) and FP (bottom) modes.

Electroluminescence properties were studied by using the µEL setup described in Chapter 3. Standard LED fabrication was carried out, including EC etching, dielectric DBR deposition, window opening and using ITO/Ni-Au as a p-contact. Thus, two samples were studied: one without any DBR (sample A) and the other with top and bottom DBR (sample B). The samples were electrically driven under CW regime with electrical probes and a Keithley SMU used as a source. Figure 80a) illustrates the emission image of the device with two DBRs under 20 mA, current crowding can be observed, where light is not uniformly spread across the current spreading layer. After repeating the process, it was assumed that the long DBR PECVD deposition of 12 pairs SiO_2/SiN at 300 °C damaged the ITO. The same issue was encountered while using Ni/Au. In fact, later in this chapter the use of ICPCVD to achieve a non-damaged current spreading layer is discussed. Although the ITO is damaged, it is possible to observe some highly bright microemitters near the p-bondpad. As the current is not spreading uniformly, a huge current density must be pumping the MQWs of the microemitters. Therefore, the light was collected from those bright spot areas using a high magnification lens. Figure 80b) shows the EL spectra as a function of injection current of the sample A, where interference fringes due to the large refractive index contrast of Sapphire-GaN-air are observed. While Figure 80c) illustrates the spectra of the sample B, where a clear main mode at 540 nm is observable. As the current increases, a 'shoulder' appears at 509 nm. The spectral spacing between the two peaks is ~31nm, which is slightly smaller than the simulated FSR presented in the previous section. The inexistence of lasing is assumed to be related with the

mode-competition between these two modes. Figure 80d), illustrates the current stability due to the microcavity effects. The emission wavelength shifting on sample A is 20 nm, attributed to be a consequence of the QCSE. Sample B shifting is less than 1 nm. The inset in figure 80d), illustrates the narrowing in FWHM caused by resonant cavity effects. The linewidth of sample B has been reduced by a factor of 5 compared with sample A.

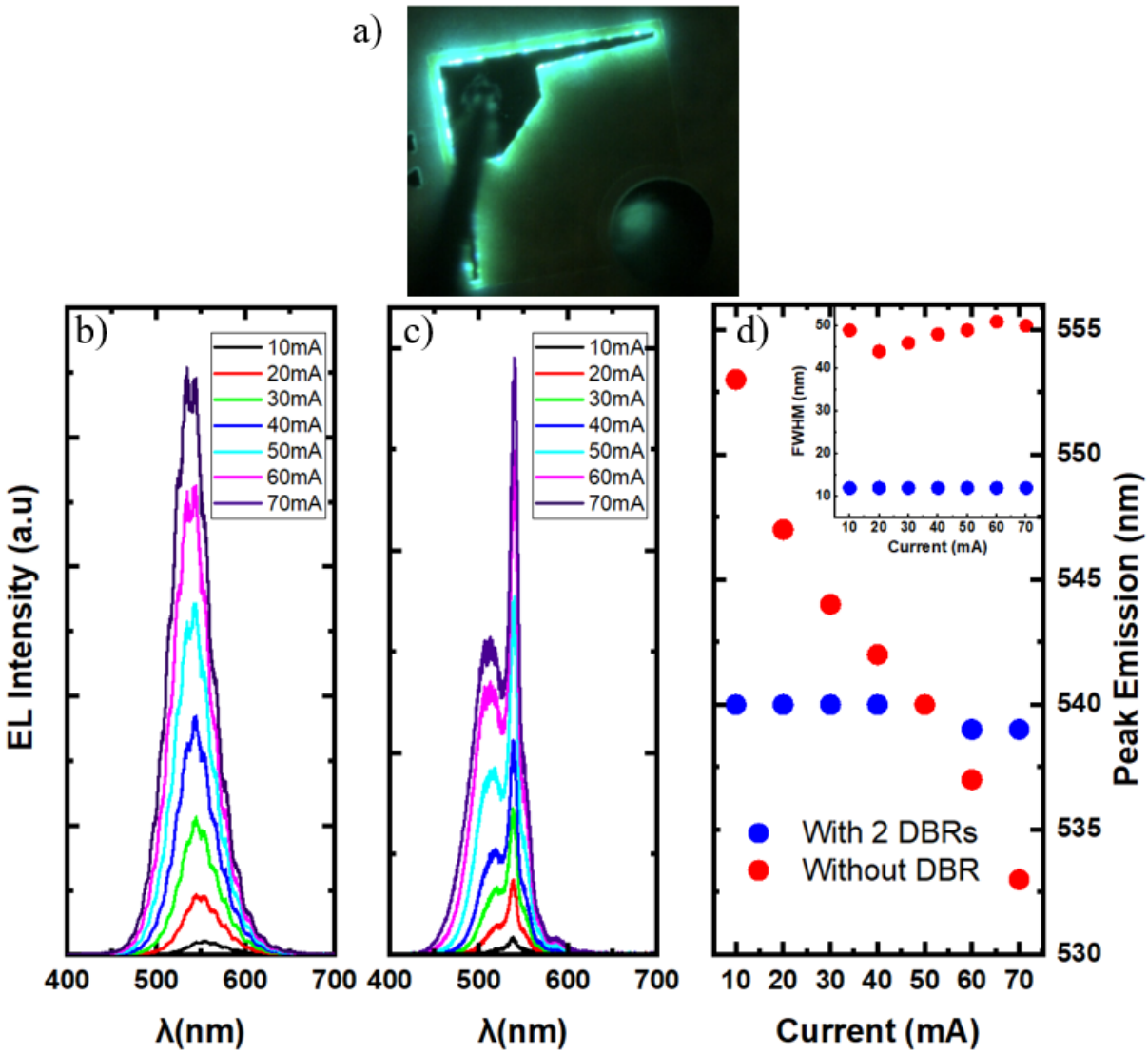

Figure 80: a) Emission image of a sample with top-bottom DBR under 20mA. b) Emission spectra of the sample without DBR. c) Emission spectra of the sample with top-bottom DBR. d) Peak emission and FWHM (inset) as a function of injected current.

In order to study the existence of modes and achieve lasing, more devices were fabricated using another piece from the same wafer. Figure 81a) illustrates the EL spectra of a second fabrication run, where the issue with ITO spreading layer was not yet solved. However, once again a narrow emission peak appeared, in this case at 530 nm. Furthermore, another two possible modes appeared at 495 nm and 577 nm. The FWHM of the sample with top-bottom DBR was as narrow as

5.5 nm at 25 mA. However, as the current increased, the emission became broader, at 65 mA a reduction in the intensity is observable, this is assumed to be related with heating issues due to the dielectric DBR. Figure 81b) shows the normalised reflectance of the top-bottom DBR emitting device and its emission spectra at 25mA. The reflectance shows cavity mode dips that spectrally match with the emission of the device, which is one of the fingerprints of microcavity effects [24-26].

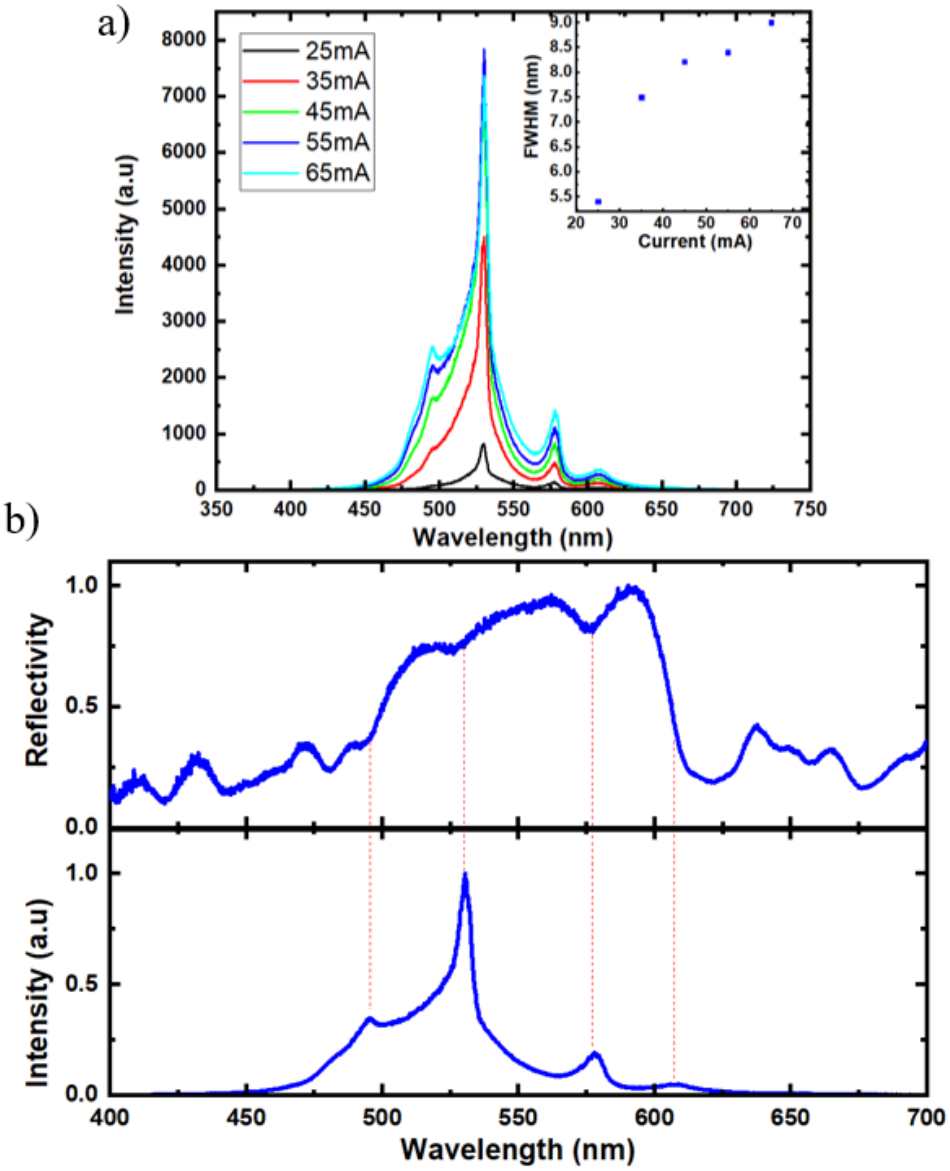

Figure 81: a) EL spectra of a top-bottom DBR device. Inset shows the FWHM of the 530nm peak. b) Normalised reflectance and emitted spectra at 25mA.

Although the development of the bottom DBR and the device fabrication has been carried out under the same conditions, the dominant mode emission of the reported devices varies in a range of 10nm. As described in Chapter 2, the mode wavelength is mainly determined by the cavity length and its refractive index. Aiming for a better understanding of this mode shifting behaviour, 3D-FDTD

simulations have been carried out to observe the effect of the top DBR into the spectral mode position. Thus, the structure described in Section 6.2.1 has been used. Nevertheless, in this case the centre wavelength of the top DBR has been varied from 500 nm to 580 nm. Figure 82, illustrates the result obtained from the simulation, where a maximum mode detuning of 6 nm is obtained when the top DBR is centred at 580 nm.

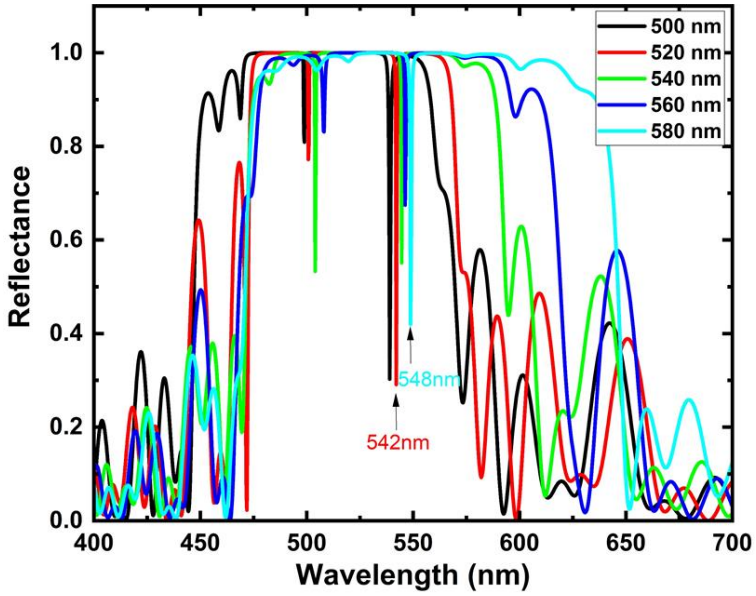

Figure 82: Simulated reflectance of the microcavity changing the top DBR centre wavelength.

The origin of the shift was believed to be due to a detuning between the centre of the top and the bottom DBR. Although the deposition conditions of the dielectric layers were slightly unstable in our PECVD (deposition rate oscillates a 2%), this was not enough to produce such a shift. Figure 83a) illustrates the cross-section view SEM image of the microemitter with porous and dielectric DBR. As can be seen, the top DBR is deposited non-uniformly, creating a wavy deposited layer, due to the non-flat surface of the microemitter. The formation of InGaN products on top of the SiO_2 during the overgrowth process would lead into DBR un-uniformity, which can lead into different effective cavity lengths and finally shift the mode wavelength. To validate this statement, reference DBRs were deposited in a Silicon and on an overgrowth microemitter sample. The reflectivity of 12 pairs of SiO_2-SiN deposited DBR on the micro-emitter sample is presented in Figure 83b). It can be seen that the peak reflectivity is lower than expected. Moreover, the centre wavelength is slightly shifted towards. In order to compensate the irregular non-flatness of the surface, another ten pairs were deposited. Thus, a near 80% peak reflectance was achieved at 520 nm.

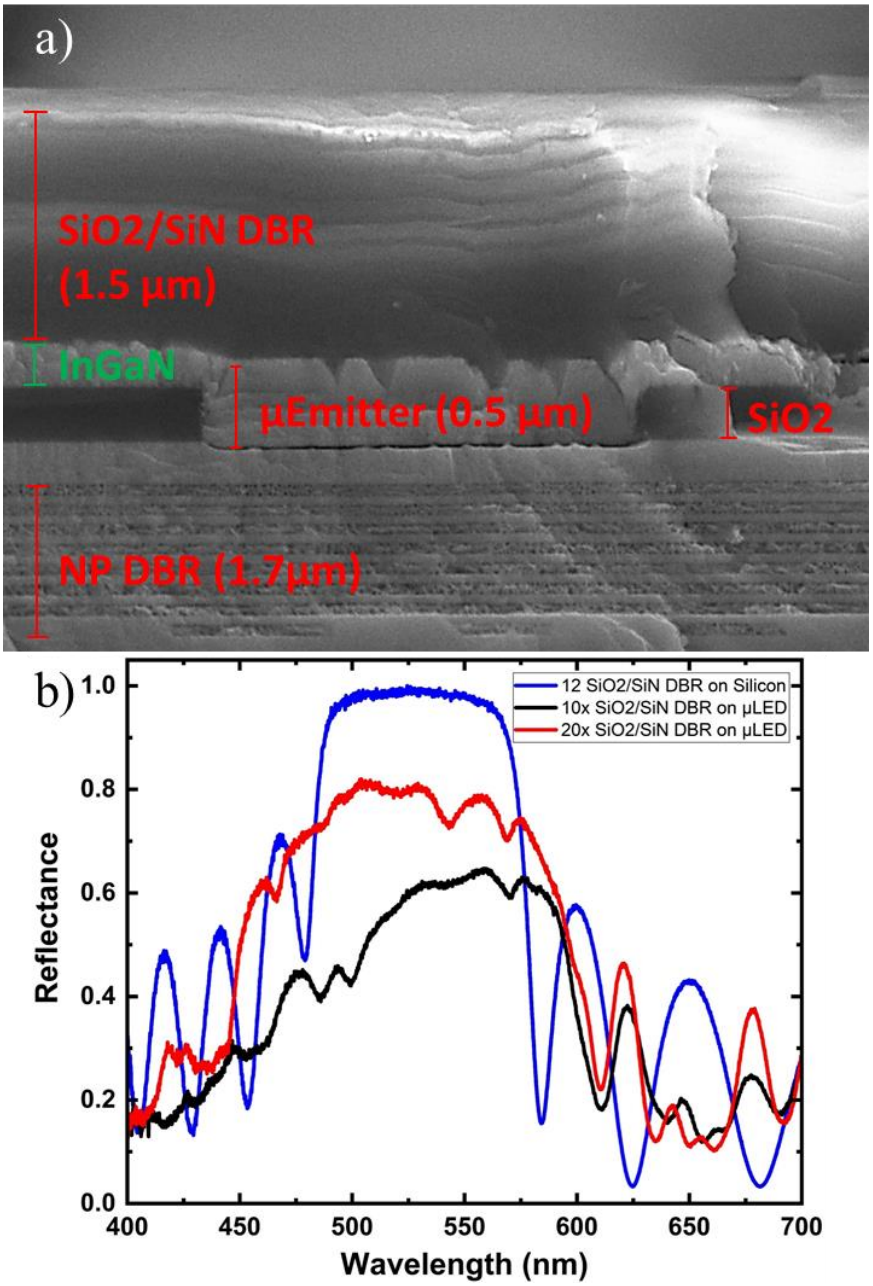

Figure 83: Cross section SEM image of the microemitter with top and bottom DBR. b) Effect of the surface on the DBR reflectance.

Another fabrication run was carried out. This time, the top DBR was deposited using ICPCVD, where the chamber temperature is kept at 100 ° C. However, for this last sample 20 pairs of dielectric DBR were deposited to compensate any uniformity on the sample surface. Figure 84a) illustrates the 80x80um mesa under 20mA injection current, where a non-damaged Ni/Au acts as a current spreading layer. Figure 84b) shows the I-V characteristics of the device, the series resistance value is roughly the same as the one presented in the previous section. The slightly increase is attributed to the dielectric heat dissipation issues. The emission spectra can be seen in Figure 84c). At low injection current, the main peak is located at 528 nm. After increasing the current to 9mA, the peak becomes

much sharper, with a FWHM of 1 nm. Unfortunately, there is a broadness in the emission and wavelength shifting that can be associated with heating effects on the device under testing. Stimulated emission has not been probed.

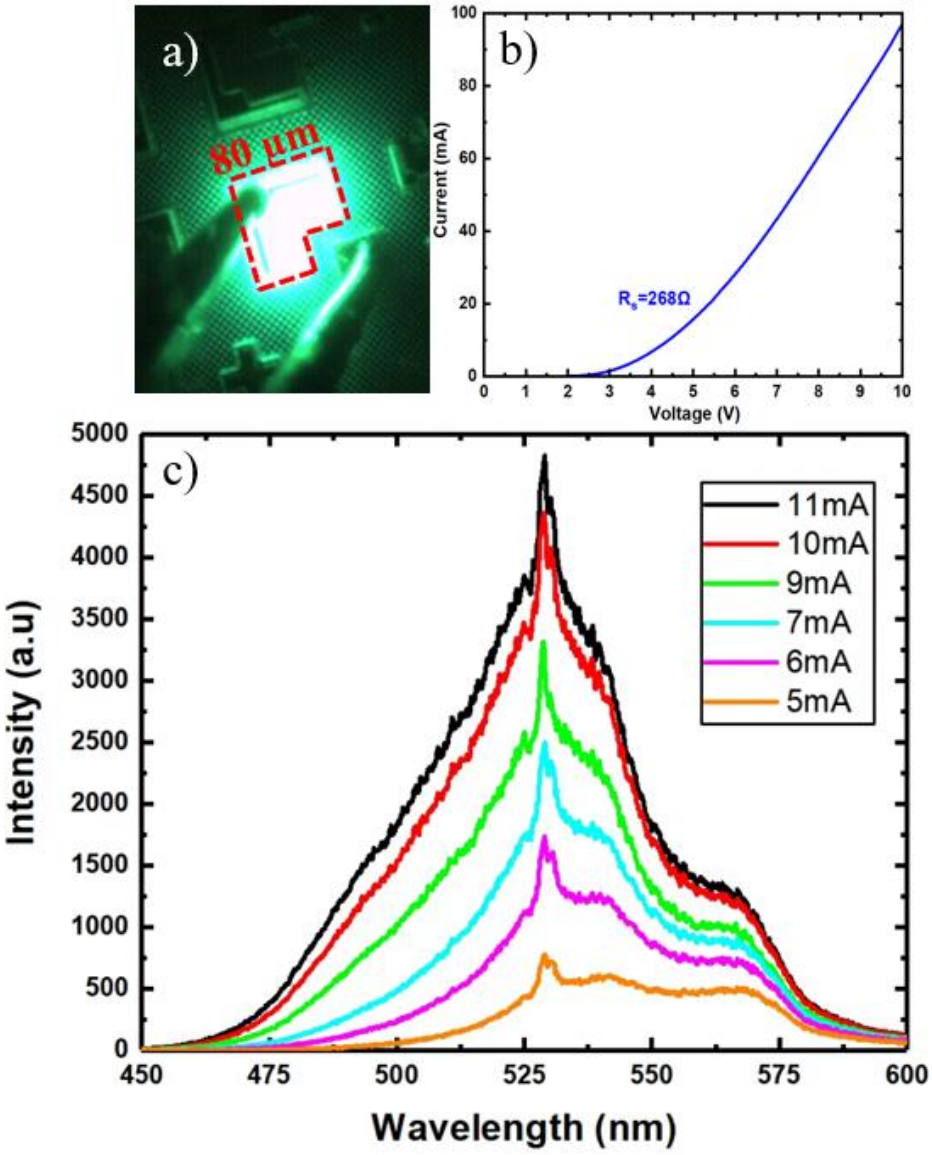

Figure 84: a) Emission image of an 80x80 µm microemitter at 20mA. b) I-V characteristics. c) EL spectra under different current injection.

6.4 Conclusion

In conclusion, this chapter presented a novel approach towards micro-scale III-nitride VCSELs. A great improvement in the EC is demonstrated, leading to a reduction of the series resistance by a factor of two. Additionally, a uniform porosity in the NP-based DBR is achieved, addressing one of the major challenges in NP based devices at present. Although stimulated emission behaviour has not been confirmed yet, microcavity effects have been observed under either optical or electrical pumping. The results show the high potential of this novel-patented approach.

6.5 References

[1] T. Someya, et al., Lasing emission from an In0.1Ga0.9N vertical cavity surface emitting laser. *Japanese Journal of Applied physics*, 37:L1424-L1426, 1998.

[2] A.N. Al-Omari and L. Kevin, VCSELs With a Self-Aligned Contact and Copper-Plated Heatsink. *IEEE Photonics Technology letters*, 17:9, 2005.

[3] A.N. Al-Omari, et al., Improved performance of top-emitting oxide-confined polyimide-planarized 980 nm VCSELs with copper-plated heat sinks. *Journal of Physics D: Applied Physics*, 45:50, 2012.

[4] T.C. Lu, et al., CW lasing of current injection blue GaN-based vertical cavity surface emitting laser. *Applied Physics Letters*, 92:141102, 2008.

[5] T. C. Lu, et al., Continuous wave operation of current injected GaN vertical cavity surface emitting lasers at room temperature. *Applied Physics Letters*, 97:071114, 2010.

[6] Y. Higuchi, et al., Room-temperature CW lasing of a GaN based Vertical-Cavity Surface-Emitting Laser by current injection. *Applied Physics Express*, 1:121102, 2008.

[7] D. Kasahara, et al., Demonstration of blue and green GaN-based Vertical-Cavity Surface-Emitting Lasers by current injection at room temperature. *Applied Physics Express*, 4:072103, 2011.

[8] T. Hamaguchi, et al., Room-temperature continuous-wave operation of green vertical-cavity surface-emitting lasers with a curved mirror fabricated on {20−21} semi-polar GaN. *Applied Physics Express*, 13:041002, 2020.

[9] L.E. Cai, et al., Blue-green optically pumped GaN-based vertical cavity surface emitting laser. *Electronics Letters*, 44(16):972-974, 2008.

[10] Y. Mei, et al., Quantum dot vertical-cavity surface-emitting lasers covering the 'green gap'. *Light: Science & Applications*, 6, 2017.

[11] S.-M. Lee, et al., Optically pumped GaN vertical cavity surface emitting laser with high index-contrast nanoporous distributed Bragg reflector. *Optics Express*, 23:11023-11030, 2015.

[12] C. Zhang, et al., A resonant-cavity blue–violet light-emitting diode with conductive nanoporous distributed Bragg reflector. *Physica Status Solidi (a)*, 214:8, 2017.

[13] S. M. Mishkat-Ul-Masabih, et al., Polarization-pinned emission of a continuous-wave optically pumped nonpolar GaN-based VCSEL using nanoporous distributed Bragg reflectors. *Optics Express*, 27:9495-9501, 2019.

[14] C . J. Wang, et al., InGaN Resonant-Cavity Light-Emitting Diodes with porous and dielectric reflectors. *Applied Science*, 11:8, 2021.

[15] R. T. ElAfandy, et al., Room-temperature operation of c-plane GaN vertical cavity surface emitting laser on conductive nanoporous distributed Bragg reflector. *Applied Physics Letters*, 117:1, 2020.

[16] E. Hashemi, et al., Analysis of structurally sensitive loss in GaN-based VCSEL cavities and its effect on modal discrimination. *Optics Express*, 22:1:411-416, 2014.

[17] R. Lida, et al., Aperture diameter dependences in GaN-based vertical-cavity surface-emitting lasers with nano-height cylindrical waveguide formed by BCl3 dry etching. *Applied Physics Express*, 14:1, 2020.

[18] L. Gao, F. Lemarchand and M. Lequime, Refractive index determination of SiO2 layer in the UV/Vis/NIR range: spectrophotometric reverse engineering on single and bi-layer designs, *Journal of European Optical Society Rapid Publications*, 8: 13010, 2013.

[19] P.H. Griffin, et al., The relationship between the three-dimensional structure of porous GaN distributed Bragg reflectors and their birefringence. *Journal of Applied physics*, 127: 193101, 2020.

[20] T. Zhu, et al., Wafer-scale fabrication of non-polar mesoporous GaN Distributed Bragg Reflectors via electrochemical porosification. *Scientific Reports*, 7:45344, 2017.

[21] P.H. Griffin and R.A. Oliver, Porous nitride semiconductors reviewed. *Journal of physics D: Applied Physics*, 53:38, 2018.

[22] X. Lu, et al., Performance-enhanced 365 nm UV LEDs with electrochemically etched nanoporous AlGaN Distributed Bragg Reflectors. *Nanomaterials*, 9:6:862, 2019.

[23] Does counter electrode (CE) size matter? https://metrohm.blog/2021/08/16/size-matters-ce-we/ [Accessed 1th December 2022]

[24] H. Megahd, D. Comoretto, P. Lova, Planar microcavities: Materials and processing for light control. *Optical Materials: X*, 13, 2022.

[25] T-C. Lu, et al., Development of GaN-based Vertical-Cavity Surface-Emitting Lasers. *IEEE Journal of Selected Topics in Quantum Electronics*, 15 (3):850-860, 2009.

[26] G.S. Huang, et al., Fabrication of microcavity Light-Emitting Diodes using highly reflective AlN–GaN and Ta2O5–SiO2 Distributed Bragg Mirrors. *IEEE Photonics Technology Letters*, 19:13, 2007.

Chapter 7: Enabling high confinement factor edge emitting lasers by using a nanoporous GaN cladding layer

This chapter presents a study of the enhancement of the optical confinement factor due to nanoporous cladding layers. Thus, simulations based in Finite Difference Eigenmode (FDE) are presented. Furthermore, experimental formation of porous conductive cladding layers has also been demonstrated.

7.1 Introduction

The progression in III-nitride edge emitting lasers have been tremendous over the past years, high brightness and high efficiency LDs have raised to lead potential application such as lighting, laser display and information storage [1-3]. The development of a GaN LD on standard c-plane is challenged due to the intrinsically nature of the polar GaN wurtzite crystal structure, particularly for emissions longer than 500nm. Over the past decade, LDs grown on alternative crystal orientations with reduced or no polarisations, referred as semipolar or non-polar have been presented [5]. Although the benefits over polar GaN seem clear, the use of semipolar or non-polar present challenges related to cost, crystal growth and device design [8].

As explained in Chapter 2, a LD requires an optical cavity in order to provide feedback through the amplifying medium, leading to stimulated emission under certain conditions. The device performance is greatly affected by the cavity design and its waveguide behaviour. Edge emitting lasers normally rely separate confinement heterostructure (SCH), where the transverse optical mode is confined in the core region (active region) inserted between two cladding layers [9-14]. The core layer is formed by MQWs to facilitate radiative recombination. Population inversion is reached when the injected carrier density exceeds the transparent level. The optical gain defines the increase of coherent photons. Thus, lasing condition is achieved when the optical gain associated with a particular waveguide mode (G_{Modal}) exceeds the optical losses, given by:

$$G_{Modal} = \Gamma g_{th} = \alpha_m + \alpha_i \quad (34)$$

Where g_{th} is the material gain of the active region, Γ is the optical confinement factor, α_m and α_i correspond to the distributed mirror losses and internal losses (scattering and absorption) [15]. The optical confinement factor presents the

overlapping between the transverse optical mode in the gain region and the rest of the waveguide, expressed as:

$$\Gamma = \frac{\int_{MQW} E(z)^2 dz}{\int_{whole\ waveguide} E(z)^2 dz} \tag{35}$$

A LD with a high Γ implies that majority of coherent photons are capable of interacting with the injected carriers. The threshold current density in an LD can be expressed as:

$$Jth = \frac{qdA_{LD}}{n_{inj}} \left[An_{tr} exp\left(\frac{\alpha_m + \alpha_i}{\Gamma g_o}\right) + Bn_{tr}{}^2 exp\left(2\frac{\alpha_m + \alpha_i}{\Gamma g_o}\right) + Cn_{tr}{}^2 exp\left(3\frac{\alpha_m + \alpha_i}{\Gamma g_o}\right)\right] \tag{36}$$

Where the terms in the brackets are related to the Shockly read hall, radiative and Auger recombination coefficients, A_{LD} is the cross section of the LD, d is the thickness of the active region, n_{tr} is the transparency carrier density, g_o is the empirical gain coefficient of the active region [16]. Therefore, to achieve low threshold lasers the optical confinement must be maximised. The confinement factor is strongly affected by the waveguide design and the refractive index difference (Δn) between the core and cladding layers.

Cladding layers require a low refractive index to confine the electric field into the active region. Traditionally, III-nitride EELs use AlGaN material as a bottom cladding layer. However, the refractive index difference between GaN-AlGaN is relatively small (<0.05), leading to a low optical confinement factor ~3% [15]. The AlGaN refractive index can be lowered as the Al content increases, at expenses of creating mismatched stress, for example an increase of 10% Al leads to a reduction of the refractive index by ~0.04, with a correlated tensile stress of 1GPa [15]. Thus, the growth of AlGaN cladding layers with high Al content present a challenge itself. The increase of Al% leads into a higher tensile strain and eventually dislocations and cracking. Alternatively, the use of nanoporous GaN as a cladding layer could lead into higher index contrast difference.

7.2 Simulation of confinement factor by *MODE solutions*

The confinement factor enhancement due to the porous cladding layer has been studied through 2D Finite Difference Eigenmode simulations. *Ansys Lumerical FDE* solves the full vectorial Maxwell equations at a specified frequency based on materials and geometries entered by the user.

The potential of ITO to replace conventional p-AlGaN cladding layer have been studied by other authors, to achieve a high-power green LD [17-21], due to its low refractive index and lower absorption losses than conventional p-AlGaN cladding layers.

In order to effectively model the waveguide, the refractive index of GaN and ITO layers has been obtained from spectroscopic scans. Figure 85, illustrates the spectroscopic scan data of a thick n-GaN and ITO on sapphire and its agreement with the model, where MSE<20 are obtained. Thus, refractive indices values at 530nm are estimated to be: n_{GaN}=2.39 n_{ITO}=2.01.

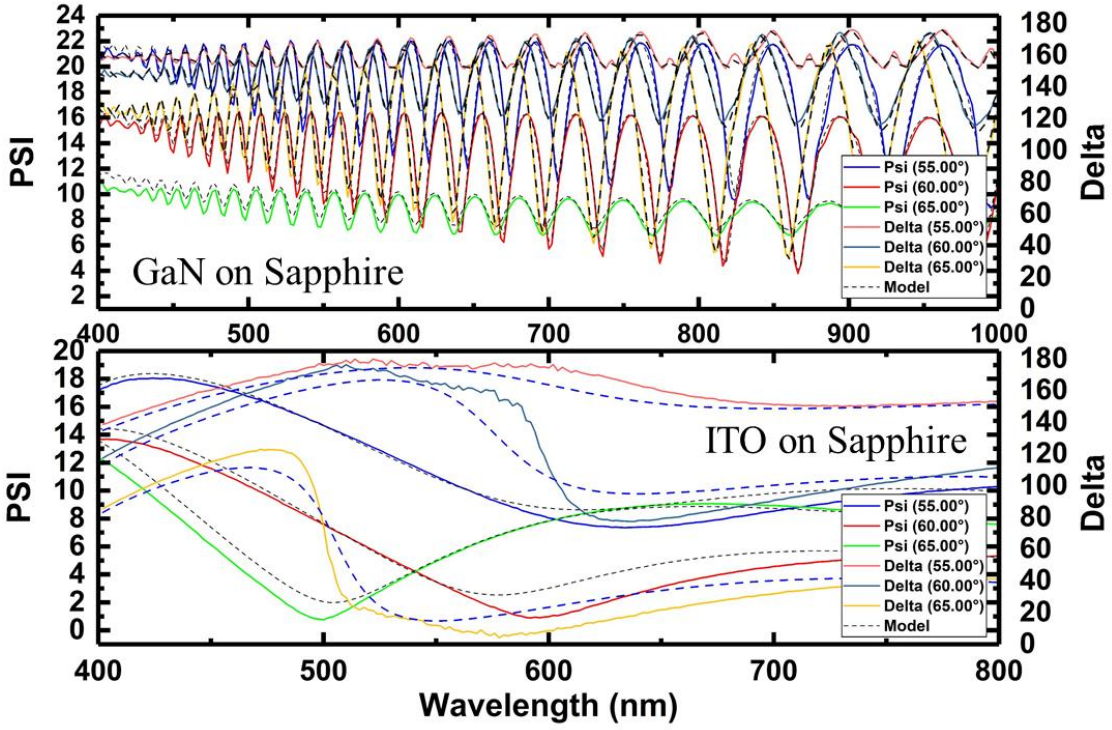

Figure 85: Spectroscopic scan GaN (top) and ITO (bottom) on sapphire.

2D-FDE simulations were carried out to demonstrate the possible enhancement of porous cladding layers. Figure 86 illustrates the 2D schematic of the simulated structures. Table 6 illustrates the thickness and refractive index of each layer used in the simulations.

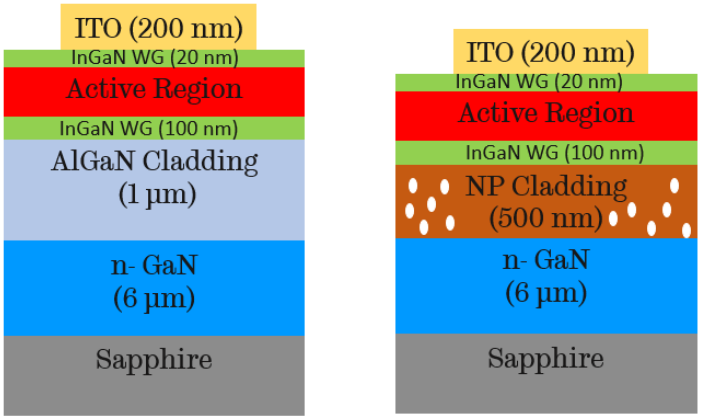

Figure 86: Schematic diagram of the conventional ridge laser (LHS) and nanoporous laser (RHS).

Table 6: Optical parameters used in FDE simulations (530nm). Adapted with permission from [21].

Layer	Thickness (nm)	Refractive Index	Absorption Coefficient (cm^{-1})
n-GaN	1000	2.39*	10
$Al_{0.15}GaN$ / NP-layer	1000/500	2.39/1.9	10
InGaN WG	70	2.43	10
5x $In_{0.27}GaN$ MQW	3	2.69	-
GaN Barrier	12	2.42	10
InGaN WG	20/100	2.43	10
$Al_{0.2}GaN$ EBL	20	2.37	10
ITO	150	2.01*	1920

A narrow 2 µm ridge was defined in the simulation. The thickness of the waveguide layers has been optimised to achieve the maximum overlap with the optical mode. Figure 87a), illustrates the solved fundamental mode of the device using porous GaN and $Al_{0.15}GaN$, the colour scale bar represents the maximum intensity of the field. The porous layer lead into a noticeable enhancement of the confinement in the active region. Figure 87b), illustrates a 1D representation of the modal field and the refractive index, where is possible to see that the part of the field leak into the substrate in the AlGaN based device.

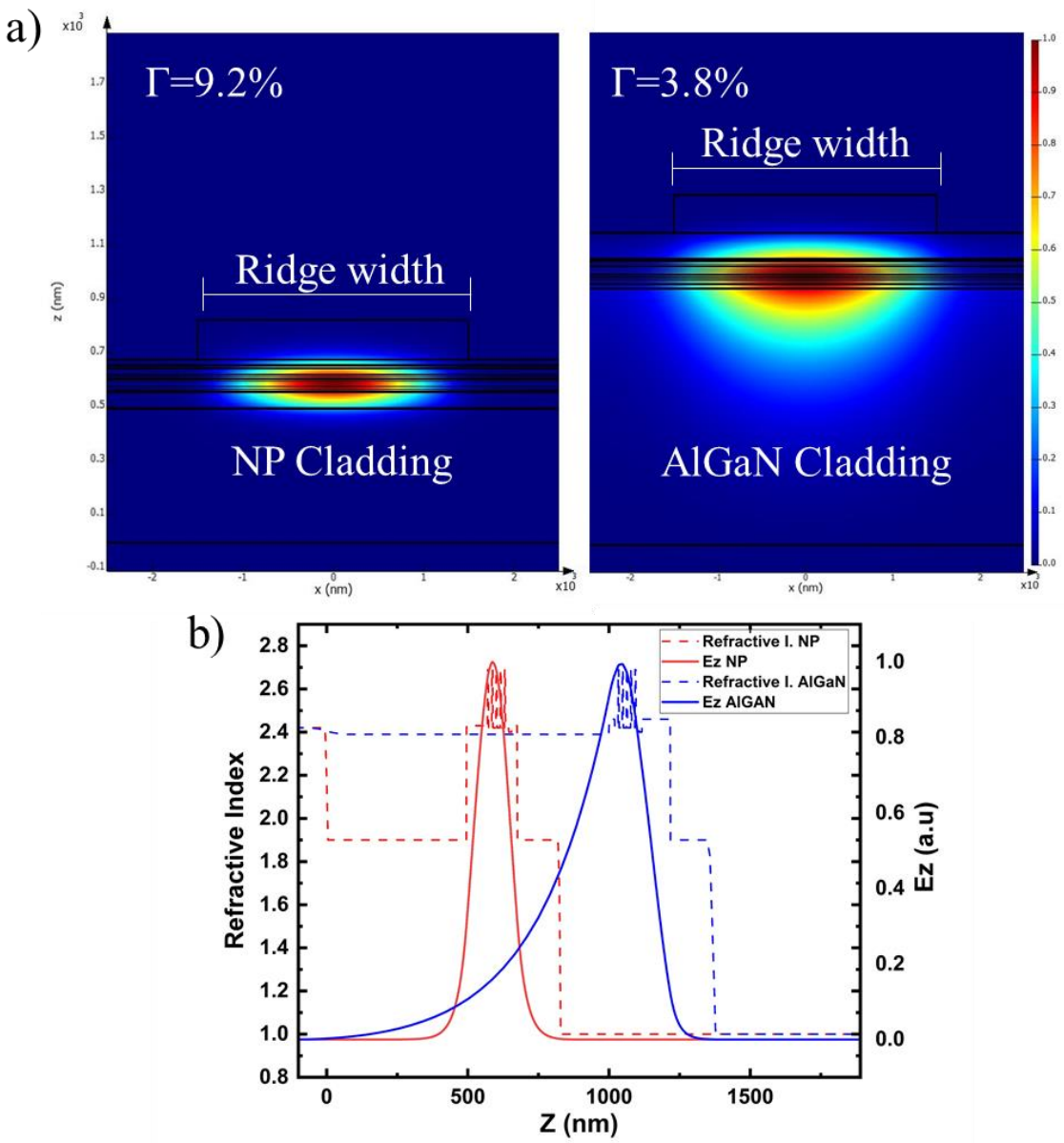

Figure 87:a) 2D Modal field distribution XZ plane using porous (left) and AlGaN (right) cladding layers. b) 1-D distribution of field and refractive index.

7.3 Nanoporous Cladding layer formed by EC etching

After demonstrating the potential of porous cladding layers through simulations, experimental EC etchings were carried out. Aiming for an electrical injected device, the number of MQWs was reduced to 2. Thus, achieving a uniform injection in the active region, as explained in Chapter 4.

A 2” wafer was grown using MOVPE. First, a thick 6 µm GaN was grown on sapphire substrate, after checking its crystal quality and surface conditions, a second LD growth was carried out. The growth replicated the thickness used in the previous section. Thus, the LD structure is formed by a 500 nm n++$Al_{0.05}Ga_{0.95}N$ layer, a 20nm and 100 nm bottom-top InGaN/GaN superlattice

waveguides, standard active region based on 2 x InGaN/GaN (3.2 nm/10 nm), a 20 nm $Al_{0.15}Ga_{0.85}N$ as an electron blocking layer and 100 nm p-GaN. Figure 88, illustrates the PL measured with at CW 375nm at room temperature, the centre emission wavelength is around 510nm with 25nm FWHM.

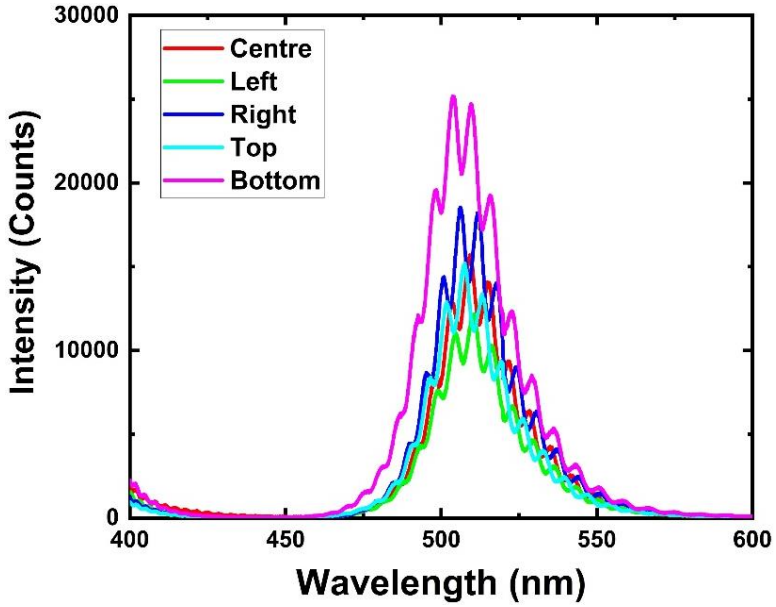

Figure 88: Photoluminesce of the 2QW LD wafer.

The lateral etching approach described in the previous chapter was used to achieve a uniform porous cladding layer. Thus, a 500 nm SiO_2 layer was deposited on top of the LD structure, trenches were defined and etched down by means of ICP, exposing the n++AlGaN cladding layer. The EC took place with a 0.3M HNO_3 electrolyte, the bias voltage was tuned from 6V to 8V. Figure 89a) illustrates the cross-section SEM image of the sample etched under 6 and 8V. Figure 89b), illustrates the spectroscopic scan data of the 8V sample. For the porous layers a model based on effective medium approximation (EMA) was built, where the porous were modelled as a void. The thickness of the layer is well modelled; however, the refractive index indicates a low porosity of 20%, giving a refractive index of 2.1. As the MSE ~ 80 and the modelling was complex, the porosity of the cladding layer was estimated from its cross-section image by using a binary conversion, as shown in chapter 6.

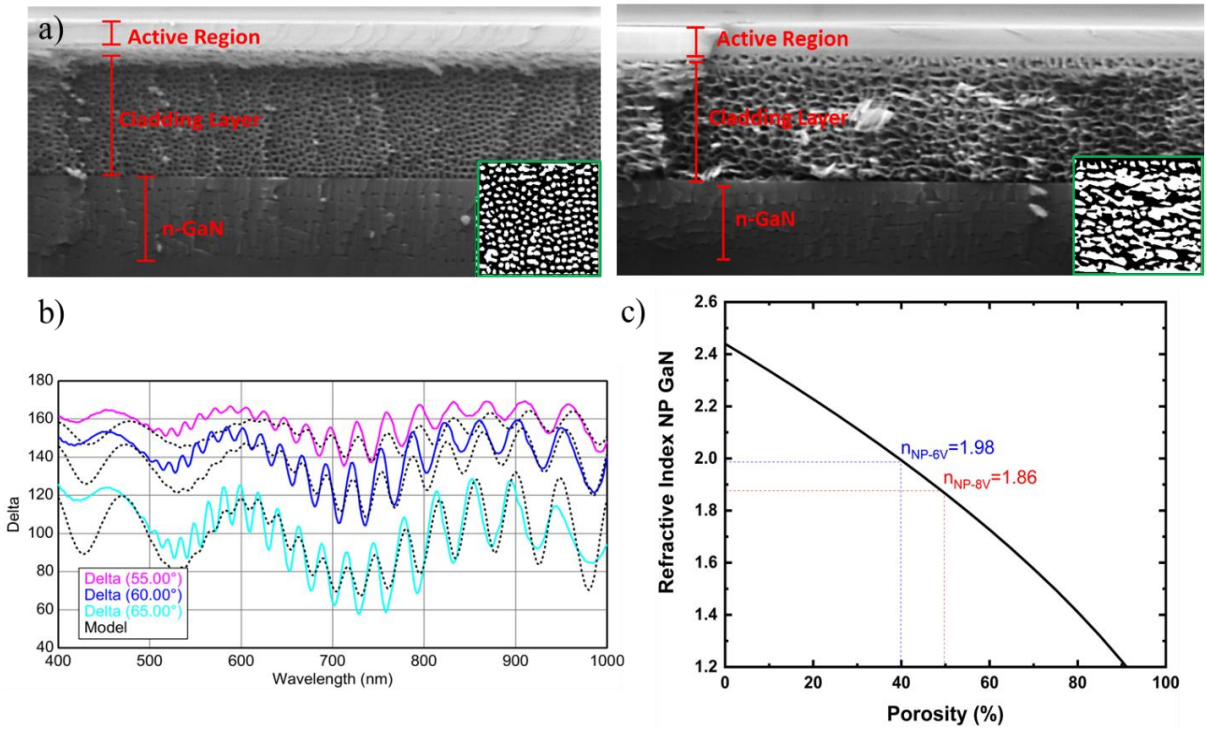

Figure 89: a) Cross section SEM image of a sample etched under 6V (left) and 8V (right). Insets show the binary image used for porosity calculation. b) Spectroscopic scan of the 8V sample. c) Refractive index based on VAT and the binary image obtained from SEM.

Once the etching conditions were established, standard laser fabrication was carried out in another piece of the wafer. First, the porosification took place under a constant bias of 6.5 V. Then, the sample was p-activated in N_2 for 15 min at 700 °C. In order to facilitate the fabrication, the ridge width was 5 µm instead of 2 µm. It was found that in such a narrow structure, which is close to the limit of our mask aligner, the patterning step is crucial in order to achieve a good ridge etch profile. Figure 90, illustrates the cross-section SEM image using a standard spin-patterning-dry etching and the optimised conditions. Thus, a first exposure removes the edge bead of the sample to improve the contact between the mask and the PR, then a second exposure pattern the ridges. After developing the PR the sample undertook a 30 seconds O_2 ashing process with a flow rate and constant power of 250 sccm and 150 W, followed by a hard mask bake at 100 °C for 1 minute. Later the ridge was etched down to the top waveguide structure, with a total etching depth of 200 nm. After that, the mesa was etched to reach the n-GaN and n-metal contact was deposited, using a Ti/Al/Ti/Au alloy. Subsequently, the contact was annealed in a N_2 ambient at 700°C for 1 minute, and a 350 nm SiO_2 passivation layer was deposited using PECVD. The p-contact window was opened in the ridge by means of HF, after that 200 nm of ITO were deposited and annealed using the same conditions described previously (Chapter 5). Similarly, the n-contact window was opened by means of ICP. Finally, Ti/Au bondpads were deposited to allow electrical injection.

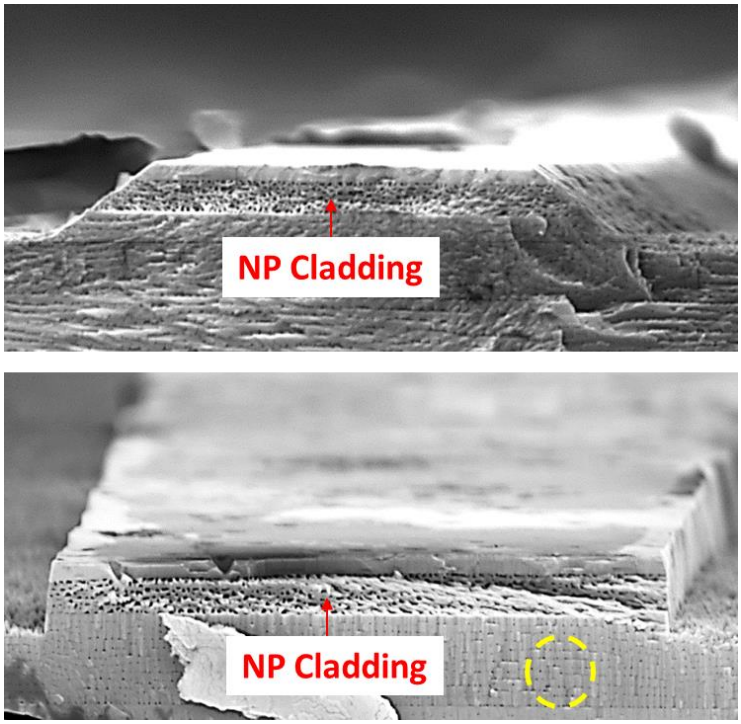

Figure 90: Cross section view SEM of the porous ridge with not optimised (top) and optimised (bottom) conditions. Yellow dashed line illustrates parasitic etching of the n-GaN layer.

7.4 Results and discussion

7.4.1 Electrical characteristics

The fabricated devices were cleaved into 1cm long pieces. However, the difficulties on polishing and cleaving the GaN on sapphire lead into bad facet formation. Although the back side of the substrate was polished with grinding papers, reducing its thickness from 460 µm to less than 100 µm, no clear cleavage was achieved. Figure 91 illustrates the cross-section SEM image of the nanoporous ridge laser after fabrication, where it is possible to observe that the passivation layer covers the ridge effectively.

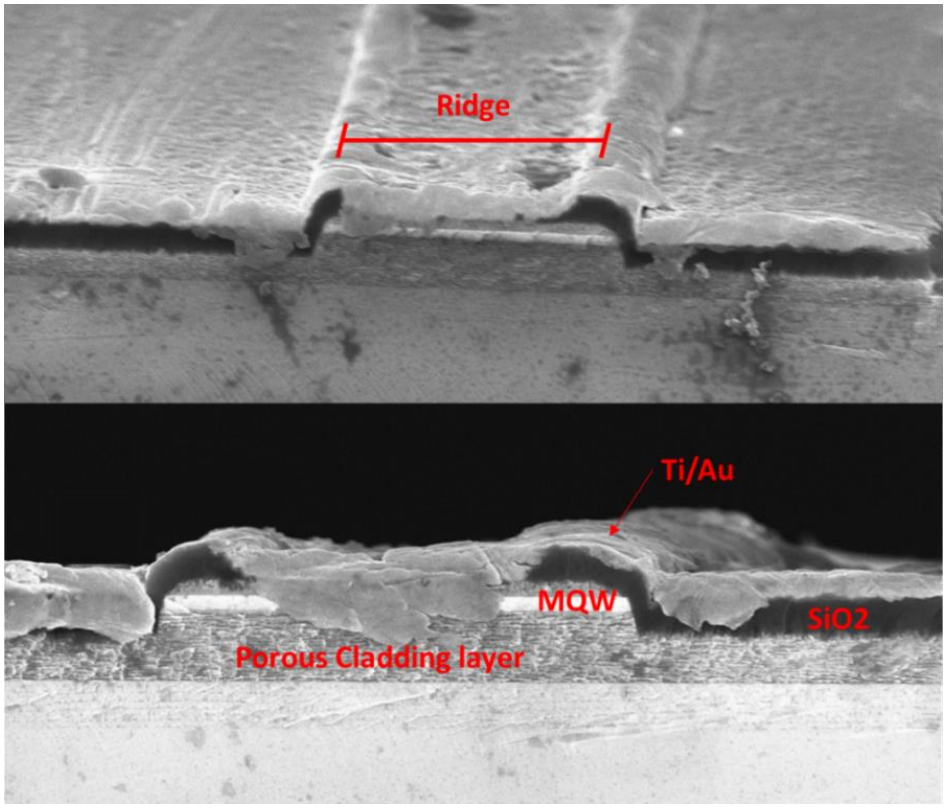

Figure 91: SEM image at 30° angle (top) and cross section view (bottom).

The sample was tested under CW regime without coated facets. Figure 92a) shows the emission of the device at 20mA, where the light seems to be effectively confined into a waveguide mode. Electroluminescence spectra shown in Figure 92b), were taken using a multi-mode fibre placed at the edge of the emitting facet and a *Flame UV-MIS* spectrometer. Narrowing was not observed under increasing current injection either an abrupt change on integrated intensity, probably the bad facet formation led to the inexistence of the cavity. The spectra show fringes with a FSR of 8 nm, which agrees well with vertical mode spacing using $FSR = \frac{\lambda^2}{2Ln}$, with λ=510 nm, L =6500 nm and n = 2.44. The dashed line illustrates the QCSE. The inset in Figure 92b) shows the current voltage characteristics of the porous device.

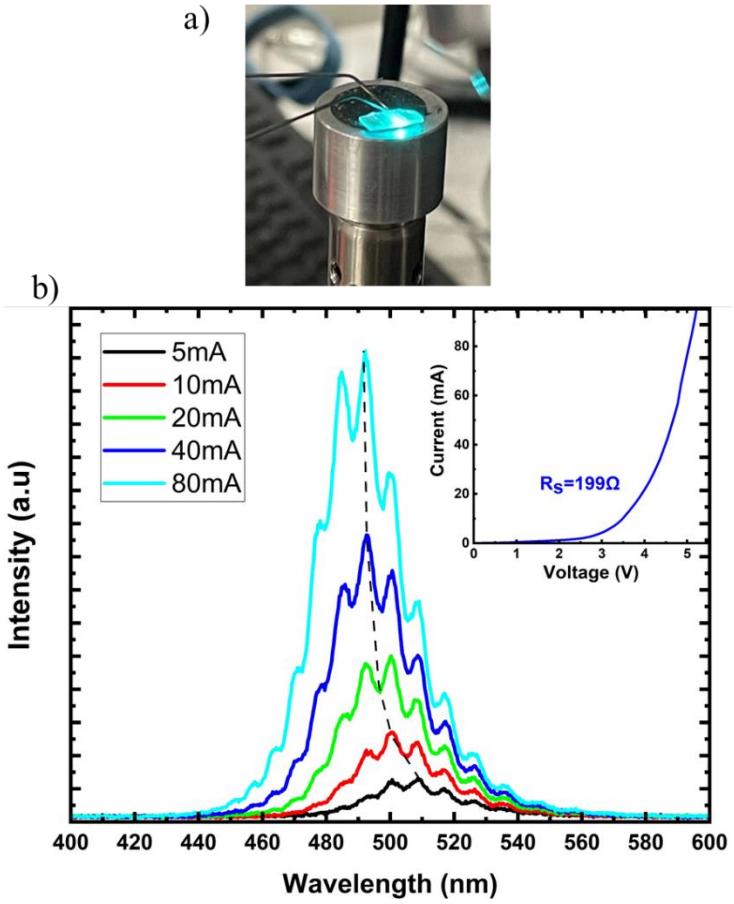

Figure 92: a) Emission image of the ridge sample at 20mA. B) EL spectra under CW injection current. Inset illustrates the I-V characteristics.

7.5 Conclusion

In summary, this chapter presented the application of porous cladding layers in edge emitting lasers. The enhancement of the confinement factor due to the porous layer has been demonstrated through simulations. Cladding layers were fabricated by means of EC, a good agreement has been achieved between the assumed refractive index (simulations) and the measurements. Electrically injected ridge lasers were fabricated, effectively injection through the porous layer is achieved. However, no stimulated emission was obtained, due to the difficulties related with cavity formation. Optimisation is on-going in order to achieve lasing.

7.6 References

[1] S. Nakamura, The roles of structural imperfections in InGaN-based blue light-emitting diodes and laser diodes. *Science*, 281: 956–961, 1998.

[2] F. A. Ponce and D. P. Bour, Nitride-based semiconductors for blue and green light-emitting devices. *Nature*, 386: 351–359, 1997.

[3] T. Miyoshi, et al., 510–515 nm InGaN-based green laser diodes on c-plane GaN substrate. *Applied Physics Express*, 2:062201, 2009.

[4] U. Strauss, et al., GaInN laser diodes from 440 to 530 nm: a performance study on single mode and multi-mode R&D designs. *Proceedings SPIE*, 10123: 101230A, 2017.

[5] S. Takagi, et al., High-power (over 100 mW) green laser diodes on semipolar {2021} GaN substrates operating at wavelengths beyond 530 nm. *Applied Physics Express*, 5: 082102, 2012.

[6] S. P. DenBaars, et al., Development of gallium-nitride-based light-emitting diodes (LEDs) and laser diodes for energy-efficient lighting and displays. *Acta Materialia*, 61: 945–951, 2013.

[7] J. J. Wierer, J. Y. Tsao, and D. S. Sizov, Comparison between blue lasers and light-emitting diodes for future solid-state lighting. *Laser Photonics Review*, 7:963–993, 2013.

[8] H. Li, et al., Development of efficient semipolar InGaN long wavelength light-emitting diodes and blue laser diodes grown on a high quality semipolar GaN/sapphire template. *Journal of Physics Photonics*, 2 :031003, 2020.

[9] G. H. B. Thompson, P. Kirkby, (GaAl)As lasers with a heterostructure for optical confinement and additional heterojunctions for extreme carrier confinement. *IEEE Journal Quantum Electronics*, 9:311– 318, 1973.

[10] H. C. Casey, et al., Heterostructure laser with separate optical and carrier confinement. *Journal of Applied Physics*, 45:322– 333, 1974.

[11] G. H. B. Thompson, et al., Narrow-beam five-layer (GaAl)As/GaAs heterostructure lasers with low threshold and high peak power. *Journal Applied Physics*, 47, 1501– 1514, 1976.

[12] W. T. Tsang, Extremely low threshold (AlGa)As graded-index waveguide Separate-Confinement Heterostructure lasers grown by Molecular Beam Epitaxy. *Applied Physics Letters*, 40, 217– 219, 1982.

[13] S. Nakamura, et al., InGaN-Based Multi-Quantum-Well-Structure Laser Diodes. *Japanese Journal of Applied Physics*, 35: L74– L76, 1996.

[14] I. Akasaki, et al., Shortest wavelength semiconductor laser diode. *Electronics Letters*, 32: 1105, 1996.

[15] G. yuan, et al., Optical engineering of modal gain in a III-Nitride laser with Nanoporous GaN. *ACS Photonics*, 3:9:1604-1610, 2016.

[16] J. J.Wierer, J. Y.Tsao, D. S. Sizov, Comparison between blue lasers and Light-Emitting Diodes for future solid-state lighting. *Laser Photonics Reviews*, 7:963– 993, 2013,

[17] L.Hu, High-power hybrid GaN-based green laser diodes with ITO cladding layer. *Photonics Research*, 8:3:279-285, 2020.

[18] D. Bour, et al., Silver-clad nitride semiconductor laser diode. *Applied Physics Letters*, 94:4:041124, 2009.

[19] M. Hardy, et al., Indium-tin-oxide clad blue and true green semipolar InGaN/GaN laser diodes. *Applied Physics Letters*, 103:8:081103, 2013.

[20] A. Myzaferi, et al., Transparent conducting oxide clad limited area epitaxy semipolar III-nitride laser diodes. *Applied Physics Letters*, 6:109, 2016.

[21] M. Cuk, et al., ITO layer as an optical confinement for nitride edge-emitting lasers. *Bulletin of The Polish Academy of Sciences-technical Sciences*, 68:1, 2020.

Chapter 8: Conclusions and future work

This thesis presents the development and optimisation of III-nitride microemitters with microcavity effects. The potential of porous GaN to form microcavities can enhance the optical performance of devices, leading to the development of future advanced III-nitride optoelectronics.

8.1.1 Study of whispering gallery modes (WGMs) in III-nitrides by FDTD

In summary, the current development, advantages, limitations and potential applications of microdisk lasers are presented. A methodical study of the thickness of the microdisk and its effects on the WGMs quality factor is conducted through FDTD simulations. Then, an alternative to the conventional pedestal approach based on nanoporous GaN cladding layer is presented. The fabricated porous GaN devices showed whispering gallery modes with a FSR of 10 nm, under optical pumping conditions. FDTD method gives spectral results that are in good agreement with the experimental measurements. The inherent trade-off between high porosity and high series resistance compromised the results of the electrical injected devices. Thus, WGMs were not observed under CW electrical injection. Finally, a study based on SiLENSE of the number of MQWs in III-nitride devices is carried out, the result showed fewer MQWs lead to a more efficient carrier injection. These results were used as a starting point in section 8.1.4, where a ridge laser was designed.

8.1.2 Enabling emission stability to microLED arrays by using microcavity effects

A novel approach to mitigate one of the consequences of QCSE, the so-called ‘blue shifting’, has been demonstrated. Thus, the design, fabrication and characterisation of a microcavity based III-nitride micro emitter was introduced. Porous DBRs were formed by means of electrochemical etching, showing exceptional reflectivities values (>99%). Selective overgrowth method formed microemitters with 3.6 μm diameter. The combination of a nearly lattice matched porous DBR and the microemitter led to microcavity effects, proven by FDTD simulations. The electrical characterisation showed a 3 nm shifting of the emission peak, while the emission of the non-cavity-based device shifting was 50 nm under the same current conditions. Furthermore, the spectral linewidth was also affected by the cavity effect, being narrowed from 50 nm to 25 nm. Thus, this approach could clearly benefit the fabrication of full colour micro displays.

8.1.3 Towards micro-Vertical Surface Emitting Lasers (VCSELs) based on III-nitride selective overgrowth

An alternative patented approach to the fabrication of III-nitride VCSELs has been demonstrated, which is achieved by developing a direct epitaxial method

based on selective epitaxial growth. Microemitters with 3.6 µm diameter were stacked between a porous-dielectric DBRs. Modes with a FWHM of 4nm were observed by confocal PL. FDTD simulations were carried out to verify the experimental results, a good agreement between the simulated model and the experimental data was obtained. The EC etching conditions were optimised, leading to a noticeable reduction of the series resistance. Although stimulated emission has not been confirmed yet, microcavity effects have been observed under either optical or electrical pumping. The emission linewidth has been narrowed down to 5.5 nm under electrical injection conditions. The results show the high potential of this novel-patented approach.

8.1.4 Enabling high confinement factor edge emitting lasers by using a nanoporous GaN cladding layer

The potential of nanoporous cladding layers in edge emitting lasers was studied, as an alternative of conventional AlGaN. The enhancement of optical confinement factor was demonstrated through FDE simulations, where a proper design showed an improvement by a factor of two. The formation of porous cladding layers was successively achieved by means of EC, where a low refractive index of 1.86 was obtained. Then, electrically injected nanoporous ridge laser devices were fabricated and characterised, stimulated emission was not confirmed. Although facet formation processing was not optimised and compromised the results, this chapter presents a novel approach towards a low threshold green edge emitting laser.

8.2 Future work

8.2.1 RGB microemitters with stable emission

As introduced in chapters 2 and 5, III-nitride based devices suffer a blue shift in the emission wavelength as the injection current is increased. Chapter 5, introduced a approach to partially mitigate this effect based on microcavity effects. Our group has recently presented 2µm diameter red microemitters with a peak EQE of 1.75% [1]. However, a strong blue shifting due to QCSE was observed. Potentially, the emission stability demonstrated here could be used to form colour stable microLEDs at longer wavelengths. In order to achieve it, the DBR thickness should be modified to produce a stopband in the red region spectra. This presents interesting applications such a colour stable RGB microdisplay. Currently, we are developing red DBRs in order to prove this idea.

8.2.2 micro-Vertical Surface Emitting Laser optimisation and porous thermal management.

The present work is a preliminary investigation on the feasibility of a micro-Vertical Surface Emitting Laser based on III-nitride selective overgrowth. As

such, a further optimisation on the selective overgrowth to minimise parasitic resistance can lead to an improved device performance. The selective overgrowth also introduces InGaN products between the microemitters (on top of the SiO_2), which led to a Q-factor reduction. Recently, our group has started to apply a post-growth annealing which partially eliminates the residual InGaN products. Thus, the deposition of the top DBR on a flat surface could reduce the scattering losses, leading to a stimulated emission.

Microcavity effects have been demonstrated on the fabricated devices, but lasing has not been fully confirmed. It is then noteworthy to verify the resulting polarization along with the microcavity effects. The performance of the microemitters is significantly affected by the poor heat dissipation of the substrate and the porous-dielectric DBR. In order to understand the current problem, thermal modelling of the hybrid cavity must be carried out. It is highly suggested to utilise a temperature-controlled stage when probing these particular devices, a new setup is being built at the moment.

8.2.3 Developing nanoporous edge emitting lasers.

Further development is needed in order to process the laser facets. Many authors have expressed the difficulties related with facet formation in sapphire substrates [2]. Laser cutting could be a costly but functional option [3]. Additionally, with an optimised process the facets could be formed by ICP etching or CAIBE (chemically assisted ion beam etching) [4-5]. Recently, our group has grown LD structures on semipolar GaN, which show higher PL intensity than c-plane sapphire and potentially could be easier to cleave (as the cleaving planes are well defined).

Moreover, the growth conditions could also be optimised. Recently, our group found out that the incorporation of H_2 on the barriers lead into an increase of the PL intensity in LD structures. This could potentially impact the gain material of the MQWs.

8.2 References

[1] P. Feng, et al., A simple approach to achieving ultrasmall III-Nitride microlight-emitting diodes with red emission. ACS Applied Electronic Materials, 4:6:2787-2792, 2022.

[2] J.H. Kang, et al., On the formation of cleaved mirror facets of GaN-based laser diodes—A comparative study of diamond-tip edge-scribing and laser scribing. Journal of Vacuum Science & Technology, 34:4, 2016

[3] D.A. Stocker, E.F. Schubert, W. Grieshaber, Facet roughness analysis for InGaN/GaN lasers with cleaved facets. Applied Physics Letters, 73:1925, 1998.

[4] S. Gandrothula, et al., Semipolar {2021} GaN Edge-Emitting Laser Diode on Epitaxial Lateral Overgrown Wing. Crystals, 11:1563, 2021.

[5] J. Rass, et al., Facet formation for laser diodes on nonpolar and semipolar GaN. Physica Status Solidi (a), 207:6:131-1364, 2010